Nano-structuring is a promising way to improve the efficiency of light emitting diodes (LEDs): two-dimensional photonic crystals can help to extract light from LEDs with the option of shaping the emission pattern, but can also increase the internal quantum efficiency in combination with surface plasmon polaritons. Both concepts are investigated theoretically in order to quantify for the first time their benefit in comparison to standard state-of-the-art LEDs. The impact of the photonic crystal design is investigated in depth along with the importance of the LED's layer stack. Additionally, the value of photonic crystal LEDs for the application in étendue-limited systems is discussed.

Universitätsverlag Regensburg

ISBN 978-3-86845-046-0

gefördert von:

Alumni der physikalischen Fakultät der Universität Regensburg e.V.

Universität Regensburg

Dissertationsreihe Physik - Band 11

Christopher Wiesmann

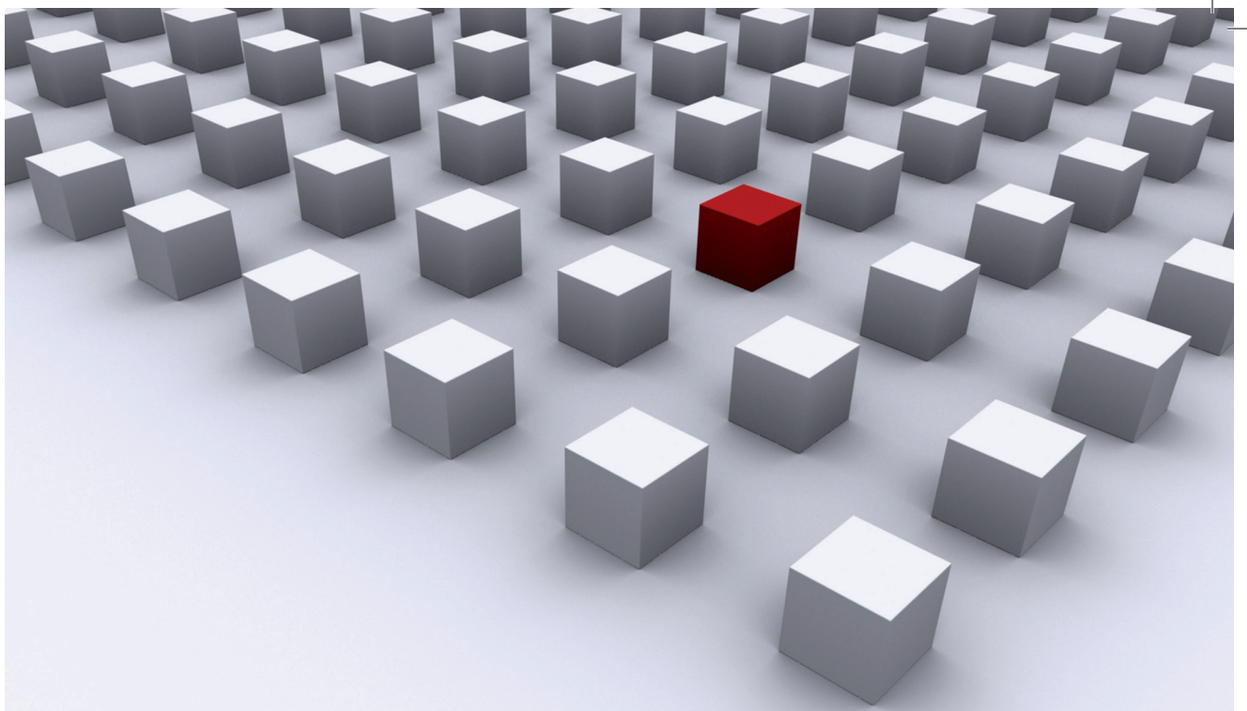

Christopher Wiesmann

Nano-structured LEDs – Light Extraction Mechanisms and Applications

Universitätsverlag Regensburg

11

Dissertationsreihe Physik

Christopher Wiesmann

Christopher Wiesmann

Nano-structured LEDs –
Light Extraction Mechanisms
and Applications

Nano-structured LEDs – Light Extraction Mechanisms and Applications

Dissertation zur Erlangung des Doktorgrades der Naturwissenschaften (Dr. rer. nat.)
der naturwissenschaftlichen Fakultät II - Physik der Universität Regensburg
vorgelegt von

Christopher Wiesmann

aus Ludwigsthal
Januar 2009

Die Arbeit wurde von PD Dr. Ulrich T. Schwarz angeleitet.
Das Promotionsgesuch wurde am 16.01.2009 eingereicht.
Das Kolloquium fand am 13.10.2009 statt.

Prüfungsausschuss:
Vorsitzender: Prof. Dr. V. M. Braun
1. Gutachter: PD Dr. U. T. Schwarz
2. Gutachter: Prof. Dr. J. Zweck
weiterer Prüfer: Prof. Dr. Ch. Strunk

Dissertationsreihe der Fakultät für Physik der Universität Regensburg, Band 11

Herausgegeben vom Präsidium des Alumnivereins der Physikalischen Fakultät:
Klaus Richter, Andreas Schäfer, Werner Wegscheider, Dieter Weiss

Christopher Wiesmann

Nano-structured LEDs – Light Extraction Mechanisms and Applications

Universitätsverlag Regensburg

Bibliografische Informationen der Deutschen Bibliothek.
Die Deutsche Bibliothek verzeichnet diese Publikation
in der Deutschen Nationalbibliografie. Detailierte bibliografische Daten
sind im Internet über http://dnb.ddb.de abrufbar.

1. Auflage 2010

Leibnitzstraße 13, 93055 Regensburg

Konzeption: Thomas Geiger
Umschlagentwurf: Franz Stadler, Designcooperative Nittenau eG
Layout: Christopher Wiesmann
Druck: Docupoint, Magdeburg
ISBN: 978-3-86845-046-0

Weitere Informationen zum Verlagsprogramm erhalten Sie unter:
www.univerlag-regensburg.de

Nano-structured LEDs –
Light Extraction Mechanisms and Applications

DISSERTATION ZUR ERLANGUNG DES DOKTORGRADES DER NATURWISSENSCHAFTEN (DR. RER. NAT.)
DER FAKULTÄT II - PHYSIK

DER UNIVERSITÄT REGENSBURG

vorgelegt von

Christopher Wiesmann

aus
Ludwigsthal

im Jahr 2009

Promotionsgesuch eingereicht am: 16.01.2009
Die Arbeit wurde angeleitet von: PD Dr. Ulrich T. Schwarz

Prüfungsausschuss:	Vorsitzender:	Prof. Dr. V. M. Braun
	1. Gutachter:	PD Dr. U. T. Schwarz
	2. Gutachter:	Prof. Dr. J. Zweck
	weiterer Prüfer:	Prof. Dr. Ch. Strunk

Contents

1 Introduction **3**

2 LED Basics **6**

2.1 White LED Efficiency 7

2.2 Internal Quantum Efficiency 9

2.3 Extraction Efficiency 11

2.3.1 Total Internal Reflection 11

2.3.2 Redistribution of Light 13

2.3.3 RCLEDs 16

2.4 Étendue 18

2.5 InGaN Material System 20

3 Photonic Crystals **22**

3.1 Dispersion Relation: Uncorrugated Slab 24

3.2 Dispersion Relation: Artificial PhC Slab 25

3.3 Dispersion Relation: PhC Slab 27

3.4 Conclusions for PhC LEDs 29

4 Theoretical Methods **31**

4.1 Transfer Matrix with a Dipole Source 31

4.1.1 Source Distributions: Bulk, Quantum Wells, and Wurtzite Structure 32

4.1.2 Transfer Matrix 33

4.2 Diffraction Model 35

4.2.1 Eigensolutions of a Co-Planar Layer Stack 35

4.2.2 Coupled Mode Theory 37

4.3 FDTD Method 41

4.3.1 Simulation Setup 42

4.3.2 Extraction Efficiency 43

4.3.3 Purcell Factor 45

4.3.4 Far Field Radiation Pattern 45

4.3.5 Calculating Dispersion Relations 46

4.3.6 Model for Metallic Mirrors 47

5 Weak PhC LEDs **49**

5.1 Lateral Part: Reciprocal Lattice Vector, Lattice Type and Filling Fraction 51

5.1.1 Reciprocal Lattice Vector 51

5.1.2 Lattice Type: Omni-directionality 54

5.1.3 Filling Fraction 58

5.2 Vertical Part: LED Layer Stack 60
5.2.1 Etch Depth and LED Thickness 60
5.2.2 Multimode Case 67
5.2.3 Spontaneous Emission Distribution 69
5.3 Directionality 72
5.3.1 Geometrical Considerations 72
5.3.2 Radiative Modes and Directionality 75
5.3.3 Multiple Guided Modes 77
5.3.4 Omni-Directionality and Directionality 80
5.4 Experimental Results and Comparison 81
5.4.1 Green InGaN Thin-Film LED 82
5.4.2 Red AlGaInP LED 84
6 Metallic PhCs: Surface Plasmon Polariton LED 86
6.1 Surface Plasmon Polaritons: Basics 86
6.2 FDTD Simulation Setup 88
6.3 Green InGaN SPP LED 89
6.4 Conclusions on SPP LEDs 92
7 Comparison of PhC LEDs and Roughened LEDs 93
7.1 Extraction Efficiency 93
7.1.1 Estimations from the Photonic Strength 93
7.1.2 FDTD: PhC LED vs. Rough LED 95
7.1.3 Optimised PhC LED 96
7.2 Étendue Limited Applications 98
8 Conclusions 101
9 Appendix 103
10 Bibliography 105

1 Introduction

After the first observation of electroluminescence in 1907 [1] and some early work on this topic twenty years later [2] by an almost forgotten Russian scientist, Oleg V. Losev, the LED experienced robust progress in efficiency since 1962 [3] and became a hot favourite in the race of the most efficient light sources. Compared to the traditional light source, the light bulb, with its approximate efficacy of 12lm/W the LED offers a great potential in energy savings according to its nowadays efficacy of ~100lm/W and its expected efficacy of 150lm/W. Even compared to CFLs (compact fluorescence lamps) with 60lm/W, the LED shows superior performance. In [4] the potential savings of green house gas emission by replacing all incandescent lamps and all CFLs by LEDs are estimated. In 2005 all buildings worldwide emitted 8.3Gt of CO_2 and 15% stemmed from lighting. For a comparison, the emission from buildings is roughly 70% higher than that of the whole road transportation sector worldwide, while the lighting used in buildings generated approximately half as much CO_2 as all light-duty vehicles (passenger and commercial vehicles with weight <3.5t) worldwide. Aggressively enforcing the replacement could save more than 400Mt of CO_2 emissions per year in 2030 and additionally save more than 300€ per emitted ton of CO_2 compared to a business-as-usual scenario. Hence, there is a great potential in reducing green house gas emission by using LEDs and pushing their efficacy further. Apart from the savings in green house gas emission the high efficiency leads to a reduced consumption of primary energy sources, like petroleum, natural gas, coal, and nuclear power while keeping our standard of living. Of course, to reach this goal a drastic reduction of the LEDs' costs have to be accomplished.

By now, LEDs are widely used as backlighting for LCD monitors in mobiles and notebooks, in automotive interior and exterior lighting, traffic lighting, video walls, architectural lighting, in pocket projectors and many more. For this huge variety of application fields the commercial applicability of the wide band gap material system InGaN (Indium Gallium Nitride) for generation of UV, blue, and green light was decisive. The main challenge was to achieve sufficient crystalline quality and high p-type doping of GaN layers. After achieving this breakthrough [5] white LEDs are realized in two ways [6] nowadays. The first way is to group the three colours red, green and blue (and sometimes additional colours like amber for better colour rendering) obtained from individual LED chips. The human eye recognizes the superposition as white light. InGaN with varying Indium content is used for blue and green. For red the quaternary system AlInGaP is widely adopted (also for yellow and orange; the AlGaAs system covers the range from red into the near IR). Fig. 1.1 shows external quantum efficiencies for different emission wavelengths and material systems along with the sensitivity of the human eye. In the second approach, which is most widely used today, a blue chip is used in combination with a phosphor that partially down converts the blue to yellow light. Also in this case the superposition is experienced as white light. Due to its key role in the field of LEDs the main focus of the current scientific work is on InGaN based ones.

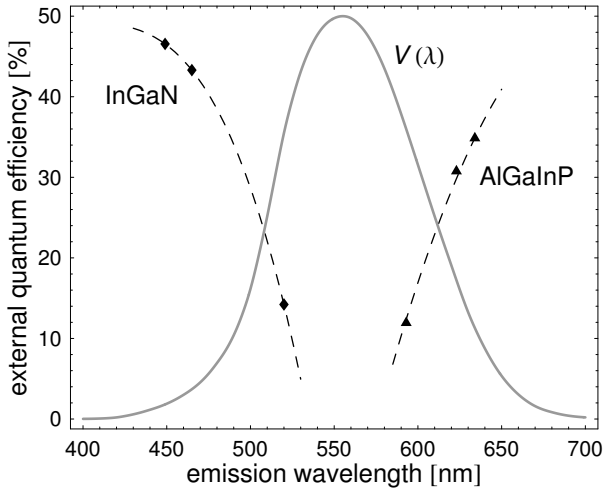

Fig. 1.1: External quantum efficiencies in 2009 for the InGaN and AlGaInP material system as a function of the emission wavelength. Data taken from datasheets of Diamond Dragon LEDs [7]. The grey solid curve indicates the eye sensitivity. Even though most of the visible spectral region is covered by nowadays LEDs, the green colour lacks efficient solid state light sources.

In general, in order to enhance the efficiency of LEDs two quantities have to be improved: the efficiency of light generation and the efficiency of light extraction from the LED chip. In relation to white light generation additional issues like colour temperature and colour rendering have also to be taken into account for the application [6]. The progress in light generation efficiency was dominated by a reduction of defects owing to improved material quality and by the introduction of heterostructures. With the latter a proper band engineering became possible. To enhance the extraction efficiency of LEDs, geometrical solutions have been suggested to overcome total internal reflection, like hemispherically shaped chips [8], the so-called Weierstrass sphere [9] or the truncated-inverted pyramid [10]. In 1993 Schnitzer et. al [11] reported on high efficiencies obtained from LEDs with a mirror at the back and a random surface structuring on the opposite side.

The value of controlled nano-structuring for the efficiency of LEDs was first investigated in [12]. Simulations revealed almost 100% extraction efficiency [13] from a so-called PhC slab with a complete photonic band gap, i.e. a thin semiconductor slab perforated with a periodic, two-dimensional arrangement of holes where the lateral propagation of light is inhibited. However, the practical realization of an electrically driven band gap PhC LED is hardly achievable [14]. Therefore, most PhC LEDs incorporate only shallow etched PhCs at the semiconductor-to-air interface. Here, the PhC diffracts light out of the LED into air [15]-[33]. In this regime, extraction enhancements for the AlGaInP material system as high as 2.6 [15] and in the InGaN system of 2.5 [16] compared to unstructured LEDs have been realized. Moreover, it has been shown that PhCs also have an impact on the radiation characteristics of the LED [17][18]. The latter is of great interest for so-called étendue limited applications, where only the light emitted into a specific solid angle can be used [34][35]. Nano-structured metallic surfaces additionally allow to enhance the efficiency of light generation owing to surface plasmons [36][37].

The present work and the related studies were carried out at Osram Opto Semiconductors GmbH in Regensburg, Germany. Due to its close relation to industry the main focus of this thesis is on diffracting PhCs, as they are most important for the application. The key question to answer is, what are the critical parameters determining the extraction efficiency of PhC LEDs and to derive the limits of this concept if there are any. Moreover, we will compare PhC LEDs with standard, commercial LEDs with respect to the application in order to quantify the benefit from using PhCs. As an example structure we use a green emitting InGaN LED because green LEDs are often the limiting factor for the performance of

RGB systems, like projectors, due to their low efficiency, see Fig. 1.1. Besides, the conclusions can readily be extended to blue due to the similarity of the LED structures.

We start with a summary of basic properties of LEDs that determine the overall efficiency using as an example the world record white LED announced by OSRAM in July, 2008 [38]. The factors that determine the internal quantum efficiency and the extraction efficiency are discussed in more detail. In addition, we summarize the concept of the étendue as it is a crucial quantity for the performance of specific applications in combination with the far field shape of the LED.

Thereafter, the impact of PhCs on the dispersion relation of light is discussed and its benefit for light extraction from LEDs is derived. Furthermore, we point out why band-effects owing to the periodicity of the PhC can be neglected in LEDs with PhCs as a surface structure.

Based upon these conclusions we present a perturbative model that describes the diffraction process of light by the PhC while taking into account the relevant properties of both the PhC and the LED. Besides, we summarize two well established methods that serve as verification tools. The first is a transfer matrix method that takes into account source distributions [39][40] and is capable of determining the extraction efficiency and the emission pattern of co-planar layer stacks without surface structuring. In this context, also the possible source distributions within LEDs are discussed. The other method is the finite-difference time-domain (FDTD) algorithm [41] that provides a general solution of Maxwell's equations for arbitrary three-dimensional geometries.

In the main part of the work we investigate the different parameters of the PhC and the vertical layer stack of the LED in order to derive their impact on the extraction of light. We separate the whole problem into two parts. The first part covers the properties of the PhC, i.e. the pitch, the lattice type and the filling fraction. In the second part we determine the role of the LED's layer stack and the resulting distribution of the generated light for the light extraction mechanism. We use geometrical considerations and the diffraction model to give a clear insight into the physics of PhC LEDs. For every parameter we additionally verify our conclusion with results from the FDTD method. Furthermore, the impact of the PhC on the far field shape is explained. In the end, experimental results are presented and compared to the diffraction model.

Thereafter, surface plasmon mediated light generation in LEDs is studied in detail with the help of the FDTD method in order to, firstly, quantify results from [42] based on a perturbational theory. Secondly, it is possible to give further conclusions on the applicability of surface plasmon polaritons in LEDs and the use of metallic PhCs in general.

In the last chapter, we compare PhC LEDs with standard LEDs in terms of overall efficiency and with respect to étendue limited applications. Here, we quantify the benefit from PhC LEDs.

2 LED Basics

In this section the basic principles determining the efficiency of an LED are summarized. Along with these also the radiometric and photometric quantities are given that are essential for the performance of LED-based applications. Thereafter, we introduce the étendue that determines the efficiency of light sources within applications with a limited acceptance angle. We close this chapter with a summary of aspects special to the InGaN material system.

Fig. 2.1 shows a general setup of a white LED. Here, the primary blue emission from a nitride based LED chip is partially down converted to yellow. A phosphor embedded within a silicone matrix absorbs the blue light and re-emits it in the yellow spectral range. A proper superposition of the directly emitted blue light and the converted yellow light is experienced as white light by the human eye. The semiconductor slab of the LED chip itself consists of an active region sandwiched between an n-doped and a p-doped semiconductor and defines the pn-junction. Nowadays commercial LEDs consist of ternary (InGaN, AlGaAs) or quaternary (AlGaInP) material systems that are grown by metalorganic vapour phase epitaxy (MOVPE) on a growth substrate. The layer thickness depends on the functionality of the specific layer and ranges from a few nm, e.g. the quantum wells of the active region, up to several µm, e.g. the cladding layers. For current injection metallic pads (not shown in Fig. 2.1) are used in direct contact to the n-type and p-type cladding layers, respectively. In order to generate light sufficient voltage V has to be applied, $V > \Delta E/e$, where ΔE is the band gap energy of the quantum well. The injected electrons and holes have the chance to recombine in the vicinity of the pn-junction through a direct transition from the conduction band to the valence band and a photon with wavelength according to the band gap is emitted. In the case of InGaN LEDs the band gap of the quantum wells is determined by their Indium content. The surrounding semiconductor consists of GaN. Since different semiconductors are combined,

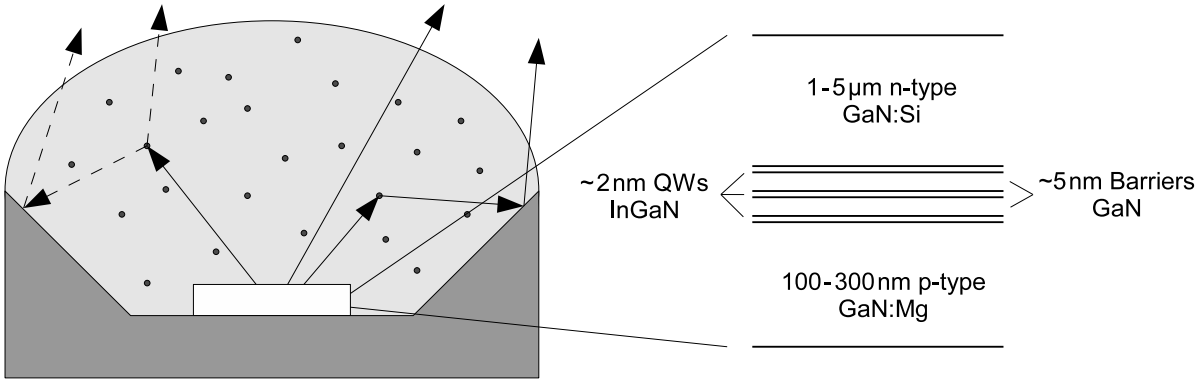

Fig. 2.1: Schematic setup of a white LED with down converting phosphor (dark spots within the silicone matrix in light grey). The reflecting package is shown in dark grey, the InGaN LED chip is white. Solid (dashed) arrows indicate blue (yellow) light. The close-up on the LED chip illustrates the vertical layer stack and gives typical values for the layer thickness.

the epitaxial layer stack is called a heterostructure. By tuning the Indium content the emission wavelength of the quantum wells can be varied; e.g. for blue (green) emission of 450nm (520nm) typical Indium contents of ~17% (~30%) are used [43].

Apart from the LED's pure efficiency that is discussed in the upcoming section, also radiometric quantities and their photometric analogies are crucial for the performance of LED applications. An example discussed in detail in section 7.2 are projection based devices, where only light emitted within some limited external angle can be used. In these applications, besides the total radiant flux also the radiant emittance, the radiant intensity and the radiance have to be taken into account. The radiant flux per source area determines the radiant emittance. The radiant intensity describes the radiant flux per unit solid angle. The emitted power per unit solid angle and seen source area is called radiance. By weighting the radiometric emission with the sensitivity of the human eye, as given in Fig. 1.1, the photometric quantities are derived.

Radiometry	Unit	Photometry	Unit	Description
Radiant flux	[W]	Luminous flux	[lm]	Emitted power
Radiant emittance	$[W/m^2]$	Luminous emittance	$[lm/m^2]=[lx]$	Emitted power per source area
Irradiance	$[W/m^2]$	Illuminance	$[lm/m^2]=[lx]$	Power per area
Radiant intensity	[W/sr]	Luminous intensity	[lm/sr]=[cd]	Power per solid angle
Radiance	$[W/sr/m^2]$	Luminance	$[lm/sr/m^2]=$ $[cd/m^2]$	Power per solid angle and projected source area

Table 2.1: Summary of radiometric and photometric quantities. The latter are calculated by weighting the former with the sensitivity of the human eye. Lumen per area are called Lux [lx], lumen per solid angle give Candela [cd].

2.1 White LED Efficiency

The overall power conversion efficiency or wallplug efficiency η_{Wall} of an LED is given by the ratio of radiant flux with respect to electrical input power and depends on several loss mechanisms

$$\eta_{\mathrm{Wall}} = \frac{\text{emitted flux [W]}}{\text{electrical input power [W]}} = \eta_{\mathrm{el}} \underbrace{\eta_{\mathrm{IQE}}\, \eta_{\mathrm{extr}}}_{\eta_{\mathrm{EQE}}} \eta_{\mathrm{Pack}}\, \eta_{\mathrm{Conv}}\, \eta_{\mathrm{St}}\,, \tag{2.1}$$

with η_{el} the electrical efficiency and η_{EQE} the external quantum efficiency given as the product of the internal quantum efficiency η_{IQE} and the extraction efficiency η_{extr}. The conversion of blue light within the package additionally introduces the package efficiency η_{Pack}, the conversion efficiency η_{Conv} and the Stokes losses η_{St}. The efficiencies and their origin will be discussed in the following. Fig. 2.2 shows the values of the different loss channels for a record 136lm/W white LED [38] consisting of a blue emitting InGaN LED with peak wavelength of 431nm and a yellow-green emitting phosphor consisting of a Yttrium Aluminium garnet doped with Cerium (YAG:Ce). The wallplug efficiency of LEDs is also often given in lm/W in order to take into account the sensitivity of the human eye and is called efficacy.

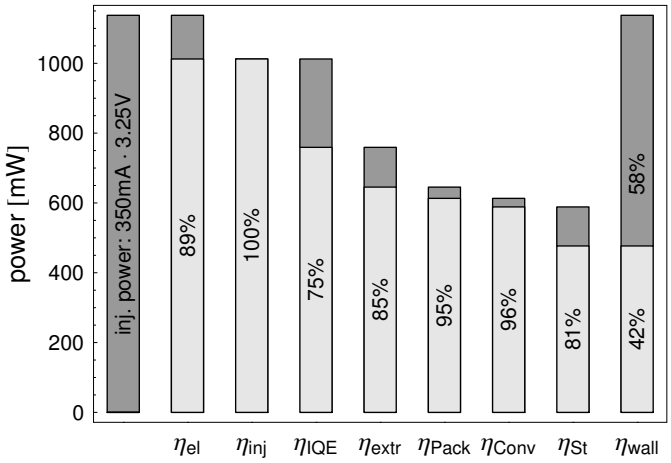

Fig. 2.2: Loss mechanisms for a record 136 lm/W white LED realized with down conversion at 350 mA.

On their way to the active region only a fraction of the charge carriers gets through. Under driving conditions, ohmic losses owing to the resistance of contacts and the epitaxial layers imply an electrical efficiency $\eta_{el}<1$. Here, also the losses associated with the barriers due to piezoelectric fields in the nitride material system are included. According to a peak wavelength of the blue emission of 431 nm≈2.88 eV for the record white LED in Fig. 2.2 the theoretical lower limit of the applied voltage in order to generate photons is at least 2.88 V. From the actually applied 3.25 V at 350 mA the electrical efficiency can be estimated to be 2.88/3.25≈89%.

But even if the charge carriers reach the active region neither every electron generates a photon (internal quantum efficiency, η_{IQE}) due to competitive recombination processes nor every photon can be extracted from the structure (extraction efficiency, η_{extr}) due to absorption. Both efficiencies will be highlighted in the next two sections. For the actual device an extraction efficiency of $\eta_{extr}=85\%$ is obtained from simulations. By measuring the blue LED chip without phosphor but silicone encapsulation the external quantum efficiency can be determined as the ratio between emitted photons to injected electrons, $\eta_{EQE}=64\%$. Consequently, the internal quantum efficiency can be estimated from the ratio between η_{extr} and η_{EQE}, $\eta_{IQE}=75\%$.

After light generation and its escape from the structure, the blue light is partially down converted to yellow light. The associated efficiency is the conversion efficiency η_{Conv} of the phosphor, i.e. the quantum efficiency of the phosphor. Typical phosphors used nowadays for yellow light generation have efficiencies of higher than 90%.

Apart from the losses of photons during the conversion process, energy is also lost due to the mismatch in energy between the blue and the yellow light. This Stokes loss η_{St} cannot be avoided and is given by the ratio between the average photon energies of the phosphor emission and the LED's blue emission. In the above example, $\eta_{St}\approx 81\%$.

As blue light is scattered at the phosphor particles and yellow light is generated isotropically, both propagate in any direction within the silicone matrix. Therefore, part of the light hits the chip and the package and needs to be reflected efficiently. Thus, the absorption of the package has to be as low as possible and mainly contributes to the package efficiency η_{Pack}. Additionally, depending on the geometry and the area fraction of the LED chip within the package, the reflectivity of the LED chip also has to be taken into account. For the package used for the LED of Fig. 2.2 a package efficiency of $\eta_{Pack}\approx 95\%$ has been estimated.

In summary, 42% of the injected electrical power is converted into white light; the remaining 58% contribute to heating of the device. Thus, the heat management of the package is crucial as almost 0.66 W have to be carried away from an area of 1 mm^2. The corresponding

heat flux at this rather moderate driving currents is approximately 10 times higher than that of a conventional hotplate during cooking.

2.2 Internal Quantum Efficiency

Two processes are commonly assumed to determine the internal quantum efficiency η_{IQE} of an LED, the injection of electrons and holes into the quantum wells and their recombination.

The probability of capturing the charge carriers in the quantum wells determines the injection efficiency. Depending on the possible electronic states the electrons or holes possibly can fly directly towards the opposite contact without contributing to light generation. Consequently, the injection efficiency and the overall efficiency of the device is worse than 100%. But even if they occupy states within the quantum well, they can gather thermal energy and leave the quantum well again, what is typically called thermal escape. The corresponding probability necessarily depends on the temperature but also on the potential characteristics defining the well.

Inside the quantum wells of the LED, the desired recombination process of an electron with a hole results in a photon. This radiative recombination process depends on the overlap of the wave functions of electrons and holes and competes with non-radiative recombination processes, that generate phonons rather than photons and thus, lead to heating of the LED chip. In general, the associated efficiency can be written as the ratio of radiative processes over all possible processes and determines the internal quantum efficiency η_{IQE} in combination with the injection efficiency η_{inj}

$$\eta_{\mathrm{IQE}} = \eta_{\mathrm{inj}} \frac{\Lambda_{\mathrm{rad}}}{\Lambda_{\mathrm{rad}} + \Lambda_{\mathrm{nrad}}}, \tag{2.2}$$

with Λ_{rad} the radiative recombination rate and Λ_{nrad} the rate summarizing all non-radiative recombination processes per unit time.

Non-radiative recombination for instance is caused by defects of the semiconductor crystal [44][45], as shown in Fig. 2.3 (left). Electrons jump from the conduction band into energy levels in the band gap offered by these defects. The energy is transferred to phonons instead of photons. During the subsequent recombination of the electron with a hole additional phonons are generated. Thus, this so-called Shockley-Read-Hall (SRH) recombination is non-radiative. As only a finite number of defects exist, the SRH recombination mainly contributes to the internal quantum efficiency at low current densities as long as the defects are not saturated.

Another non-radiative recombination process is the Auger recombination [46], as sketched in Fig. 2.3 (right). Here, an electron recombines with a hole, but the energy is transferred to another electron or hole rather than a photon. The second electron (hole) is pushed into high conduction (low valence) band levels and relaxes back to the band edge while its energy is transferred to phonons. As three charge carriers are necessary for this process, the Auger recombination mainly contributes to the internal quantum efficiency at high current densities in the active region. In the case of InGaN LEDs the decreasing efficiency at high current densities is called efficiency droop – the maximum efficiency is typically achieved at $\sim 10\,\mathrm{A/cm^2}$ whereas common current densities at driving conditions range from 30 to $100\,\mathrm{A/cm^2}$. Even though still under investigation, the Auger recombination seems to be most likely to cause this effect [47][48]. Other explanations for the droop favour a thermal escape from the quantum wells and hence a reduced injection efficiency [49].

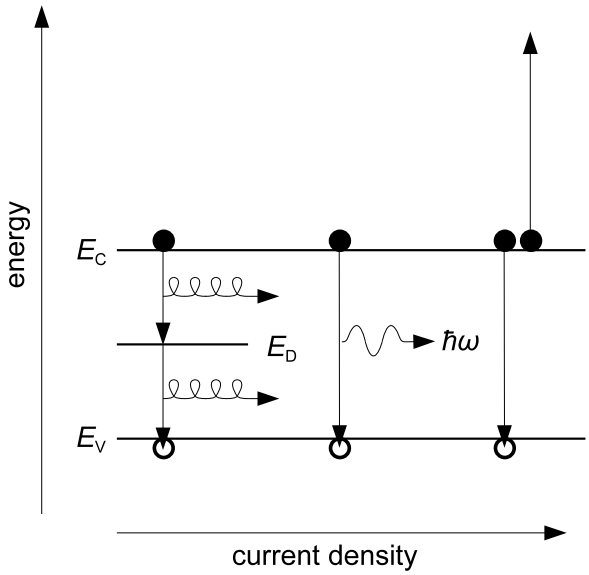

Fig. 2.3: Sketch of different recombination processes in ascending order according to their occurrence with increasing current density. (Left) Shockley-Read-Hall recombination through impurities, (middle) radiative recombination resulting in a photon with energy $E_C - E_V$, (right) Auger recombination. The conduction band is labelled E_C, the valence band E_V and the energy level of a defect E_D.

The radiative recombination involves two charge carriers and hence dominates the recombination process at intermediate current densities compared to SRH and Auger. According to Fermi's Golden Rule the radiative recombination rate is given by

$$\Lambda_{\mathrm{rad}}(\omega,\mathbf{r}) = \frac{2\pi}{\hbar}\left\langle \mathbf{d}\cdot\mathbf{E}(\mathbf{r})\right\rangle^2 \rho(\omega) \tag{2.3}$$

with **d** the electric dipole moment corresponding to the electron-hole transition, **E**(**r**) the local electric field amplitude and $\rho(\omega)$ the density of final photonic states. Thus, not only a proper design of the conduction and the valence band structure which particularly offers a good overlap between electron and hole wavefunction ensures a high radiative recombination rate. Also the optical environment significantly impacts Λ_{rad} through **E**(**r**) and $\rho(\omega)$, what is known as the Purcell effect [50]. The Purcell factor F_P is given by the radiative rate Λ_{rad} stemming from the actual optical environment and the radiative rate $\Lambda_{\mathrm{rad,0}}$ of a dipole in a homogeneous one

$$F_P = \frac{\Lambda_{\mathrm{rad}}}{\Lambda_{\mathrm{rad,0}}}. \tag{2.4}$$

Since the dispersion relation $\omega=\omega(\mathbf{k})$ is a function of the wave vector, the radiative rate, in general, is direction dependent.

In order to investigate the impact of the Purcell factor on the internal quantum efficiency, we assume the injection efficiency to be close to unity and neglect it throughout the further analysis. The intrinsic radiative rate $\Lambda_{\mathrm{rad,0}}$ of an emitter in a homogeneous optical environment is only determined by the electron-hole transition and yields an intrinsic $\eta_{\mathrm{IQE,0}}$ in dependence of the non-radiative recombination rate Λ_{nrad} according to (2.2). With (2.4) the internal quantum efficiency of the actual optical structure reads

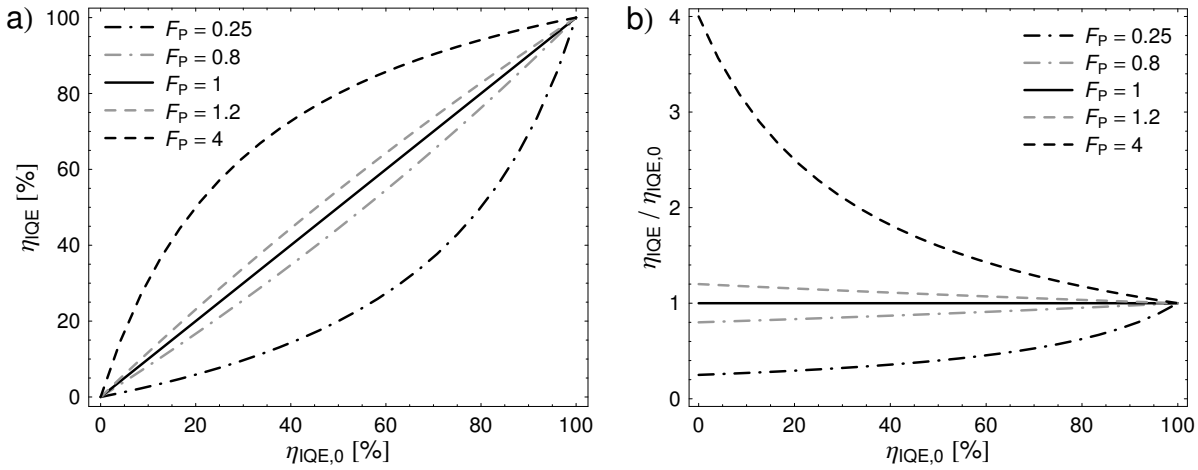

Fig. 2.4: Internal quantum efficiency η_{IQE} in dependence of the intrinsic internal quantum efficiency $\eta_{IQE,0}$ according to (2.5) for $\eta_{inj}=1$ and different Purcell factors: $F_P=1$ (solid black line), $F_P=4$ (dashed black line), $F_P=0.25$ (dash-dotted black line), $F_P=1.2$ (dashed grey line) and $F_P=0.8$ (dash-dotted grey line). Only in the limit of high non-radiative rates and thus low intrinsic internal quantum efficiency the Purcell factor fully contributes to an increase in internal quantum efficiency.

$$\eta_{IQE} = \left(1 + \frac{1-\eta_{IQE,0}}{F_P\ \eta_{IQE,0}}\right)^{-1}. \tag{2.5}$$

Hence, in the case of negligible non-radiative recombination rates and thus, high $\eta_{IQE,0}$, the Purcell factor has hardly any effect on the internal quantum efficiency. The radiative recombination dominates the processes anyway. In contrast, for high non-radiative recombination rates (low $\eta_{IQE,0}$), the Purcell effect fully contributes to the enhancement of the internal quantum efficiency. This can also be seen by taking the limits $\eta_{IQE,0}\rightarrow 0$ and $\eta_{IQE,0}\rightarrow 1$. The former yields $\eta_{IQE}\approx F_P\eta_{IQE,0}$, the latter $\eta_{IQE}\approx 1$. Fig. 2.4 shows the internal quantum efficiency as a function of the intrinsic internal quantum efficiency for different Purcell factors along with the resulting enhancements.

Thus, highly efficient emitters are effected less by a modified optical environment compared to low efficient ones. In co-planar layer stacks typical Purcell factors are of the order of 1. In order to obtain significant enhancement for poor emitters photonic crystals [51][52] or surface plasmon polaritons [36][37] as described in section 6 can be used.

2.3 Extraction Efficiency

In this chapter, first of all the fundamental problem of light extraction from LEDs is sketched. Afterwards, common solutions are explained.

2.3.1 Total Internal Reflection

The extraction efficiency of an LED is mainly limited by the high refractive index contrast between the semiconductor and the ambient medium as illustrated in Fig. 2.5. For GaN based LEDs the refractive index of the semiconductor in the green spectral range is roughly $n_{SC}=2.4$, for the AlGaInP or AlGaAs material systems the refractive index is about $n_{SC}=3.5$ at the corresponding emission wavelengths. From Snell's law of refraction,

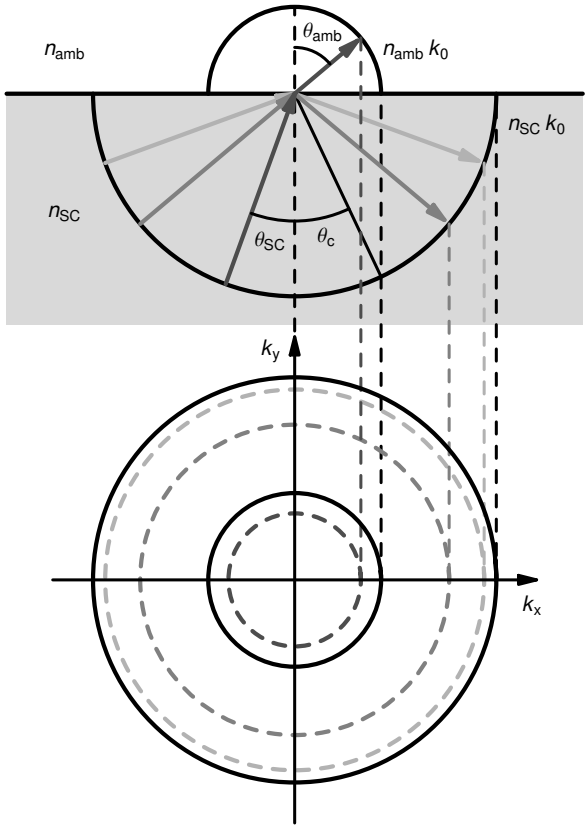

Fig. 2.5: Illustration of Snell's Law of refraction. Light with in-plane k-vector $\beta > n_{amb} k_0$ or equivalently $\theta_{SC} > \theta_c$ cannot escape from the structure. The projection of the k-vectors into the k_x-k_y-plane reveals the ring of guided light with $n_{amb} k_0 < \beta < n_{SC} k_0$ and the extraction disk with $\beta < n_{amb} k_0$.

$$n_{SC} \sin\theta_{SC} = n_{amb} \sin\theta_{amb} , \tag{2.6}$$

the critical angle of total internal reflection is $\theta_c \approx 24.6°$ (16.6°) for the nitrides (phosphides/arsenides) and extraction to air, $n_{amb}=1$. Here, n_{amb} is the refractive index of the ambient medium, θ_{SC} (θ_{amb}) is the angle between the propagation direction within the semiconductor (ambient medium) and the surface normal. Snell's law is equivalent to the conservation of the in-plane k-vector length β. This can be seen by multiplication with the vacuum wave number $k_0=2\pi/\lambda_0$. Thus, only light within the extraction disk, i.e. $\beta < n_{SC} k_0 \sin\theta_c = n_{amb} k_0$, radiates into the ambient medium; light with $\beta > n_{amb} k_0$ is evanescent and thus non-propagative in the ambient medium as the corresponding angle θ_{amb} is purely imaginary. This light never escapes from the flat LED chip and is called guided light. The conservation of the in-plane k-vector is a direct consequence of the translational symmetry parallel to the interface of such a layer stack. The k-vector **k** and the in-plane k-vector **β** are related to each other by $k^2=\beta^2+\gamma^2$ or equivalently $\beta = k\sin\theta$, with γ the k-vector component perpendicular to the semiconductor-to-ambient interface, $\gamma = k\cos\theta$.

With the critical angle in mind, the extraction efficiency for an isotropic source from a high-index material to a low-index material reads

$$\eta_{extr} = \frac{1}{2} \int_0^{\theta_c} T(\theta_{SC}) \sin\theta_{SC} \, d\theta_{SC} \tag{2.7}$$

with $T(\theta_{SC})$ the polarization-averaged Fresnel transmission at the incident angle θ_{SC}. Fig. 2.6

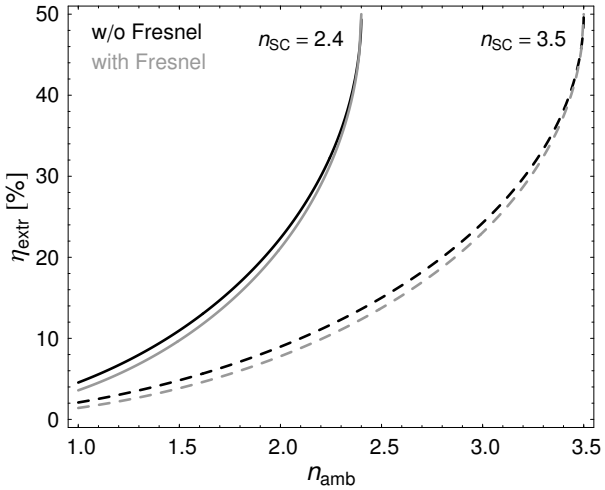

Fig. 2.6: Dependence of the extraction efficiency on the refractive index of the ambient medium with (grey) and without (black) Fresnel reflection at the interface. The solid (dashed) line corresponds to extraction from $n_{SC}=2.4$ ($n_{SC}=3.5$).

shows the efficiency of extracting light according to (2.7) from a nitride-based LED and a phosphide-based LED as a function of n_{amb} with and without Fresnel losses. For $n_{amb}=1$, 4% for the nitrides and 2% for the phosphides of the total generated light can be extracted when Fresnel reflection at the boundary is neglected, i.e. a perfect anti-reflection coating is assumed. This value rises up to 50% in both cases if the refractive index of the ambient medium reaches the refractive index of the semiconductor. However, 100% light extraction is not possible as half of the light is emitted downwards, i.e. away from the semiconductor-to-ambient surface. Nevertheless, an increased refractive index of the ambient medium significantly boosts the extraction efficiency. An early idea for taking advantage of this was to encapsulate the LED within a high index spherical dome [8]. In this case, light hits the encapsulant-to-air interface under normal incidence in any case. In commercial devices, typically silicone with $n=1.4$ is used as an encapsulant as it remains transparent over the LED lifetime and can easily be processed. But still a significant amount of light is totally internally reflected and the extraction efficiency limits the external quantum efficiency to <10%.

2.3.2 Redistribution of Light

Fig. 2.7 shows commonly used solutions to overcome the problem of total internal reflection. In a first approach, five of six facets of the LED chip are used for light extraction, see Fig. 2.7a. In the case of thick, highly transparent window layers the extraction efficiency to air roughly can be enhanced to 20% for InGaN LEDs and 10% for AlGaInP LEDs. However, the efficiency is still limited by the rectangular cross-section of the LED chip. Thus, light totally internally reflected at a semiconductor-to-ambient interface cannot change its incidence angle upon any of the facets and will be absorbed while propagating inside the chip. A geometrically shaped LED chip as shown in Fig. 2.7b changes the angle of guided light and therefore, light totally internally reflected on one facet has the chance to escape from the chip as its incident angle on another facet is different. With this solution high extraction efficiencies of up to 50% for GaN-based LEDs [53] and 55% for AlGaInP based ones [10] have been realized. However, two main drawbacks arise. Firstly, the overall chip size is limited as the light redistribution by the tilted facets enhances the extraction only if the light has the chance to hit the opposite facet before being absorbed. Secondly, the light output is spread over the whole chip surface. This implies a volume-emitting light source with pronounced side-emission. Special packaging is required in order to redirect this light into the forward direction.

Another possibility to circumvent total internal reflection and the formation of guided light is shown in Fig. 2.7c. By incorporating a scattering mechanism into the top surface of the LED light gets redistributed after every incidence on this surface. By additionally incorporating a mirror at the bottom of the LED, the light has several chances to escape from the LED chip after reflectance [11][54]. Furthermore, light gets partially extracted regardless of its incidence angle as it is randomly scattered. The processing of these so-called thin-film LEDs requires bonding the epitaxial layers to a second substrate, like Ge, Si or GaAs, after deposition of the mirror, like Ag, Al or Au. Afterwards, the growth substrate is removed and light is emitted into the ambient through the layer grown first (flip-chip device). In the GaN system laser lift-off is used for removal of the sapphire substrate [55][56]. In the case of AlGaAs or AlGaInP the substrate is removed by wet-etching [57]. With encapsulated thin-flim LEDs high extraction efficiencies of up to 85% for GaN-based LEDs (see section 2.1, [58] and [59]) and 50% external quantum efficiency for AlGaInP based ones [60] have been achieved. Another advantage of thin-film LEDs as compared to volume-emitting LEDs is that the light is extracted only through the top surface. Thus, from the optical point of view no limitations for the lateral dimensions of thin-film LEDs exist as the redistribution takes place at the top surface and these LEDs can be arbitrarily scaled. In practice, the largest chips are 1-2mm² as the production yield and the resulting costs per chip are the main limiting factor. A further positive aspect is that light escapes from a significantly smaller surface area and the radiant emittance increases compared to volume-emitting LEDs. This is of great interest for étendue-limited applications, where as much light as possible is required from a surface as small as possible (see section 2.4 and 7.2). In the case of GaN the rough scattering surface can be obtained from a wet-etching process that reveals pyramids with hexagonal base as shown in Fig. 2.7c [62].

A setup not shown in Fig. 2.7 combines the surface roughening and the idea of tilted facets by incorporating buried micro-reflectors within the LED chip [60][61]. Similar to this, the use of a patterned substrate for GaN LEDs on sapphire breaks the guidance of light within the semiconductor slab due to the refractive index contrast between GaN and sapphire [63].

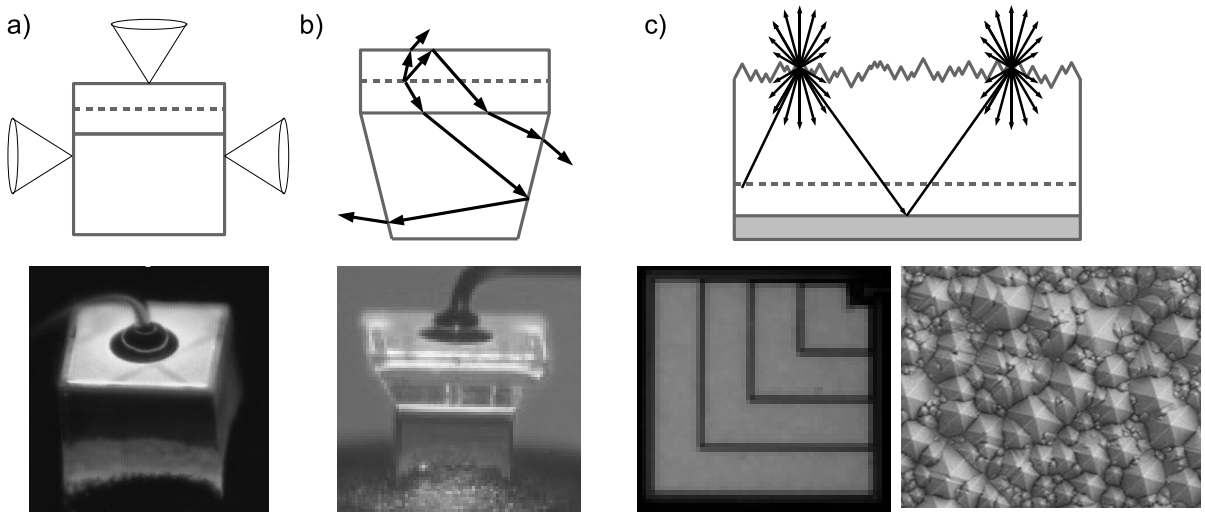

Fig. 2.7: Typical solutions for overcoming the low extraction efficiency of LEDs owing to total internal reflection along with images from devices under operation. (a) Through the use of thick window layers five facets contribute to the extraction of light. The image shows a GaN LED grown on SiC-substrate. (b) Tilted sidewalls redistribute the internally guided light. The image is taken from a GaN LED grown on SiC substrate. (c) Sketch of the thin-film principle: light is extracted partially regardless of its incident angle and redistributed randomly at the rough surface. Due to the bottom mirror the light has several chances to escape from the LED. The image shows an InGaN thin-film LED along with an SEM image of the typical rough surface structure. The contact grid for current injection is visible as black lines.

In any case the redistribution of the internally guided light enhances the extraction efficiency. The overall extraction efficiency is determined by the amount of light extracted per unit length compared to the amount of light absorbed within the same length

$$\eta_{\mathrm{extr}} = \frac{\Gamma}{\Gamma + \alpha} = \frac{1}{1 + \alpha / \Gamma} \tag{2.8}$$

with Γ the extraction and α the absorption coefficient. Therefore, regardless of the type of redistribution process complete light extraction is obtained only in the absence of absorption. Hence, high-performance devices are achieved by decreasing the absorption losses while extracting the light as fast as possible.

To illustrate this relation, Fig. 2.8 shows the extraction efficiency for a LED in thin-film configuration. The absorption coefficient is altered by changing the mirror reflectivity and the value of bulk absorption in the semiconductor with n_{SC}=2.4. By calculating the extraction into air or into silicone the extraction coefficient is also changed. An isotropic light generation is assumed along with a perfect Lambertian redistribution of the light at the random surface texture. The distance between the mirror and the surface is 3µm. It has been further assumed that all light within the critical angle escapes from the structure, i.e. no Fresnel losses. Thus, the extraction efficiency reads

$$\eta_{\mathrm{extr}} = \frac{A_{\mathrm{iso}}}{2}\left(1 + R_{\mathrm{M}}\right)\frac{T_{\mathrm{Lam}}}{1 - A_{\mathrm{Lam}}^2 R_{\mathrm{M}} R_{\mathrm{Lam}}} \tag{2.9}$$

with A_{iso} (A_{Lam}) the amount of light with an isotropic (Lambertian) angle distribution that is not absorbed during a single pass through the semiconductor. R_{Lam} (T_{Lam}) is the power of light with a Lambertian angle distribution reflected (transmitted) at the semiconductor-to-ambient surface. R_{M} accounts for the mirror reflectivity. A detailed derivation of (2.9) is given in the appendix.

The extraction efficiency depends strongly on the mirror reflectivity and increases significantly for highly reflective mirrors. However, both high extraction coefficient and high absorption coefficient decrease this dependency as the light bounces less times between the

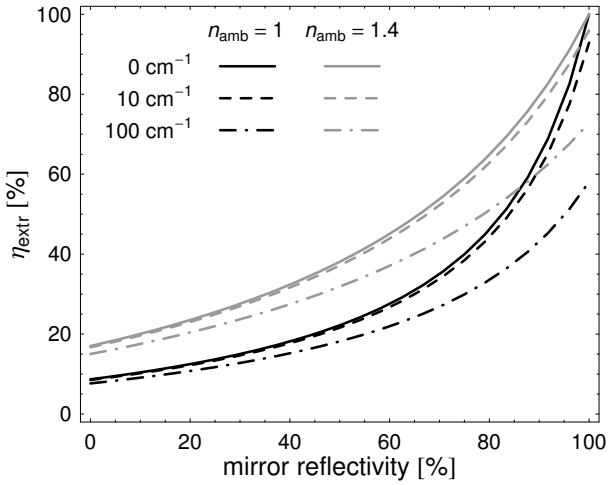

Fig. 2.8: Extraction efficiency as a function of the mirror reflectivity for a GaN-based thin-film LED with the assumption of an isotropic light generation and perfect Lambertian redistribution for extraction to air (black lines) and silicone (grey lines). The solid lines correspond to zero absorption in the semiconductor, the dashed lines correspond to an absorption coefficient of 10 cm^{-1} and the dash-dotted lines are calculated for 100 cm^{-1} absorption. The distance between the mirror and the scattering surface is 3 µm.

mirror and the top surface. Hence, absorption at the mirror has less impact on the extraction efficiency. For extraction to silicone roughly two times more light per round-trip can be extracted compared to extraction to air as can be seen by the extraction efficiencies for vanishing mirror reflectivity. The reason is the ratio between the extracted in-plane k-vector section and that of all in-plane k-vectors, compare Fig. 2.5. In the case of extraction from GaN to air and a Lambertian distribution of light, only $1/2.4^2 \approx 0.17$ of the internally propagating light can escape when incident on the semiconductor-to-air interface, whereas this fraction is $1.4^2/2.4^2 \approx 0.34$ for silicone.

2.3.3 RCLEDs

In contrast to the techniques presented so far that rely on light redistribution in order to enhance the extraction effciency, in so-called resonant cavity LEDs (RCLEDs) light generation within the extraction cone is enforced based on interference effects [64][65][66]. This is realized by embedding the active region into a semiconductor slab sandwiched between two mirrors. The latter form a micro-cavity, i.e. the distance of the two mirrors is on the order a few wavelengths. These mirrors can be metallic, distributed Bragg reflectors (DBRs) or the bare semiconductor-to-air interface. According to this Fabry-Perot setup resonances of the optical field occur depending on the position of light generation, its wavelength and emission angle.

For illustration, in Fig. 2.9a a basic example of an emitter placed in front of a metallic mirror is sketched. Depending on the distance between the active region and the mirror constructive and destructive interference occurs at different angles. Fig. 2.9b shows the radiant intensity as a function of the angle for two distances of an isotropic emitter with wavelength of 520nm in front of a mirror. The values are obtained from the method described in section 4.1. In the case of a distance between the source and the mirror of d=110nm, constructive interference takes place for angles below the critical angle. Hence, higher radiant intensities are obtained compared to a distance of d=160nm. Consequently, according to Fermi's Golden Rule (2.3) more light is generated within the extraction cone for d=110nm compared to d=160nm due to a higher electric field amplitude for emission angles below the critical angle. In sum, the extraction efficiency is as high as 13.4% for 110nm, whereas it is only 4.4% for 160nm.

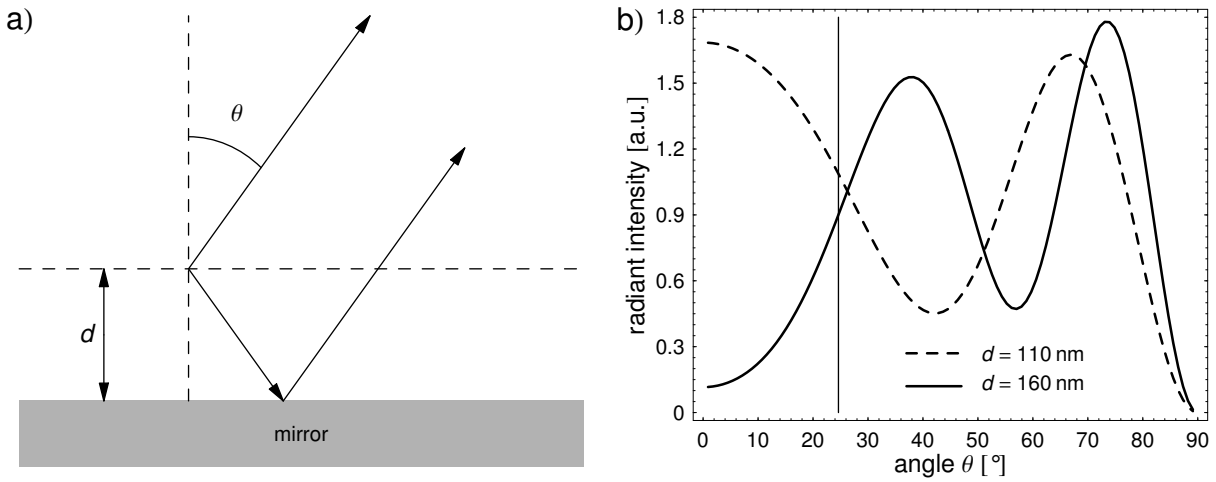

Fig. 2.9: (a) Interference of generated and reflected light. The horizontal dashed line indicates the position of the active region within the semiconductor. The mirror is shown in grey. The arrows indicate the propagation direction of the two interfering plane waves. (b) Radiant intensity for an isotropic emitter placed d=160nm (solid line) and d=110nm (dashed line) above a mirror. The semiconductor refractive index is 2.4 and the wavelength 520nm. The vertical line indicates the critical angle θ_c. The calculations are done with the algorithm presented in section 4.1.

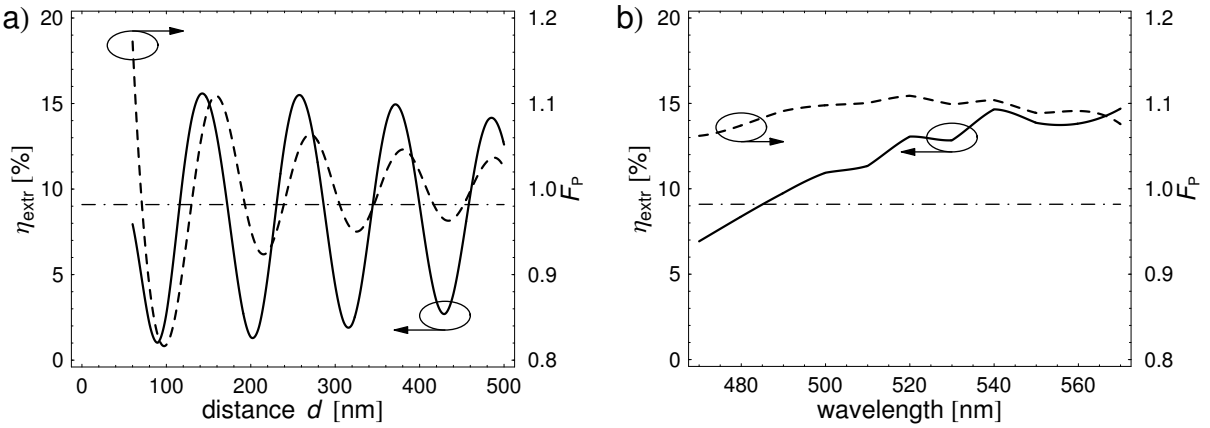

Fig. 2.10: (a) Extraction efficiency to air (solid line and left y-axis) and Purcell factor F_P (dashed line and right y-axis) as a function of the distance d between the isotropic source with emission wavelength of 520nm and the silver mirror. The semiconductor slab is 3µm thick and its refractive index is $n_{SC}=2.4$. (b) Analogous to (a) for a distance $d=160$nm and varying wavelength. The oscillations of both quantities stem from the interference between the source and its mirror image. The horizontal dash-dotted line indicates the extraction efficiency according to (2.7) without Fresnel losses and doubled owing to the mirror.

In order to obtain an even stronger interaction of the source with the surrounding cavity, the second mirror can be used. In this case, extraction efficiencies of up to 22% in the InGaN material system [67], 23% from encapsulated AlGaInP chips [68] and 30% with AlGaAs have been realized [69]. Consequently, also the far field pattern can be changed by tuning the cavity properly [68] but on the expense of overall extraction efficiency. However, in any case these values cannot compete with extraction efficiencies obtained from the redistribution techniques of the former section.

In general, the micro-cavity effect as shown in Fig. 2.9 is present in any LED if the distance between the source and one of the mirrors is small. In this case, the internal light generation can be optimised for best interaction with respect to an extraction scheme, e.g. surface structuring. This will be discussed in detail in section 5.2.3 with PhCs as a surface texture. Additionally, apart from the extraction efficiency also the overall radiative rate or the Purcell factor can be altered as shown in Fig. 2.10a [70]. The corresponding structure emitting isotropically at 520nm consists of a 3µm thick LED with refractive index $n_{SC}=2.4$ and a silver bottom mirror. The semiconductor-to-air interface is left un-structured.

The oscillations of the Purcell factor arise from two facts. Firstly, the interference between the source and its mirror image occurs at different angles as the distance between the source and the mirror changes, see Fig. 2.9. Secondly, large angles (e.g. $70°<\theta_{SC}<90°$) offer more photonic states in k-space compared to smaller ones as the latter cover a smaller area in k-space, see Fig. 2.5. Thus, if the interferences coincide with large angles, the Purcell factor increases according to the larger number of photonic states. In contrast, if light is dominantly emitted into small angles, the Purcell factor decreases.

However, apart from the angle of incidence and the distance between the source and the mirror the wavelength itself impacts these interferences. Thus, in order to benefit from an optimised design, the emission spectrum has to be kept constant. For instance, heating of the LED chip typically causes a shift of the emission to longer wavelength as the band gap decreases [71]. The resulting de-tuning between the surrounding optical environment and the emission worsens the extraction efficiency, see Fig. 2.10b. In the nitride material system, the blue shift of the emission due to screening of the internal piezo-electric fields with increasing current density has similar impact.

2.4 Étendue

In contrast to the efficiencies discussed so far the étendue is not a property specific to LEDs but comes into consideration if the emission of a light source has to be coupled into an optical system. Examples for such applications are projectors [34][35], automotive headlamps [35] or simply coupling the light into an optical fibre.

In general, the étendue E defines the phase space volume of light that can pass an optical element and is given by[1]

$$E = \pi n^2 A \sin^2 \theta \tag{2.10}$$

with n the ambient refractive index. The area A (the angle θ with respect to the optical axis) defines the area (angle), where light can pass through the optical element.

Consider for instance the simplified system as sketched in Fig. 2.11. Light is generated within an area A_L, passes some optics (in this case a lens) and hits the target area A_T. In the case of projectors, the target is the imager, e.g. a DMD (digital mirror device), LCoS (liquid crystal on silicon) or LCD (liquid crystal display). We will investigate the DMD example in the following. Here, micro mirrors, that are mechanically adjustable, are used to generate the image [72], where every mirror represents a single pixel on the screen. The tilt angle of the mirror relative to the optical axis determines the on and off state of the pixel. Typically, the full angle between on and off state is 24°. Hence, for proper operating of the DMD only light within ±12° relative to the optical axis should hit the imager. These 12° determine the target angle θ_T in our example. The target area is simply given by the total area of all micro mirrors and is A_T=93.7 mm^2 for a 0.55" DMD. According to (2.10) the phase space of light that can pass the DMD and is projected onto the screen is E_T=12.7 mm^{2}sr with n=1. In the case of a non-scattering, loss-free optical systems, the optical element with the smallest étendue defines the overall throughput of the system. Only light within this phase space can pass the whole system. If we assume that the optics can be chosen without limitations regarding their size or functionality, the limiting element in projectors is the imager.

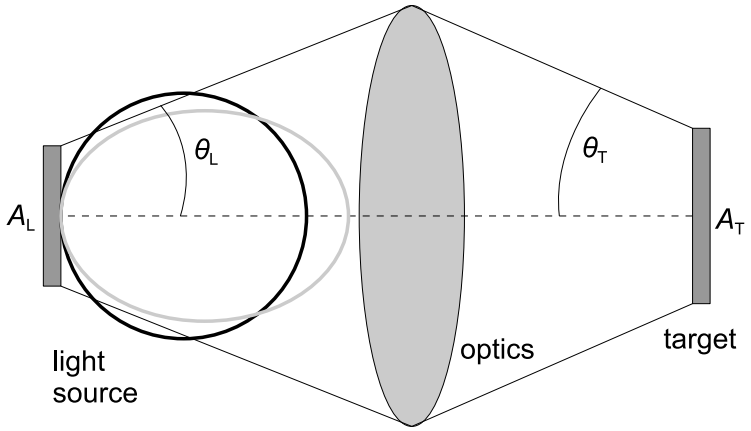

Fig. 2.11: Sketch of an étendue limited system. Light generated within the area A_L is projected by the lens (grey oval) onto the target area A_T. According to étendue matching the acceptance angle of the target θ_T determines the acceptance angle θ_L of the system for the light source at given areas A_L and A_T. A larger fraction of the emission is projected onto the target area in the case of a light source with pronounced forward emission (grey line) compared to standard (Lambertian) emission characteristic.

[1] The definition of the étendue in (2.9) is valid for rotational symmetries. In general, the étendue is defined by its differential form, $dE=n^2\cos\theta d\Omega dA$, with n the refractive index, θ the polar angle with respect to the optical axis, $d\Omega$ the solid angle and the surface area dA.

From this limitation the following consequences arise for the design of the light source. If the source emits light beyond the phase space of the imager, i.e. $E_L > E_T$, light will be wasted as it cannot be projected onto the imager. On the other hand, if the phase space of light emission is too small, i.e. $E_L < E_T$, we do not exploit the possible phase space. Consequently, less light will be projected onto the imager compared to a case, where the étendue of both systems match. Therefore, if the complete emission of the light source is collected, $\theta_L = 90°$ with an optics as described in [35], the maximum applicable source area for the 0.55" imager is 4mm^2 ($E_L = E_T$). Larger source areas will not project more light onto the imager. The only way to accomplish this is to enhance the radiant emittance from the source, i.e. increasing the light output from the same area. One might think, that encapsulating the LED chip enhances the amount of light coupled into the target's étendue as it results in higher extraction efficiencies and thus in an increased radiant emittance. However, according to the spherical encapsulation the ambient medium of the LED is not air but the encapsulant. Hence, the étendue of the light source is increased by the squared refractive index of the encapsulant corresponding to (2.10). Therefore, light is emitted into a larger phase space compared to extraction into air and the enhancement in extraction efficiency does not necessarily overcome this penalty in étendue.

The condition of étendue matching $E_L = E_T$ in general also holds for systems with a limited acceptance angle $\theta_L < 90°$. In this case, the source area has to be increased according to

$$A_L = \frac{E_T}{\pi \sin^2 \theta_L} \tag{2.11}$$

in order to occupy the phase space provided by the imager. Fig. 2.12 gives the required source area as a function of the acceptance angle θ_L per target étendue E_T. In the case of LEDs, this source area is achieved by grouping several chips. Large chips are favourable in order to reduce the area between the individual chips[2]. However, large source areas increase the costs of the system as more chips have to be used. The optics get more bulky and more expensive, too. Hence, in terms of costs the reduction of the target étendue is preferable as fewer chips have to be used and the imager gets cheaper. This is only possible at the expense of flux on the screen if the useful radiant flux cannot be enhanced.

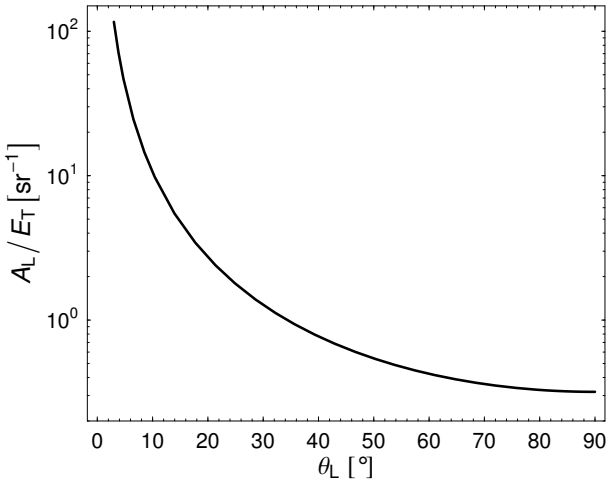

Fig. 2.12: Required source area A_L per target étendue E_T as a function of the acceptance angle θ_L under the condition of étendue matching $E_L = E_T$.

[2] Reducing the spacing between the chips also improves the homogeneity of the radiant emittance over the whole source area.

In order to achieve the optimum flux on the target the phase space volume should be "filled" with as much light as possible, i.e. the emitted flux from the source within that étendue should be as high as possible. As sketched in Fig. 2.11 a more collimated far field is preferable for $\theta_L<90°$ as a larger fraction of the total flux is emitted into the target's étendue and projected onto the imager. However, apart from the far field shape also the radiant flux contributes to the radiance and thus, the amount of flux on the imager. A quantitative discussion regarding these issues is given in section 7.2 for the comparison between PhC LEDs and roughened thin-film LEDs. The prior have the possibility to shape the emission pattern, while the latter are the benchmark due to their high extraction efficiency.

In general, the local radiance, i.e. the local radiant emittance in combination with the local radiant intensity, has to be considered over the whole chip area [73] in order to determine the total radiant flux emitted into the target's étendue. For instance, in the vicinity of the electrical contacts more light is generated compared to areas far away from the contacts. Hence, a different amount of flux is emitted in both cases. Also the emission profile may differ from location to location, e.g. due to shadowing by the contacts. Thus, both the radiant emittance and the radiant intensity are not uniform across the LED chip. However, for the sake of simplicity we will neglect these issues during this work and consider the radiance as homogenous over the complete chip area.

2.5 InGaN Material System

Some peculiarities of the InGaN material system compared to the traditional material systems, like AlGaInP or AlGaAs, have to be mentioned that define the parameter space for the "photonic" optimisation.

As briefly addressed above, the growth of GaN is already challenging. The main reason for this is that the best suited growth substrate, GaN itself, is far too expensive by now. Therefore, alternative substrates have to be used. The most popular is sapphire (Al_2O_3) as it is cheap and reasonable results are achieved. However, the lattice mismatch between sapphire and the GaN layers grown on it causes a rather high density of dislocations within the GaN layers. In order to achieve sufficient quality and to reduce the number of defects several µm thick buffer layers are grown before the crucial part, the active region, is deposited, see Fig. 2.13. This results in a typical LED thickness of several µm. The only way to thin these layers while maintaining high crystalline quality is to etch these layers after epitaxy down to the desired thickness. However, this is not favourable in terms of processing costs and processing time.

Also the growth of the active layer is subject to restrictions. The colour range of InGaN LEDs is accomplished by different Indium contents within the active region. The more Indium the smaller the band gap and consequently the longer the emission wavelength. However, due to its large atomic radius Indium tends to nucleate in clusters. Thus, no homogeneous Indium concentration in lateral direction is achieved and the growth of the following layers suffers from poor quality of the active layer especially in the case of high Indium content (typically green and above). Furthermore, owing to the Wurtzite structure of the GaN crystal piezoelectric fields occur at hetero interfaces, e.g. between GaN and InGaN. These piezoelectric fields firstly implicate a separation of the electron and the hole wave function. Hence, recombination rates, both radiative and non-radiative, that rely on the overlap of these two wave functions are decreased [74]. Secondly, the screening of these fields by an applied voltage increases the band gap between conduction and valence band. Therefore, the emission wavelength of GaN based devices shifts to shorter wavelength with increasing current [75].

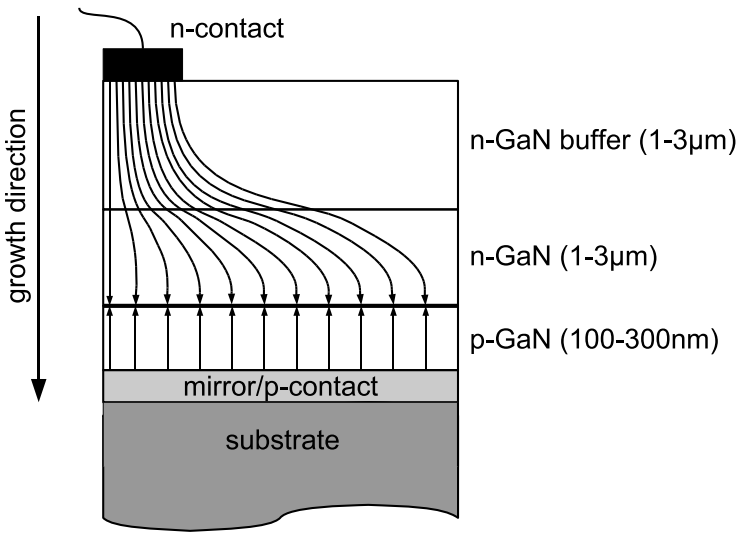

Fig. 2.13: Sketch of an InGaN LED in thin-film configuration. The left arrow indicates the growth direction. The LED is already bonded onto a second substrate after mirror deposition and the initial growth substrate, sapphire, has been removed. The arrows inside the LED indicate the flow of charge carriers from the n-contact and the p-contact towards the pn-junction.

Typically, the growth of InGaN LEDs is closed with the nucleation of the p-type GaN layers. Here, the p-type doping with Mg has to be paid attention to. In the first instance, the doping indeed enables the GaN based LED but the current spreading is fairly poor. Hence, the injected carrier tend to flow vertically through the layer stack rather than spreading laterally. In order to achieve homogeneous carrier injection into the active region the current spreading on the p-side is done by a metallic contact, i.e. the mirror in the case of thin-film LEDs. In addition, with increasing thickness of the p-GaN layer the activation of the dopand becomes less efficient. Therefore, the thickness of the p-GaN layer is typically only 100-300nm in order to limit additional ohmic losses and thus, achieve sufficient electrical efficiency.

3 Photonic Crystals

In analogy to solid-state physics, the aim of photonic crystals is to control the propagation behaviour of light. The propagation of electrons within a crystal depends on the periodic arrangement of the crystal's atoms. In electromagnetism the periodic arrangement of materials with different refractive index has the same impact on the possible photonic states as the periodic potential within a crystal on the electronic states. The periodicity in both cases has to be of the order of the corresponding wavelength, i.e. the de Broglie wavelength in the case of electrons and the optical wavelength in the case of photons. Thus, a one-, two- or three-dimensional periodic arrangement of materials with different refractive indices is called a photonic crystal (PhCs).

The counterpart to Schrödinger's equation describing the electrons in quantum mechanics are Maxwell's equations in electromagnetism. In general, Maxwell's equations read

$$\begin{aligned} \nabla \cdot \mathbf{D} &= \rho \\ \nabla \cdot \mathbf{B} &= 0 \\ \nabla \times \mathbf{E} &= -\frac{\partial \mathbf{B}}{\partial t} \\ \nabla \times \mathbf{H} &= \frac{\partial \mathbf{D}}{\partial t} + \mathbf{J} \end{aligned} \tag{3.1}$$

with $\mathbf{D}=\varepsilon_0\mathbf{E}+\mathbf{P}$ the electric displacement field, ε_0 the electric constant, $\mathbf{E}$ the electric field, $\mathbf{P}$ the polarisation, $\mathbf{B}=\mu_0(\mathbf{H}+\mathbf{M})$ the magnetic induction, μ_0 the magnetic constant, $\mathbf{H}$ the magnetic field, $\mathbf{M}$ the magnetisation density, ρ the charge density, and $\mathbf{J}$ the current density. In the case of isotropic, non-magnetic, linear materials without macroscopic charges (3.1) becomes

$$\begin{aligned} \nabla \cdot \left[\varepsilon(\mathbf{r})\,\mathbf{E}(\mathbf{r})\right] &= 0 \\ \nabla \cdot \mathbf{H}(\mathbf{r}) &= 0 \\ \nabla \times \mathbf{E}(\mathbf{r}) - i\omega\mu_0\,\mathbf{H}(\mathbf{r}) &= 0 \\ \nabla \times \mathbf{H}(\mathbf{r}) + i\omega\varepsilon_0\,\varepsilon(\mathbf{r})\,\mathbf{E}(\mathbf{r}) &= 0 \end{aligned} \tag{3.2}$$

where a harmonic time dependence $\mathbf{H}(\mathbf{r})\sim\mathbf{E}(\mathbf{r})\sim\exp(-i\omega t)$ with ω the frequency of light and a relative permeability of $\mu=1$ has been assumed. Furthermore, the electric displacement field and the magnetic induction are given by $\mathbf{D}=\varepsilon_0\varepsilon(\mathbf{r})\mathbf{E}$ and $\mathbf{B}=\mu_0\mathbf{H}$, respectively. The refractive index $n(\mathbf{r})$ is related to the relative permittivity $\varepsilon(\mathbf{r})$ by $n^2=\varepsilon$ and the vacuum speed of light is given by $c^2=1/\varepsilon_0\mu_0$.

In order to determine the allowed photonic states for a refractive index distribution, the so-called master equation [76] is utilized. It is obtained by dividing the last equation of (3.2) by $\varepsilon(\mathbf{r})$, taking the curl afterwards and using the third equation

$$\nabla\times\left[\frac{1}{\varepsilon(\mathbf{r})}\nabla\times\mathbf{H}(\mathbf{r})\right]=\left(\frac{\omega}{c}\right)^2\mathbf{H}(\mathbf{r})\,. \tag{3.3}$$

The eigenvalue of this equation is the square of frequency. In quantum mechanics the eigenvalue is the energy. From the solution of (3.3) the electric field amplitude is derived with the help of the third equation of (3.2). Alternatively, the corresponding equation to (3.3) for the electric field reads

$$\nabla\times\left[\nabla\times\mathbf{E}(\mathbf{r})\right]=\left(\frac{\omega}{c}\right)^2\varepsilon(\mathbf{r})\,\mathbf{E}(\mathbf{r})\,. \tag{3.4}$$

In the case of a periodic refractive index $n(\mathbf{r})=n(\mathbf{r}+\mathbf{R})$ with $\mathbf{R}=m_1\mathbf{a}_1+m_2\mathbf{a}_2+m_3\mathbf{a}_3$ and $\mathbf{a}_j$ the primitive lattice vectors (m_j an integer), the electric and magnetic field can be written as

$$\begin{aligned}\mathbf{H}_\mathbf{k}(\mathbf{r})&=e^{i\mathbf{kr}}\,\mathbf{u}_\mathbf{k}(\mathbf{r})\,;\;\mathbf{u}_\mathbf{k}(\mathbf{r})=\mathbf{u}_\mathbf{k}(\mathbf{r}+\mathbf{R})\\ \mathbf{E}_\mathbf{k}(\mathbf{r})&=e^{i\mathbf{kr}}\,\mathbf{v}_\mathbf{k}(\mathbf{r})\,;\;\mathbf{v}_\mathbf{k}(\mathbf{r})=\mathbf{v}_\mathbf{k}(\mathbf{r}+\mathbf{R})\end{aligned} \tag{3.5}$$

which is known as Bloch's Theorem. Owing to this periodicity the master equation has to be solved only within the finite sized reciprocal unit cell. This solution determines the dispersion relation of light and consists of several continuous bands $\omega_n=\omega_n(\mathbf{k})$, with n the band index. These bands relate the allowed frequencies to the corresponding k-vectors. Hence, they enable light propagation through the photonic crystal despite the strong scattering of photons at the periodic refractive index structures. However, also the contrary can occur, no light can propagate at a given frequency in any direction. This is called a complete photonic band gap.

Solving (3.3) is challenging in the case of PhC LEDs consisting of a vertical layer stack with a lateral distribution of holes as shown in Fig. 3.1a and offers only little insight into the underlying mechanisms. Thus, in order to understand the propagation behaviour of photons in such a structure, we first of all treat a simplified uncorrugated slab. Afterwards an artificial periodicity is introduced and the formation of the dispersion relation is described. Finally, a corrugated slab is investigated and the role of the PhC in typical PhC LEDs is highlighted. Here, two regimes of PhC LEDs, a weakly coupled PhC LED and a strongly coupled one, can be distinguished.

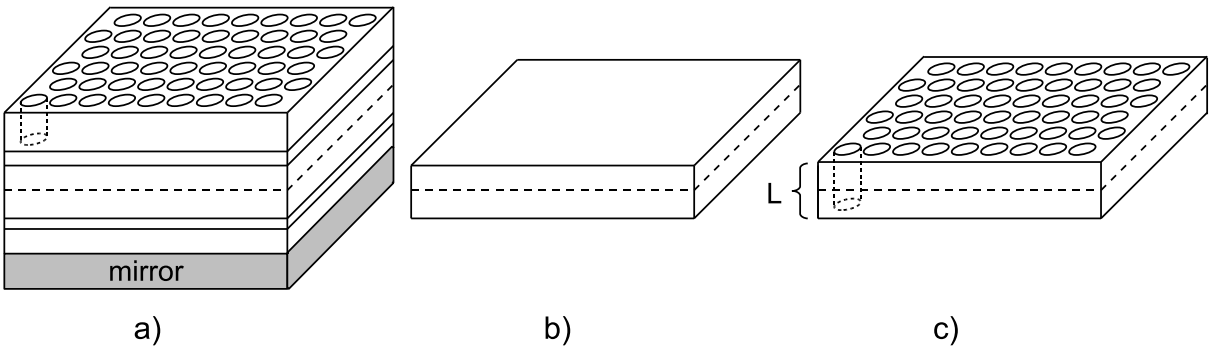

Fig. 3.1: (a) Typical setup of a PhC LED in thin-film configuration. Layers with different refractive indices are sketched along with the active region (dashed line). (b) Uncorrugated slab for the discussion in section 3.1. (c) PhC slab as discussed in section 3.2 and 3.3. The slab thickness is labelled L.

3.1 Dispersion Relation: Uncorrugated Slab

In general, the dispersion relation $\omega=\omega(\mathbf{k})$ relates the propagation direction of light to the allowed frequencies. In the cases treated throughout this work it is convenient to describe the dispersion relation as a function of the in-plane k-vector $\boldsymbol{\beta}$ as the invariant of a system with translational invariance.

For a simple slab as sketched in Fig. 3.1b with two refractive indices, $n_{amb}=1$ and n_{SC}, three regimes can be distinguished, as depicted in Fig. 3.2. The boundaries between them are given by the so-called light line, $\omega=\beta c$, and the semiconductor light line, $\omega=\beta c/n_{SC}$. The first regime corresponds to photonic states that propagate in air and in the semiconductor, $\beta<\omega/c=k_0$. All of these states lie within the extraction disk and the light line is equivalent to the critical angle. The second regime summarizes guided light, that can propagate within the semiconductor but is evanescent in air, $k_0<\beta<n_{SC}\omega/c=n_{SC}k_0$. The third is typically neglected as it describes photonic states that are evanescent even within the semiconductor and hence, carry no energy. This is valid as long as there is no material present with $n>n_{SC}$ or no surface states like surface plasmons exist, see section 6.

For a semiconductor slab with finite thickness only a finite number of confined states exists, so-called guided modes. This is equivalent to the allowed electronic states within a quantum well with finite depth. However, in electromagnetism two polarization states can be distinguished, the TE-polarisation (transverse electric) and the TM-polarisation (transverse magnetic). In the case of TE-polarized (TM-polarized) light, the electric (magnetic) field amplitude is perpendicular to the plane of incidence. The incoming k-vector and the normal to the layer interfaces determine the plane of incidence. A general solution to obtain the guided modes of a layer stack is given in [77] and is also briefly discussed in section 4.2.1. For the case of a symmetric slab as in Fig. 3.1b the solution can also be found in [78]. In Fig. 3.2 the dispersion for the two fundamental guided TE-polarized guided modes is shown.

As Maxwell's equations are invariant under scaling, it is convenient to use the reduced frequency $u=\omega a/2\pi c=a/\lambda$. As a consequence of the scaling invariance, two systems with the same ratio a/λ behave exactly the same. Of course, not only the length a has to be scaled but also all other lengths of the system, e.g. the slab's thickness L.

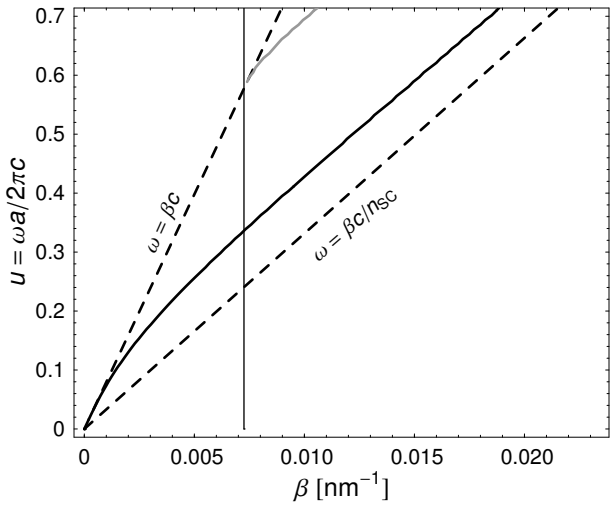

Fig. 3.2: Dispersion relation of the two fundamental TE-polarized guided modes (black and grey line) for a slab as shown in Fig. 3.1b with $n_{amb}=1$ and $n_{SC}=2.4$. The parameter a is the pitch of the lattices used in the upcoming two sections and is chosen $a=2.5L$ with L the slab thickness. The vertical line indicates the position of the first Brillouin zone edge in ΓM direction for the lattice defined in the upcoming section. The dashed lines indicate the light line and the semiconductor light line, respectively.

3.2 Dispersion Relation: Artificial PhC Slab

Before investigating the dispersion relation of a PhC slab as shown in Fig. 3.1c, we have a look at the impact of the periodicity itself on the dispersion of the guided modes. For this reason, the refractive index contrast that defines the lattice is assumed to be infinitely small.

In contrast to the laterally homogeneous slab of section 3.1, now the in-plane propagation directions have to be distinguished. In the case of a hexagonal lattice – that will be examined in the majority of cases in this work – a six-fold symmetry of the Brillouin zone is observed as shown in Fig. 3.3. Additionally, each of these segments is mirror inverted with respect to the ΓK direction. This defines the irreducible Brillouin zone. The reciprocal lattice of a hexagonal lattice with pitch a is set up by the primitive reciprocal lattice vectors

$$\mathbf{G}_1 = \frac{G_0}{2}\begin{pmatrix}\sqrt{3}\\ -1\end{pmatrix} \qquad \mathbf{G}_2 = G_0\begin{pmatrix}0\\ 1\end{pmatrix} \tag{3.6}$$

with

$$G_0 = \frac{4\pi}{\sqrt{3}\,a}. \tag{3.7}$$

The real space primitive lattice vectors read

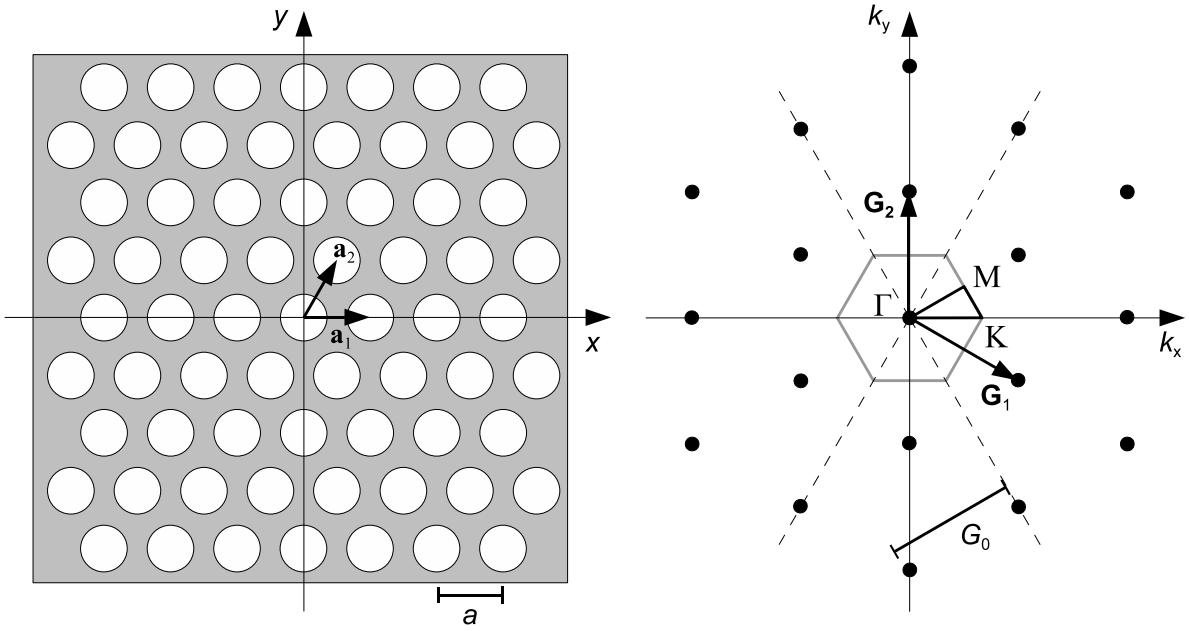

Fig. 3.3: A hexagonal lattice (left) and its representation in reciprocal space (right). The grey hexagon around the Γ-point indicates the Brillouin zone, the small triangle with the corners labelled Γ, M and K indicates the irreducible Brillouin zone. The dashed lines are a guide for the eye highlighting the six-fold symmetry.

$$\mathbf{a}_1 = a\begin{pmatrix}1\\0\end{pmatrix}$$
$$\mathbf{a}_2 = \frac{a}{2}\begin{pmatrix}1\\\sqrt{3}\end{pmatrix}. \tag{3.8}$$

In this context, the filling fraction F of a PhC is defined as the area of holes within the unit cell with respect to the area of the unit cell and reads in the case of a hexagonal lattice

$$F = \frac{2\pi r^2}{\sqrt{3}\, a^2}, \tag{3.9}$$

where r is the hole radius.

Due to the symmetry and due to Bloch's Theorem it is convenient to describe the propagation of light along the irreducible Brillouin zone as the main directions of the lattice. The dispersion relation as shown in Fig. 3.4 builds up as follows. For in-plane k-vector lengths $\beta<G_0/2$ the Brillouin zone completely encloses the guided mode and thus, the dispersion relation is the same as for the uncorrugated slab. As soon as $\beta>G_0/2$ the dispersion is folded at the Brillouin zone edge since guided modes with origin in the neighbouring Brillouin zones enter the first one. In ΓK direction the in-plane k-vector has to be larger than $\beta>G_0/3^{1/2}$. By consecutively following the intersections of the guided mode circles with the irreducible Brillouin zone edges the dispersion relation is obtained.

As an example all contributing circles are drawn in Fig. 3.5 for a reduced frequency of u=0.66. These circles stem from a shift of the original one centred at the Γ-point by reciprocal lattice vectors $\mathbf{G}=m_1\mathbf{G}_1+m_2\mathbf{G}_2$ with m_j an integer. Hence, they fulfil the Bragg condition

$$\boldsymbol{\beta}_d = \boldsymbol{\beta}_i + \mathbf{G} \tag{3.10}$$

with $\boldsymbol{\beta}_d$ the diffracted in-plane k-vector resulting from diffraction of an incident k-vector $\boldsymbol{\beta}_i$.

As soon as $\beta_d=|\boldsymbol{\beta}_i+\mathbf{G}|<k_0$ the formerly guided mode is folded above the light line and radiates into air. Thus, more light is extracted and the extraction efficiency enhances. In the above example the fundamental guided mode is diffracted into air for reduced frequencies $u>0.41$. Interestingly, if $u>2/3$ or equivalently $G_0<3^{1/2}k_0$, all guided modes are diffracted into air as the Brillouin zone fits completely within the extraction disk. The actual amount of

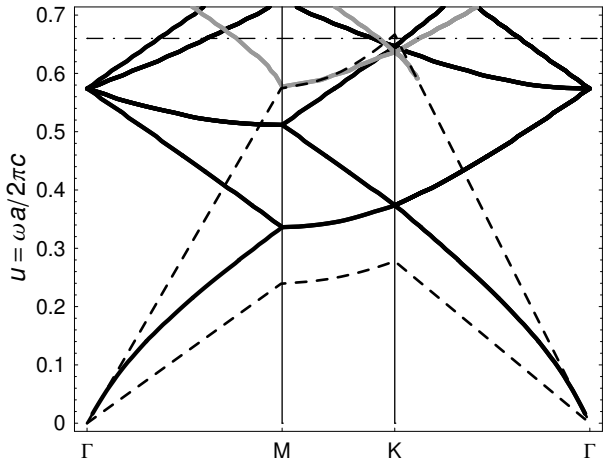

Fig. 3.4: Dispersion relation of the slab in Fig. 3.2c with an artificial hexagonal lattice, where $a=2.5L$ as in Fig. 3.2. The dash-dotted horizontal line indicates the reduced frequency corresponding to Fig. 3.5.

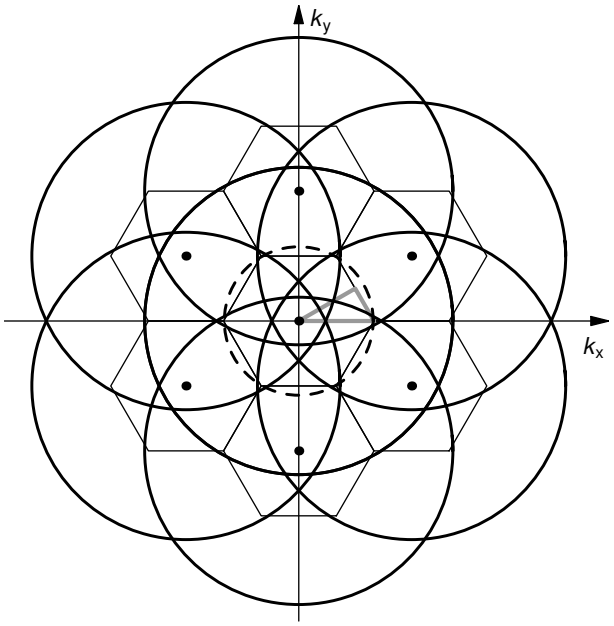

Fig. 3.5: In-plane contribution determining the intersections of the guided mode circles with the irreducible Brillouin zone at a reduced frequency $u=0.66$; in Fig. 3.4 the dotted horizontal line indicates this reduced frequency. For better visibility only the fundamental guided mode of the slab shown. The Brillouin zones are indicated by black lines, the irreducible Brillouin zone by thick grey lines. The black dashed circle encloses the extraction disk, $\beta=k_0$.

extracted light on the one hand depends on the absorption within the slab, see Fig. 2.8. On the other hand, the PhC pattern has to be optimised for best extraction. This will be discussed in detail in section 5.

3.3 Dispersion Relation: PhC Slab

For a real refractive index contrast $\Delta n=n_2-n_1>0$ between the material with $n=n_2$ and the hole with $n=n_1$ we can again draw our conclusions in analogy to quantum mechanics. Two modes contribute to the degeneracy for instance at the M-point, one with origin at the Γ-point, the other shifted by $\mathbf{G}_1$. Both have the same in-plane periodicity $\beta=G_0/2$, but their intensity profiles differ from each other in terms of their offset with respect to lattice. In the case of a one-dimensional potential in quantum mechanics this situation is sketched in Fig. 3.6 for the corresponding electronic states at the Brillouin zone edge.

As the electrons with the upper distribution are mainly located at the position of the ion cores, this distribution is related to lower energy compared to the distribution at the bottom where the electrons are mainly located between the atoms. Thus, a band gap opens up at the edge of the Brillouin zone. In electromagnetism the band gap comes into existence as the modes "see" different averaged refractive indices $<n>$ due to their mode profiles. The refractive index profile is the counterpart to the potential in quantum mechanics. The mode mainly located within the high index material has lower energy compared to the mode mainly located within the low index material [76], since $\omega=\beta c/<n>$.

In Fig. 3.7a the dispersion relation is shown for the PhC slab of Fig. 3.1c with $n_2=2.4$ and $n_1=2.2$. Thus, a band gap for instance at the M-point opens up. The dispersion is only shown for TE-like polarized modes. As these modes are not exclusively TE-polarized but with a portion TM-polarisation [79], the term "TE-like" is used. However, for thin slabs they are mainly TE-polarized. As the index contrast Δn increases, the band gap widens and

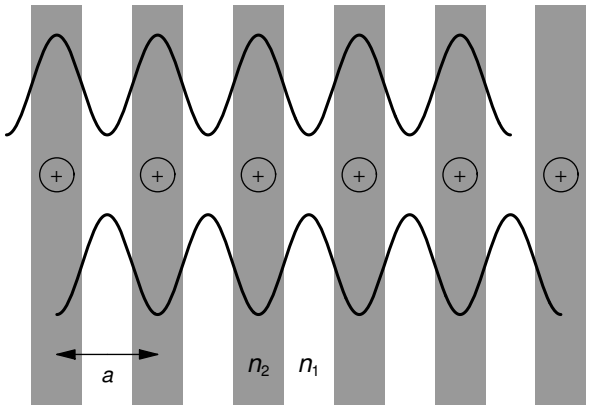

Fig. 3.6: Illustration of the probability density of electrons in a one-dimensional array of ion cores. Both have the same periodicity related to the edge of the Brillouin zone, i.e. $k=\pi/a$. The upper density function heaps the electrons at the position of the ion cores and thus, lowers the related energy compared to freely propagating electrons. In contrast, the bottom probability favours electrons between the atoms and thus, the related energy is higher. The difference in energy defines the band gap. In electromagnetism, the position of the ion cores corresponds to the high index material (dark rectangles) with refractive index $n=n_2$. The low index material (white spaces) has refractive index $n=n_1$.

overlaps with the other band gaps around the Γ and the K-point. For air holes, $n_1=1$, a complete band gap is obtained for TE-like modes, as shown in Fig. 3.7b, i.e. light with frequency inside the complete band gap cannot propagate within the PhC slab. Hence, emission only takes place into radiative modes and the extraction enhances [14]. Simulations of these structures reveal almost 100% extraction efficiency [13].

Apart from the band gaps that prohibit propagation of light at this frequency into a specific direction, a second important phenomenon arises from the band bending. As the refractive index contrast pushes the bands away from each other, the bands become more flat, especially at the edges of the band gaps. Flat bands offer a higher number of photonic states in k-space within a certain frequency range compared to steeper ones. Thus, the photonic density of states increases and consequently, with Fermi's Golden Rule (2.3) in mind, the radiative rate and the Purcell factor, respectively. From photoluminescence measurements [51] Purcell factors of up to 2 have been reported along with an external quantum efficiency of >50% if the emission is adjusted to flat bands above the light line. In contrast, the available photonic states in the case of a complete photonic band gap dramatically decrease resulting in a very

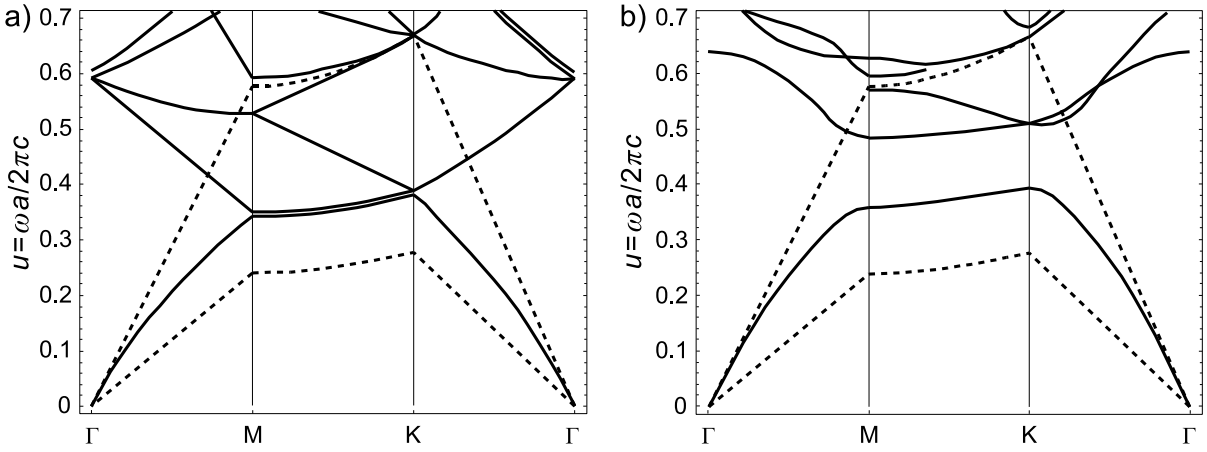

Fig. 3.7: (a) Dispersion relation of the TE-like polarized modes for a PhC slab with $n_2=2.4$, $n_1=2.2$, $a=2.5L$ and hole radius $r=0.35a$. (b) The same as (a) except $n_1=1$.

low radiative rate [13][14]. Therefore, it is more preferable to provide additional photonic states along with efficient diffraction instead of inhibiting the spontaneous emission into guided modes [51] even though the latter could provide 100% light extraction.

3.4 Conclusions for PhC LEDs

From the previous sections the question arises, how important are band bending effects in typical PhC LEDs with shallow two-dimensional PhCs. According to the considerations so far, the average index $\langle n \rangle$ seen by the modes is the deciding factor for the band bending. Apart from the real index contrast also the overlap of the modes with the PhC region determines $\langle n \rangle$. If we assume a material with refractive index n that is perturbed with a refractive index shift δn in some region, the associated shift in frequency that causes band bending can be estimated in first order to be [80]

$$\frac{\delta\omega}{\omega} = -\frac{\delta n}{n}\left(\text{fraction of} \int n^2 |E|^2 \text{ in perturbed regions}\right) \tag{3.11}$$

with ω the frequency and E the electric field amplitude of the mode without the perturbation. Thus, two regimes of PhC LEDs can be distinguished:

i) Band-bending can be neglected as the refractive index contrast is low and/or the PhC covers only a small volume within the LED, e.g. is only shallow etched. In this case, the dispersion relation of Fig. 3.4 is still valid and the PhC can be thought of as a diffraction grating. This will be referred to as weakly coupled PhCs and we deal with this regime throughout this work.

ii) The PhC covers a significant volume of the LED and the index contrast is large. Here, band gaps and an altered density of photonic states play an important role for light generation. Hence, the PhC is strongly coupled.

In order to determine the operating regime of a given PhC LED structure, spectrally resolved far field measurements have been proposed [21]. The far field contains the dispersion relation above the light line since the angle is related to the in-plane k-vector by

$$\boldsymbol{\beta} = n_{\text{amb}} k_0 \sin\theta_{\text{amb}} \begin{pmatrix} \cos\varphi \\ \sin\varphi \end{pmatrix} \tag{3.12}$$

with φ the azimuthal angle. Fig. 3.8a shows experimental data for a 1µm thick InGaN/GaN LED with a >400nm deeply etched hexagonal PhC, a bottom mirror and a 130nm thick transparent conductive oxide cover layer [33]. The far field was collected in the ΓM direction of the lattice. The dispersion relation is similar to the one shown in Fig. 3.4 around u=0.575. Hence, the four lines intersecting at u=0.495 stem from the same guided mode diffracted from different neighbouring Brillouin zones. The lines crossing the y-axis at u=0.515 indicate another guided mode. Also the azimuthally resolved emission pattern taken at a reduced frequency of u=0.592 as shown in Fig. 3.8b can be understood with Fig. 3.5 in mind. Since band gaps are hardly observed, this LED operates within the weak coupling regime. As an alternative to the far field measurement the dispersion relation above the light line can also be gathered by spectral reflectometry [81].

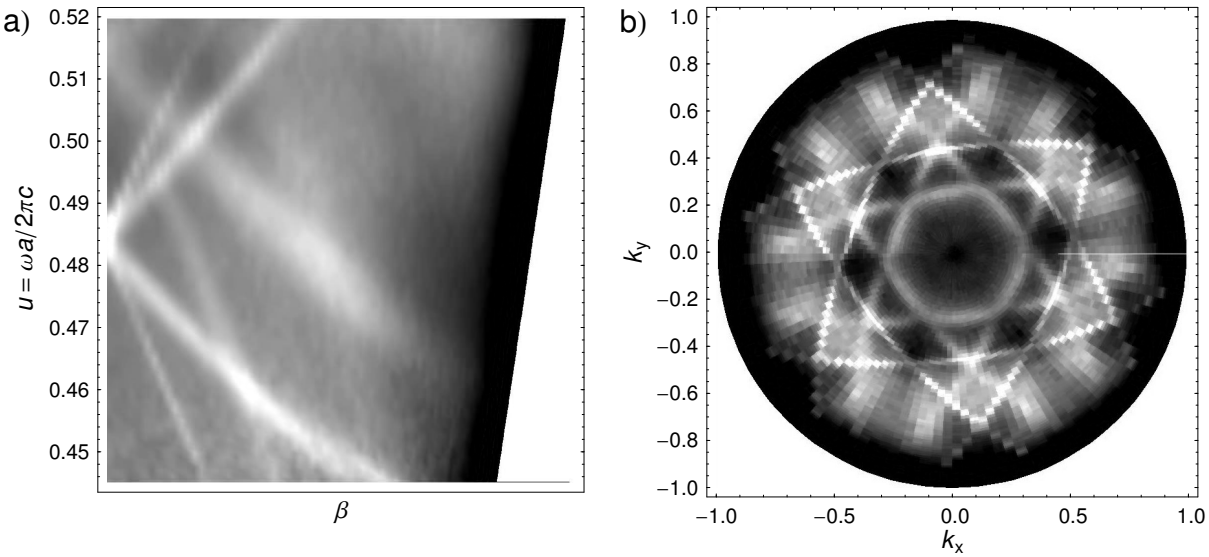

Fig. 3.8: (a) Measured dispersion relation of a GaN-based LED with overall thickness of ~1 µm, a >400 nm etched PhC with pitch a = 274 nm, a bottom mirror and an ITO cover-layer. The band intersection at u = 0.495 qualitatively agrees with the bands in Fig. 3.4 at u = 0.575. (b) Azimuthally resolved far field for u = 0.592 revealing a Star-of-David shaped pattern similar to the one shown in Fig. 3.5.

4 Theoretical Methods

In this chapter the simulation methods used throughout this work are summarized. First of all, a widely used method is presented that handles co-planar layer stacks and yields the extraction efficiency of LEDs along with the Purcell factor. Even though this method can be extended to structures with surface texturing [29][82][83], it is limited to periodical surfaces and to single frequency calculations. Afterwards we describe two methods for structured LEDs. The first one is applicable to shallow etched PhC LEDs since a perturbational treatment of the PhC is utilized. With this diffraction model a clear insight into the basic mechanisms of PhC LEDs is possible. Besides the detailed discussion regarding PhC LEDs in chapter 5 is based upon this model. The second one is the finite-difference time-domain (FDTD) method that solves Maxwell's equations fully vectorial in three dimensions [41]. Due to the tremendous demand in computational time and resources along with the huge parameter space of PhC LEDs a general optimisation of these is not possible with FDTD. However, as this method handles any surface structuring it will be used for a quantitative comparison between PhC LEDs and standard thin-film LEDs with random surface texture in chapter 7. Furthermore, we will verify our conclusions and results obtained from the diffraction model with FDTD.

4.1 Transfer Matrix with a Dipole Source

The aim of the method described here is to calculate the extraction efficiency of co-planar layer stacks along with the Purcell factor and the angular emission distribution while taking into account the interference effects within the layer stack stemming from reflections at the layer interfaces (RCLED effect).

In order to determine the main principles of this method consider for instance the three layer stack as shown in Fig. 4.1. For a given frequency and in-plane k-vector two propagating plane waves contribute to the electric field in layer 1 as no coupling of different in-plane k-vectors is possible: firstly, light generated upwards and secondly, light generated downwards and reflected at the interface between layer 2 and layer 3, similar to Fig. 2.9a. The transmission of this superposition gives the electric field E_1 in the upper layer 1 [40]

$$E_1 = \frac{t_1\left(A_- + r_3 A_+\right)}{1 - r_1 r_3}, \tag{4.1}$$

with $A_\pm$ the source distribution in $\pm z$-direction and t_j (r_j) the amplitude transmission (reflection) coefficients including phase factors corresponding to the propagation of light from the source position towards the layer interfaces. The denominator determines the confinement of the fields within the cavity between layers 1 and 3. For reflectivities r_1 and r_3 approaching unity highly confined modes are obtained; the lower the product the less confined is the corresponding mode. For the electric field in layer 3 E_3 and the field within the source layer

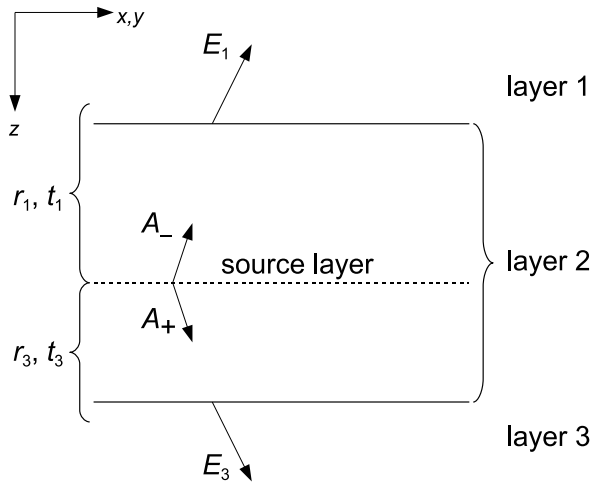

Fig. 4.1: Sketch of a three layer system. The source is embedded within layer 2. Along with the electric field in layer 1 and 3 also the source amplitudes $A_{\pm}$ are depicted. The reflection and transmission coefficients r_j and t_j include both the pure Fresnel reflection coefficient between two layers and phase factors owing to the propagation of light from the source position towards the layer interface.

E_2 similar expressions to (4.1) can be derived [39] and [40]. From this it is possible to determine the impact of the cavity on the source. We already used this method for the calculation of the extraction efficiency and the Purcell factor as shown in Fig. 2.9b and the emission distribution in Fig. 2.10.

At this point, two issues remain open: the source distribution and the generalization of the three layer system to a system with an arbitrary number of layers.

4.1.1 Source Distributions: Bulk, Quantum Wells, and Wurtzite Structure

The source distribution $A_{\pm}$ itself depends on the electron-hole-recombination process. Classically, this recombination can be described by an isotropic source with its separation into a vertically (v) oriented dipole only radiating TM-polarisation and two horizontally (h) oriented dipoles, one for TE and the other for TM-polarisation [40]

$$\begin{aligned} A_{\pm}^{\mathrm{v,TM}} &= \pm\sqrt{\frac{3}{8\pi}}\sin\theta_2 = \pm\sqrt{\frac{3}{8\pi}}\frac{\beta}{k_2} \\ A_{\pm}^{\mathrm{h,TM}} &= \pm\sqrt{\frac{3}{16\pi}}\cos\theta_2 = \pm\sqrt{\frac{3}{16\pi}}\sqrt{1-\left(\beta/k_2\right)^2}\,, \\ A_{\pm}^{\mathrm{h,TE}} &= \pm\sqrt{\frac{3}{16\pi}} \end{aligned} \tag{4.2}$$

with θ_2 the propagation angle of the plane wave inside layer 2 and k_2 the corresponding k-vector. By replacing the propagation angle with the in-plane k-vector it is possible to include the evanescent fraction, $\beta > k_2$, of the dipole emission into the calculations. Thus, also the coupling of an emitter with surface plasmons, see section 6, can be considered quantitatively. The coefficients ensure the correct weighting of each dipole. For instance, the emitted radiant intensity for an isotropic emitter is then given by

$$I_{\mathrm{iso}} = \frac{2}{3} I_{\mathrm{h}} + \frac{1}{3} I_{\mathrm{v}} = \frac{2}{3}\left(\frac{3}{16\pi} + \frac{3}{16\pi} \cos^2 \theta \right) + \frac{1}{3} \frac{3}{8\pi} \sin^2 \theta = \frac{1}{4\pi}, \tag{4.3}$$

The weighting of the horizontal (vertical) fraction of the radiant intensity I_{h} (I_{v}) with 2/3 (1/3) accounts for the decomposition of an isotropic source into two horizontally (one vertically) aligned dipole, i.e. one for each spatial direction.

However, the assumption of an isotropic emission being used up to now only holds for spatially homogeneous crystal structures, like bulk GaAs with its Zinc-Blende structure. In this case, no preferential direction exists and thus, no preferred dipole orientation. In contrast, for quantum wells the direction perpendicular to the well significantly differs from the in-plane directions due to the heterostructure. For transitions between confined conduction bands and heavy hole valence band states, which usually are the fundamental transitions, the dipole oriented perpendicular to the well is suppressed and thus only horizontal dipoles exist. A similar break in spatial symmetry occurs in semiconductors with an intrinsic preferential direction resulting from the crystal structure. For example in the case of GaN with its Wurtzite structure the *c*-axis defines a preferred direction. For GaN grown along the *c*-axis the dominating electron-hole recombination process can be described by horizontal dipoles. Hence, throughout this work only in-plane oriented dipoles will be taken into account as all LEDs under investigation are GaN-based and/or have quantum wells. The issues related to the dipole orientation and the electronic transition matrix element with a special focus on GaN are discussed in more detail in [24].

4.1.2 Transfer Matrix

Even though the three layer stack as sketched in Fig. 4.1 is a very simple system it already includes the extension to an arbitrary LED layer stack. The only information we need to know about layer 1 and 3 are their reflection and transmission coefficients in relation to layer 2. Thus, in a general structure one simply replaces the layer stack above and below the active region with an artificial layer with the same properties in terms of reflection and transmission. The latter serve as an input for e.g. (4.1).

In order to derive *r* and *t* of an arbitrary layer stack the same mathematics is applied as in the case of electron tunnelling through a potential barrier, for instance. The following results hold for TE-polarized light (similar expressions for TM), i.e. the electric field is oriented in the *x*-direction. The electric field ξ_{j} in each layer *j* is assumed as a superposition of upward and downward propagating plane waves

$$\xi_j(z) = A_{\mathrm{j}} e^{i\gamma_{\mathrm{j}}(z - z_{\mathrm{j}})} + B_{\mathrm{j}} e^{-i\gamma_{\mathrm{j}}(z - z_{\mathrm{j}})}, \tag{4.4}$$

with

$$\gamma_{\mathrm{j}} = \sqrt{n_{\mathrm{j}}^2 \, k_0^2 - \beta^2} \tag{4.5}$$

the k-vector component perpendicular to the layer interfaces, n_{j} the refractive index of the *j*-th layer and z_{j} the position of the interface between layer $j-1$ and layer *j*. The amplitudes A_{j} and B_{j} are determined by the electromagnetic boundary conditions between two layers that in general read

$$\begin{aligned}
\left(\mathbf{D}_{j+1}-\mathbf{D}_{j}\right)\cdot\mathbf{e}_{z} &= \sigma_{s}\\
\left(\mathbf{B}_{j+1}-\mathbf{B}_{j}\right)\cdot\mathbf{e}_{z} &= 0\\
\mathbf{e}_{z}\times\left(\mathbf{E}_{j+1}-\mathbf{E}_{j}\right) &= 0\\
\mathbf{e}_{z}\times\left(\mathbf{H}_{j+1}-\mathbf{H}_{j}\right) &= \mathbf{j}_{s}
\end{aligned} \tag{4.6}$$

with $\mathbf{e}_z$ the unit vector in z-direction. The surface charge σ_s and the surface current density $\mathbf{j}_s$ are neglected in the following. Due to the third and the last equation of (4.6) the tangential components of both the electric and the magnetic field are continuous across the interface. Thus, in the case of TE-polarisation the amplitudes A_j, B_j, A_{j+1} and B_{j+1} of two adjacent layers are related to each other by

$$\begin{aligned}
\xi_{j}\big|_{z=z_{j+1}} &= \xi_{j+1}\big|_{z=z_{j+1}}\\
\left.\frac{\partial\xi_{j}}{\partial z}\right|_{z=z_{j+1}} &= \left.\frac{\partial\xi_{j+1}}{\partial z}\right|_{z=z_{j+1}}
\end{aligned} \tag{4.7}$$

as $\mathbf{H}=(0,H_y,H_z)$ and $H_y \sim \partial E/\partial z$ owing to the third equation of (3.2). From (4.7) the amplitudes of the next layer j+1 can be calculated from the amplitudes in layer j by the matrix $\mathbf{T}_j$

$$\begin{pmatrix} A_{j+1}\\ B_{j+1}\end{pmatrix} = \underbrace{\frac{1}{2\gamma_{j+1}}\begin{pmatrix}\left(\gamma_{j+1}+\gamma_{j}\right)e^{i\gamma_j d_j} & \left(\gamma_{j+1}-\gamma_{j}\right)e^{-i\gamma_j d_j}\\ \left(\gamma_{j+1}-\gamma_{j}\right)e^{i\gamma_j d_j} & \left(\gamma_{j+1}+\gamma_{j}\right)e^{-i\gamma_j d_j}\end{pmatrix}}_{\mathbf{T}_j}\cdot\begin{pmatrix} A_{j}\\ B_{j}\end{pmatrix}, \tag{4.8}$$

with the thickness $d_j=z_{j+1}-z_j$ of the j-th layer. Consequently, the amplitudes in the last layer of an N layer stack are derived from the first by the transfer matrix $\mathbf{T}$

$$\begin{pmatrix} A_{N}\\ B_{N}\end{pmatrix} = \underbrace{\mathbf{T}_{N-1}\cdot\ldots\cdot\mathbf{T}_{1}}_{\mathbf{T}}\cdot\begin{pmatrix} A_{1}\\ B_{1}\end{pmatrix}. \tag{4.9}$$

Hence, the reflection coefficient r and the transmission coefficient t for an arbitrary layer stack can be calculated by

$$\begin{pmatrix} t\\ 0\end{pmatrix} = \mathbf{T}\cdot\begin{pmatrix} 1\\ r\end{pmatrix}. \tag{4.10}$$

Since this transfer matrix has the drawback of being numerically unstable as small numerical errors within the exponential functions build up rapidly, we used the so-called scattering matrix. Instead of linking the fields on the bottom of the stack with the fields on top as is the case for the transfer matrix, the scattering matrix $\mathbf{S}$ links the incoming waves A_1 and B_N to the outgoing waves A_N and B_1 [84]

$$\begin{pmatrix} A_{N}\\ B_{1}\end{pmatrix} = \mathbf{S}\cdot\begin{pmatrix} A_{1}\\ B_{N}\end{pmatrix}. \tag{4.11}$$

The reflection and transmission coefficient ensue from

$$\begin{pmatrix} t \\ r \end{pmatrix} = \mathbf{S} \cdot \begin{pmatrix} 1 \\ 0 \end{pmatrix}. \tag{4.12}$$

4.2 Diffraction Model

Based upon the conclusions from section 3.4 we now derive a simulation method for PhC LEDs that handles the PhC as a perturbation of the co-planar LED layer stack. Hence, first of all the modes of the LED are calculated. Afterwards coupled mode theory is applied in order to obtain the amount of diffracted intensity between modes. The PhC enters the mode calculation by its average dielectric function $\varepsilon_{\mathrm{PhC}}$, that is given by $\varepsilon_{\mathrm{PhC}}=F\varepsilon_{\mathrm{air}}+(1-F)\varepsilon_{\mathrm{SC}}$. Fig. 4.2 shows a general setup of a PhC LED along with a guided and a radiative mode.

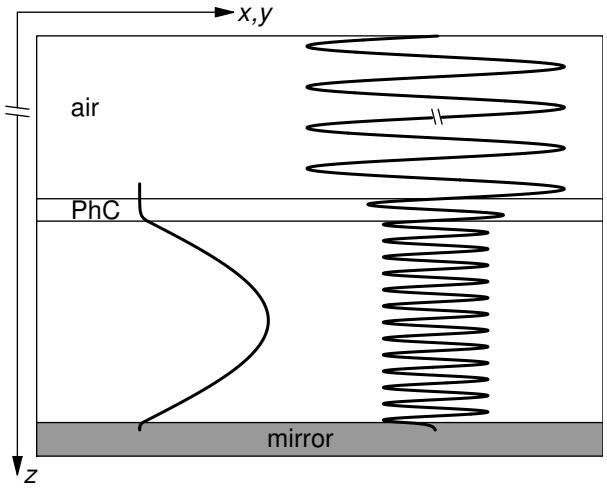

Fig. 4.2: General setup of a PhC thin-film LED along with field amplitude profiles of a guided and a radiative mode.

4.2.1 Eigensolutions of a Co-Planar Layer Stack

The method to determine the eigensolutions of an arbitrary co-planar layer stack described in the following is given in detail in [77] for TE-polarized, i.e. $\mathbf{E}=(E,0,0)$, guided modes. Hence, only a brief summary is presented and extended to the calculation of radiative modes.

In the case of a co-planar layer stack as depicted in Fig. 4.3 the master equation for the electric field (3.4) reads

$$\left[\nabla^2 + \frac{\omega^2}{c^2}\varepsilon(z)\right] E_{\mathrm{m}}(\mathbf{r}) = 0, \tag{4.13}$$

where E_{m} is the m-th eigensolution. In order to derive (4.13) the Grassmann[3] identity has been applied along with the assumption $\nabla\cdot(\varepsilon\mathbf{E})=\varepsilon\nabla\cdot\mathbf{E}=0$. The latter is justified, even though ε is z-dependent, as the discontinuities are handled by the boundary conditions (4.6) between two adjacent layers.

[3] $\mathbf{a}\times(\mathbf{b}\times\mathbf{c}) = \mathbf{b}(\mathbf{a}\cdot\mathbf{c}) - \mathbf{c}(\mathbf{a}\cdot\mathbf{b})$

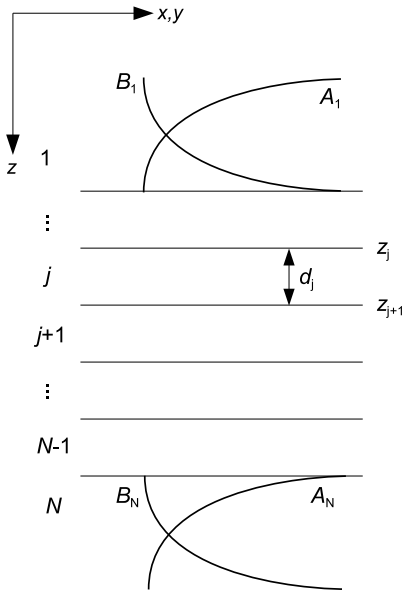

Fig. 4.3: Sketch of a co-planar stack with N layers. The first layer corresponds to the ambient medium, the last to the mirror in the case of thin-film LEDs. Apart from the layers also the field amplitudes in the first and the N-th layer are depicted in the case $\beta > n_1 k_0$ and $\beta > n_N k_0$. A mode is confined to the stack if $A_1 = B_N = 0$.

Due to the homogeneity of the slab in x and y, the eigensolutions of (4.13) can be separated into a vertical field profile $U_\mathrm{m}(z)$ and a plane wave in lateral directions

$$E_\mathrm{m}(\mathbf{r}) = U_\mathrm{m}(z)\, e^{-i\,\boldsymbol{\beta}_\mathrm{m}\cdot\mathbf{r}_\parallel}, \tag{4.14}$$

with $\mathbf{r}_\parallel=(x,y)$ and the vertical field profile

$$U_\mathrm{m}(z) = \sum_{\mathrm{j}=1}^{\mathrm{N}} \Theta_\mathrm{j}(z)\,\xi_\mathrm{j}(z), \tag{4.15}$$

with N the number of layers and

$$\Theta_\mathrm{j}(z) = \begin{cases} 1 & z_\mathrm{j} < z \le z_{\mathrm{j}+1} \\ 0 & \text{else} \end{cases}. \tag{4.16}$$

For better readability the field inside each layer ξ_j and the vertical k-vector component γ_j are not labelled with the mode index m. The vertical mode profile is normalized according to [85]

$$\int U_\mathrm{m}^*(z)\, U_\mathrm{k}(z)\, dz = \frac{2\,\omega\,\mu_0}{\beta_\mathrm{m}}\,\delta_\mathrm{mk}. \tag{4.17}$$

With the help of the transfer matrix (4.9) the eigensolutions of (4.13) can be found, since an eigensolution is confined to the layer stack when the field decays exponentially outside the stack, i.e. $\beta_\mathrm{m} > n_1 k_0$ and simultaneously $\beta_\mathrm{m} > n_\mathrm{N} k_0$. Thus, the normal k-vector components γ_1 and γ_N are purely imaginary. Consequently, the amplitudes $A_1 = B_\mathrm{N} = 0$ have to vanish in order to avoid an exponential growth of the fields in layer 1 and N in direction away from the stack, see Fig. 4.3. For $A_1 = 0$ and $B_1 = 1$ guided modes are determined by the roots of the T_{22} component of $\mathbf{T}$

$$\begin{pmatrix} A_{\mathrm{N}} \\ B_{\mathrm{N}} \end{pmatrix} = \mathbf{T} \cdot \begin{pmatrix} 0 \\ 1 \end{pmatrix} = \begin{pmatrix} T_{11} & T_{12} \\ T_{21} & T_{22} \end{pmatrix} \cdot \begin{pmatrix} 0 \\ 1 \end{pmatrix} \tag{4.18}$$

as $B_{\mathrm{N}}=0$ in this case. The only unknown in (4.18) is the in-plane k-vector length β. It should be mentioned here, that an infinite number of modes correspond to the eigenvalue β_{m} according to (4.14), each having different in-plane propagation direction $\boldsymbol{\beta}_{\mathrm{m}}/\beta_{\mathrm{m}}$. Wherever it simplifies the treatment this degenerate set of modes is referred to as a single mode. The imaginary part of the eigenvalue determines the absorption coefficient α_{m} of the guided mode

$$\alpha_{\mathrm{m}} = 2\left|\mathrm{Im}(\beta_{\mathrm{m}})\right| \tag{4.19}$$

However, when referring to the eigenvalue or the in-plane k-vector length only the real part is taken into account.

In contrast to guided modes, radiative modes are not confined to the layer stack and hence, cannot be calculated with (4.18). Furthermore, an infinite number exists as they extend into free space. In order to allow for the numerical treatment of these modes, the ambient medium is truncated to a layer with finite thickness. For the results presented in this work, the thickness of this layer is 200 times the emission wavelength in order to create a quasi-continuum of radiative modes. The calculation of the radiative modes itself is carried out by solving for standing waves within this extended layer stack. Since the power flux of standing waves in z-direction has to be zero, the amplitudes within the ambient layer are assumed to be $A_1=-B_1$. The condition $B_{\mathrm{N}}=0$ still holds for thin-film LEDs as the radiative modes are confined by the mirror. Thus, according to (4.18) radiative modes obey

$$\begin{pmatrix} A_{\mathrm{N}} \\ 0 \end{pmatrix} = \begin{pmatrix} T_{11} & T_{12} \\ T_{21} & T_{22} \end{pmatrix} \cdot \begin{pmatrix} 1 \\ -1 \end{pmatrix} \Leftrightarrow T_{21} = T_{22}\,. \tag{4.20}$$

Although the above method is derived for LEDs in thin-film configuration, it can readily be extended to LEDs with transparent or absorptive substrates.[4]

In order to obtain all guided and radiative modes supported by a layer stack, the following criterion is used. Two modes can be distinguished by the number of roots of their field profile. The lowest order guided mode has zero roots, the next higher order guided mode has one root, etc. Hence, a complete set of guided modes is obtained, if every possible number of roots up to some maximum number $N_{\max}$ is determined. The maximum number $N_{\max}$ for guided modes is calculated from a test field profile with $\beta=(n_1+\delta n)k_0$ with $\delta n=10^{-15}$. For radiative modes the maximum number of roots is determined from a test field profile with $\beta=0$.

4.2.2 Coupled Mode Theory

Due to the perturbation of the co-planar layer stack by the PhC, the modes of the slab get coupled to each other according to Bragg' law (3.10). In order to derive the relevant properties of the modes, firstly coupled mode theory [86] is applied to a one-dimensional

[4] The numerical implementation of the mode search was based upon the derivation given in [77]. Here, the normal k-vector component is defined by $\gamma_{\mathrm{j}} = \sqrt{\beta^2 - n_{\mathrm{j}}^2 k_0^2}$ and the electric field within the j-th layer by $\xi_j(z) = A_{\mathrm{j}} e^{\gamma_{\mathrm{j}}(z-z_{\mathrm{j}})} + B_{\mathrm{j}} e^{-\gamma_{\mathrm{j}}(z-z_{\mathrm{j}})}$. Thus, the transfer matrix differs and the condition for guided modes requires $A_{\mathrm{N}}=0$ or $T_{11}=0$ and for radiative modes $T_{11}=T_{12}$ in contrast to (4.18) and (4.20), respectively. For the numerical determination of the complex eigenvalue β the built-in function *FindRoot* of Mathematica 5.2 is used.

grating and modes propagating perpendicular to the grooves. Afterwards the results are extended to the two-dimensional case.

By adding the perturbation $\Delta\varepsilon(x,z)$ due to a one-dimensional PhC the unperturbed equation (4.13) assumes the form

$$\left[\nabla^2 + \frac{\omega^2}{c^2}\left(\varepsilon(z) + \Delta\varepsilon(x,z)\right)\right] E(x,z) = 0\,, \tag{4.21}$$

where the solution $E(x,z)$ is taken as a superposition of both guided and radiative modes of the unperturbed layer stack

$$E(x,z) = \sum_{\mathrm{m}} a_{\mathrm{m}}(\mathrm{x})\, U_m(\mathrm{z})\, e^{-i\beta_{\mathrm{m}} x}\,. \tag{4.22}$$

After multiplying (4.21) with the complex conjugate of the k-th mode and integrating over the transversal direction z one obtains by additionally applying the unperturbed equation (4.13) and the orthonormality condition (4.17)

$$\frac{\partial a_{\mathrm{k}}(x)}{\partial x} = -\frac{i\varepsilon_0\omega}{4}\sum_{\mathrm{m}} a_{\mathrm{m}}(x)\, e^{-i(\beta_{\mathrm{m}}-\beta_{\mathrm{k}})x} \int U_{\mathrm{k}}^*(z)\,\Delta\varepsilon(x,z)\,U_{\mathrm{m}}(z)\,dz\,. \tag{4.23}$$

The second derivative has been neglected owing to the slowly varying amplitude approximation $\partial^2 a_{\mathrm{m}}/\partial x^2 \ll \beta_{\mathrm{m}}\partial a_{\mathrm{m}}/\partial x$.

At this point it is helpful to introduce the Fourier transform of the periodic dielectric function [87]

$$\Delta\varepsilon(x,z) = \sum_{G} \Theta_{\mathrm{PhC}}(z)\,\Delta\tilde{\varepsilon}_{\mathrm{G}}\; e^{-iGx}\,, \tag{4.24}$$

with $\Theta_{\mathrm{PhC}}(z)=1$ for vertical positions inside the PhC layer and zero elsewhere. Since the average dielectric function of the PhC is already included into the mode calculation the fundamental Fourier amplitude vanishes, i.e. $\Delta\varepsilon_{\mathrm{G=0}}=0$. Inserting the Fourier transform (4.24) into (4.23) results in

$$\frac{\partial a_{\mathrm{k}}(x)}{\partial x} = -\frac{i\varepsilon_0\omega}{4}\sum_{\mathrm{m}}\sum_{G} a_{\mathrm{m}}(x)\, e^{-i(\beta_{\mathrm{m}}-\beta_{\mathrm{k}}-G)x}\;\Delta\tilde{\varepsilon}_G \underbrace{\int_{\mathrm{PhC}} U_{\mathrm{k}}^*(z)\,U_{\mathrm{m}}(z)\,dz}_{\kappa_{\mathrm{km}}}\,, \tag{4.25}$$

where the integral κ_{km} is only taken over the PhC layer and determines the coupling strength of the modes k and m within the PhC. Integration of (4.25) in x-direction up to some length L yields

$$a_{\mathrm{k}}(L) = -\frac{i\varepsilon_0\omega}{4}\sum_{\mathrm{m}}\sum_{G} a_{\mathrm{m}}\;\Delta\tilde{\varepsilon}_G\;\kappa_{\mathrm{km}}\,\frac{1-e^{-i\Delta L}}{i\Delta}\,, \tag{4.26}$$

with $\Delta=\beta_{\mathrm{m}}-\beta_{\mathrm{k}}-G$ and the assumption $a_{\mathrm{k}}(0)=0$. Furthermore, the coefficient $a_{\mathrm{m}}(x)=a_{\mathrm{m}}$ has been assumed constant as the coupling is supposed to be weak. Incoherently summing (4.26) up after taking the squared modulus enables to replace the last factor in (4.26) by the Bragg condition $\Delta=0$ in the limit of large L

$$\left|\frac{1-e^{-i\Delta L}}{i\Delta}\right|^2 \xrightarrow{L\to\infty} 8\pi\, L\,\delta(\Delta) \tag{4.27}$$

Thus, the diffraction rate Γ_k into the k-th mode is obtained as

$$\Gamma_\mathrm{k} = \frac{\left|a_\mathrm{k}(L)\right|^2}{L} = \frac{\pi\,\varepsilon_0^2\omega^2}{2}\sum_\mathrm{m}\left|a_\mathrm{m}\right|^2\left|\Delta\tilde{\varepsilon}_{\beta_\mathrm{m}-\beta_\mathrm{k}}\right|^2\left|\kappa_\mathrm{km}\right|^2, \tag{4.28}$$

with

$$\Delta\tilde{\varepsilon}_{\beta_m-\beta_k} = \begin{cases}\Delta\tilde{\varepsilon}_G & G=\beta_\mathrm{m}-\beta_\mathrm{k}\\ 0 & \text{else}\end{cases}. \tag{4.29}$$

In order to extend these results to the calculation of two-dimensional PhCs, every in-plane propagation direction has to be taken into account. Thus, the diffraction rate from a mode propagating with in-plane direction $\boldsymbol{\beta}_\mathrm{m}/\beta_\mathrm{m}$ into another one propagating in direction $\boldsymbol{\beta}_\mathrm{k}/\beta_\mathrm{k}$ is given by

$$\Gamma(\boldsymbol{\beta}_\mathrm{m}\to\boldsymbol{\beta}_\mathrm{k}) \propto \left|\Delta\tilde{\varepsilon}_{\boldsymbol{\beta}_\mathrm{m}-\boldsymbol{\beta}_\mathrm{k}}\right|^2\left|\kappa_\mathrm{km}\right|^2, \tag{4.30}$$

and consequently

$$\Delta\tilde{\varepsilon}_{\boldsymbol{\beta}_\mathrm{m}-\boldsymbol{\beta}_\mathrm{k}} = \begin{cases}\Delta\tilde{\varepsilon}_\mathbf{G} & \mathbf{G}=\boldsymbol{\beta}_\mathrm{m}-\boldsymbol{\beta}_\mathrm{k}\\ 0 & \text{else}\end{cases}. \tag{4.31}$$

Hence, the overall diffraction rate $\Gamma_{\mathrm{m}\to\mathrm{amb}}$ of a guided mode β_m into the ambient medium is obtained by considering every in-plane propagation direction $\boldsymbol{\beta}_\mathrm{m}/\beta_\mathrm{m}$ of the guided mode and every radiative mode along with its propagation direction

$$\Gamma_{\mathrm{m}\to\mathrm{amb}} \propto \sum_{\boldsymbol{\beta}_\mathrm{m}/\beta_\mathrm{m}}\sum_{\substack{\boldsymbol{\beta}_\mathrm{k}\\ \beta_\mathrm{k}<k_\mathrm{amb}}}\left|\Delta\tilde{\varepsilon}_{\boldsymbol{\beta}_\mathrm{m}-\boldsymbol{\beta}_\mathrm{k}}\right|^2\left|\kappa_\mathrm{km}\right|^2. \tag{4.32}$$

From (4.30) the amount of diffracted intensity I_d is calculated by multiplying the diffraction rate with the amount of spontaneous emission B_m into each mode

$$I_\mathrm{d}(\boldsymbol{\beta}_\mathrm{m}\to\boldsymbol{\beta}_\mathrm{k}) \propto B_\mathrm{m}\left|\Delta\tilde{\varepsilon}_{\boldsymbol{\beta}_\mathrm{m}-\boldsymbol{\beta}_\mathrm{k}}\right|^2\left|\kappa_\mathrm{km}\right|^2, \tag{4.33}$$

with

$$B_\mathrm{m} = \frac{\beta_\mathrm{m}}{2\omega\mu_0}\int_{\substack{\text{active}\\ \text{region}}}\left|U_\mathrm{m}(z)\right|^2 dz \tag{4.34}$$

the overlap of the mode profile with the active region. In analogy, we can define the overlap of the mode profile with the PhC layer by

$$C_{\mathrm{m}} = \frac{\beta_{\mathrm{m}}}{2\omega\mu_0} \int_{\mathrm{PhC}} \left|U_{\mathrm{m}}(z)\right|^2 dz = \kappa_{mm} \tag{4.35}$$

According to (4.33) it is evident that a large amount of intensity is diffracted from one mode to another when the initial mode gains a lot of spontaneous emission and the two modes couple significantly with each other. Additionally, the corresponding reciprocal lattice vector should support a high Fourier intensity.

The azimuthally averaged far field pattern $I_{\mathrm{d}}(\theta)$ resulting from diffraction of guided modes into the extraction cone is then given by summation over every in-plane direction of every guided mode and summation over every diffraction process resulting in the same radiative mode β_{k}

$$I_{\mathrm{d}}(\theta_{\mathrm{k}}) \propto \frac{1}{\sin\theta_{\mathrm{k}}} \sum_{\boldsymbol{\beta}_{\mathrm{m}}} \sum_{\boldsymbol{\beta}_{\mathrm{k}}/\beta_{\mathrm{k}}} B_{\mathrm{m}} \left|\Delta\tilde{\varepsilon}_{\boldsymbol{\beta}_{\mathrm{m}}-\boldsymbol{\beta}_{\mathrm{k}}}\right|^2 \left|\kappa_{\mathrm{km}}\right|^2 , \tag{4.36}$$

with $\sin\theta_{\mathrm{k}} = \beta_{\mathrm{k}}/k_{\mathrm{amb}}$.

According to Fig. 4.4 diffraction of a guided mode β_{m} results only in radiative modes with in-plane k-vector $|G-\beta_{\mathrm{m}}| < \beta_{\mathrm{k}} < k_{\mathrm{amb}}$. Thus, the explicit sum over every possible in-plane direction in (4.32) and (4.36) can be replaced by a sum over every reciprocal lattice vector length G supported by the PhC along with a sum over every in-plane k-vector length of the radiative modes obeying the above condition. Therefore, the overall diffraction rate $\Gamma_{\mathrm{m}\to\mathrm{amb}}$ (4.32) is given by

$$\Gamma_{\mathrm{m}\to\mathrm{amb}} \propto \sum_{G} \sum_{|G-\beta_{\mathrm{m}}|<\beta_{\mathrm{k}}<k_{\mathrm{amb}}} \left|\Delta\tilde{\varepsilon}_{G,\mathrm{tot}}\right|^2 \left|\kappa_{\mathrm{km}}\right|^2 \tag{4.37}$$

and the azimuthally averaged far field pattern $I_{\mathrm{d}}(\theta)$ transforms into

$$I_{\mathrm{d}}(\theta_{\mathrm{k}}) \propto \frac{1}{\sin\theta_{\mathrm{k}}} \sum_{\beta_{\mathrm{m}}} \sum_{G} B_{\mathrm{m}} \left|\Delta\tilde{\varepsilon}_{G,\mathrm{tot}}\right|^2 \left|\kappa_{\mathrm{km}}\right|^2 \Theta\left(\beta_{\mathrm{k}} - \left|G-\beta_{\mathrm{m}}\right|\right), \tag{4.38}$$

where the total Fourier intensity of reciprocal lattice vectors with equal length is given by

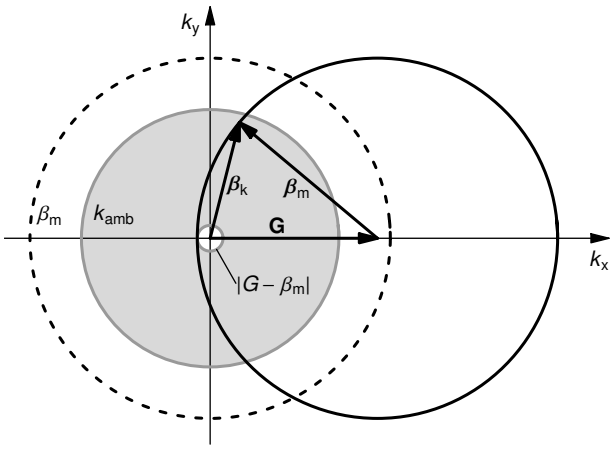

*Fig. 4.4: Ewald-like construction according to Fig. 3.5 showing every possible diffracted k-vector (black solid circle) resulting from diffraction of a guided mode (black dashed circle) with eigenvalue β_{m} by a reciprocal lattice vector **G**. Bragg's law is shown for one in-plane propagation direction $\boldsymbol{\beta}_{\mathrm{m}}$. The diffraction process within the extraction disk only results in diffracted k-vectors with length $|G-\beta_{\mathrm{m}}| < \beta_{\mathrm{k}} < k_{\mathrm{amb}}$ (light grey area).*

$$\left|\Delta\tilde{\varepsilon}_{G,\mathrm{tot}}\right|^2 = \sum_{\substack{\mathbf{G} \\ |\mathbf{G}|=G}} \left|\Delta\tilde{\varepsilon}_{\mathbf{G}}\right|^2 \tag{4.39}$$

and

$$\Theta\left(\beta_{\mathrm{k}} - \left|G - \beta_{\mathrm{m}}\right|\right) = \begin{cases} 1 & \beta_{\mathrm{k}} > \left|G - \beta_{\mathrm{m}}\right| \\ 0 & else \end{cases}. \tag{4.40}$$

In general, if light is diffracted from mode β_{m} to mode β_{k} the reverse direction is also possible. However, as we are interested in diffraction from guided modes into radiative modes, the diffraction from the latter into the former can be neglected. As discussed in [19], if the confinement of the radiative modes within the cavity is small compared to the guided modes, extraction of light is more rapid than back-diffraction. In the case of GaN-to-air (AlGaInP-to-air) the reflectivity of this interface is as low as 17% (31%) and hence, only weak confinement of the radiative modes is expected. In contrast, guided modes are per definition absolutely confined to the stack, as they obey total internal reflection. Therefore, a net power flow arises from the guided mode into the radiative mode.

At this point, a general remark regarding the diffraction coefficient $\Gamma_{\mathrm{m}\to\mathrm{air}}$ and the extraction efficiency $\eta_{\mathrm{extr,m}}$ of the same guided mode should be made. The diffraction coefficient itself does not determine the extraction efficiency solely as also the absorption coefficient α_{m} has to be taken into account according to (2.8). For instance in the case of no absorption, 100% extraction efficiency is obtained regardless of the actual diffraction coefficient as long as $\Gamma_{\mathrm{m}\to\mathrm{air}}>0$. Only in the case of heavy absorption a change in diffraction coefficient causes the same amount of change in extraction efficiency[5]. In general, the extraction efficiency of a single guided mode reads

$$\eta_{\mathrm{extr,m}} = \frac{1}{2\pi}\int_0^{2\pi} \frac{1}{1+\alpha_{\mathrm{m}}/\Gamma_{\mathrm{m}}(\varphi)}\,d\varphi \tag{4.41}$$

Due to the coupling integral the diffraction coefficient varies depending on the in-plane propagation angle φ and may sometimes be even zero if diffraction from this particular propagation direction to ambient is not possible. Therefore, the extraction efficiency has to be calculated for every in-plane propagation direction of the guided mode and averaged afterwards. However, all these issues conceal the view on the pure diffraction properties of the PhC and hence, we will investigate PhC LEDs based upon the diffraction coefficient and discuss the consequences for the extraction efficiency separately. Additionally, calculating the latter within the model would cause significantly longer computation runs as the in-plane directions have to be discretised appropriately.

4.3 FDTD Method

The finite-difference time-domain method (FDTD) was first presented in [88] and probably has become one of the most popular algorithms in electromagnetics by now. The solution of Maxwell's equations (3.1) is accomplished by approximating the partial differential equations

[5] This is equivalent to the discussion regarding the Purcell factor as shown in Fig. 2.4. The radiative (non-radiative) rate is analogous to the diffraction (absorption) coefficient and the Purcell factor accounts for variations of the radiative rate.

by finite differences, both in time and in space. The time derivatives of the coupled Maxwell's curl equations – the latter two equations in (3.1) – are used in order to obtain an evolution of the fields in time. The electric field distribution for the next time step $t+\Delta t$ is derived from its current distribution at time t and from the spatial derivation of the magnetic field distribution at an intermediate point in time $t+\Delta t/2$. The latter has been calculated from the magnetic field distribution at time $t-\Delta t/2$ and a spatial derivation of the electric field distribution at time t. Hence, by alternately calculating the new electric and magnetic field distributions the fields evolve. Moreover, as both fields are used the solutions are more robust than using only one of them [41]. The unique spatial discretisation scheme via so-called Yee cells allows to approximate both the space and the time derivatives by central-difference finite-differences that are second-order accurate. In general, the strength of this approach relies on the fact that almost arbitrary structures can be calculated as long as the spatial grid is dense enough and the computational domain can be stored within the available computer memory. Additionally, as the method is time domain based, one simulation run yields the response of the system within a broad frequency range through a frequency analysis of the temporal field evolution, see for instance section 4.3.5.

In the upcoming section the simulation setup is described. Also the determination of the extraction efficiency and the Purcell factor is briefly discussed along with requirements on the computational domain in order to obtain reliable far field patterns. Afterwards the procedure for calculating dispersion relations with FDTD is summarized. In the last section the model for the metallic mirror is presented that has been used in FDTD in order to obtain the correct material dispersion.

We worked with the commercial software tool FDTD Solutions 5.2 from Lumerical [89] on a Linux 64bit multiprocessor machine with 16 cores (four AMD Opteron 8354 Quad Core 2.2GHz 2MB) and 128GB RAM.

4.3.1 Simulation Setup

A few things should be kept in mind that have to be met by the simulation setup in order to get the correct physics. First of all, as the diffraction process differs with respect to the in-plane directions, see e.g. Fig. 3.8b, the three-dimensional problem cannot be reduced to two-dimensions by just calculating a vertical slice through the PhC LED. Secondly, dipole sources are best suited for excitation as the electron-hole-recombination can classically be represented by a dipole, see 4.1.1. Furthermore, a large number of them should be randomly distributed at the position of the active region as all possible orientations of the dipoles with respect to the surface structure should be considered, see Fig. 4.5a. However, as FDTD intrinsically is a coherent simulation method the use of several dipoles within one simulation run results in an unphysical interference pattern representing the source. This interference pattern significantly influences the simulation results, especially the far field pattern. For the same reason, it is not convenient to use periodic boundary conditions, as shown in Fig. 4.5b, even though the periodicity of the PhC tempts to apply them. Due to the periodic continuation of the computational domain every embedded dipole is also replicated and interferes with its counterparts.

Therefore, we will use a single dipole source within a computational domain enclosed by absorbing boundary conditions (perfectly matched layers; PMLs), as depicted in Fig. 4.5c. We have proven by test simulations that different dipole positions and orientations have only negligible impact on the results if the dipole is rather far away from the surface structure (distance $>1\,\mu m$). For LED structures with a smaller distance different dipole positions are taken into account that are shown in Fig. 4.5d. In general, the extraction efficiency and the Purcell factor are less dependent on the dipole position than the far field pattern, especially for angles close to surface normal. In order to reduce the impact of the finite sized area on the

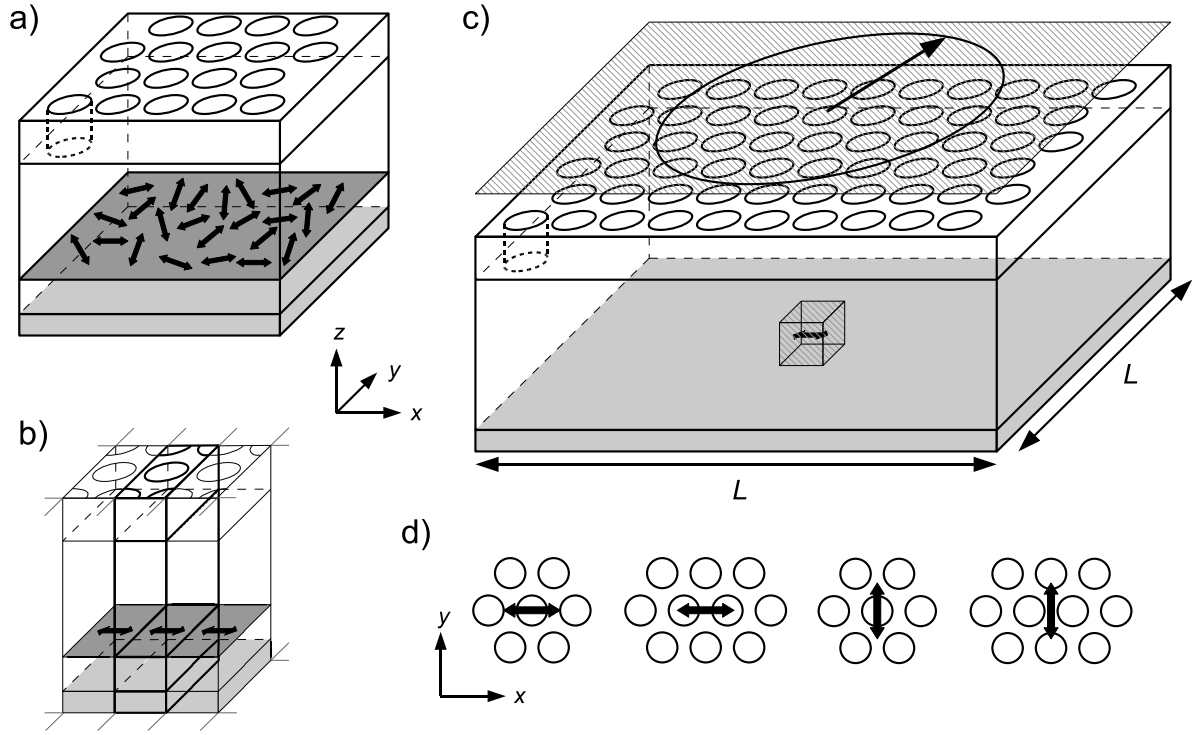

Fig. 4.5: Possible FDTD simulation setups; the grey area indicates the mirror and the dark grey area the active layer. (a) Randomly positioned and oriented dipoles define the active layer. (b) Periodic boundary conditions continue the structure, but also any dipole within the simulation volume. Thus a) and b) suffer from an unphysical interference pattern generated by the coherent dipoles and their relative position to each other. (c) Simulation setup we used during this work to calculate the extraction efficiency, Purcell factor and far field radiation patterns of surface textured LEDs. The shaded areas indicate planes used for calculating the power flux emitted by the source (cube around the dipole) and the extracted power flow (plane above the LED); the latter is calculated by integrating over disks with varying radius as depicted. L denotes the lateral dimension of the simulation setup. (d) Different dipole positions and orientations with respect to the hexagonal lattice taken into account in the simulations when the distance between the PhC and the dipole is small (distance < 1 µm).

simulation results large simulation volumes are used. Here, the computational time sets an upper limit on the lateral area, as it exhibits quadratic growth depending on the lateral area. Therefore, the lateral dimensions were set to 60µm by 60µm. Since the dipole is placed in the middle of the simulation volume light interacts 30µm with the PhC before being absorbed at the PMLs. Typically, computational times of 9h up to 40h are necessary before reaching the shutoff criterion (electromagnetic energy has decreased to 10^{-5} of its peak value) depending on the extraction capability and the absorption of the structure.

4.3.2 Extraction Efficiency

Even though relatively large computational domains are used, entire LED structures cannot be modelled. Small LEDs still have lateral dimensions of 250µm by 250µm (approximately 6.5d of computing in the best case). Additionally, it became evident that complete light extraction cannot be achieved within 30µm propagation distance for typical LED structures (e.g. LED as shown in Fig. 4.5c with thickness of 3µm and 300nm deeply etched PhC). Therefore, a scheme was set up for extrapolating the extraction efficiency of entire LEDs. The basic idea is to obtain extraction efficiencies from several simulation runs with the same LED structure but different lateral dimensions. In each case, the extraction efficiency is calculated from the power flux extracted from the structure with respect to the overall emitted power from the source, see Fig. 4.5c,

$$\eta_{\mathrm{extr}} = \frac{P^{+}_{\mathrm{z,out}}}{P^{+}_{\mathrm{x,in}} + P^{-}_{\mathrm{x,in}} + P^{+}_{\mathrm{y,in}} + P^{-}_{\mathrm{y,in}} + P^{+}_{\mathrm{z,in}} + P^{-}_{\mathrm{z,in}}}, \tag{4.42}$$

with $P_{\mathrm{z,out}}$ the power flow integrated over a plane above the LED structure and $P_{\mathrm{x,y,z,in}}$ the integrated power flux through the planes normal to x, y or z enclosing the source. The + and – sign indicate power flow parallel or anti-parallel to the corresponding axis. Hence, we obtain a series of extraction efficiencies $\eta_{\mathrm{extr,j}}$ for every lateral dimension L_{j}. The extraction efficiency for arbitrarily large LEDs is extrapolated from these values by fitting

$$\eta_{\mathrm{extr}}(x) = \eta_0 + \frac{\eta}{\eta+\alpha}\left(1 - e^{-(\eta+\alpha)x}\right). \tag{4.43}$$

As the light propagates inside the LED it undergoes two phenomena. Firstly, it is extracted due to the PhC. This is taken into account by the extraction coefficient η. Secondly, it suffers from absorption (denoted by the absorption coefficient α). The term in brackets describes the fraction of light either absorbed or extracted after the propagation distance x. The ratio of coefficients $\eta/(\eta+\alpha)$ defines the amount of extracted light. Hence, the extraction efficiency as a function of the propagation distance can be calculated. The amount of light extracted from the LED without the help of the PhC, i.e. light generated within the extraction disk, is taken into account by the offset η_0.

Unfortunately, running several simulations is extremely time consuming. But it is also possible to obtain the dependency of the extracted power flow on the lateral dimension from a single simulation. To mimic increasing lateral simulation dimensions L_{j} the extracted power flow is not integrated over the entire plane above the LED but over a disk with increasing radius. Hence, almost any number of lateral lengths can be obtained up to the maximum of 30µm. We calculated the extracted flux and hence the extraction efficiency in steps of 1µm. However, regarding the extrapolation of this data it has to be mentioned that both the extraction and the absorption coefficient as introduced in (4.43) are average values over a large number of guided modes, each with individual coefficients. Hence, modes with e.g. high extraction coefficients will contribute significantly to the extraction efficiency at short propagation distances whereas they negligibly impact the values at large x as they are almost completely extracted. At large distances rather slow processes determine the extraction efficiency. To illustrate the impact of fast processes on the extrapolation, Fig. 4.6 exemplarily shows results for the extraction efficiency (grey symbols) along with three different fits. Firstly, as can be seen, the calculated extraction efficiencies do not saturate within 30µm and total light extraction from the PhC LED is not achieved. But this lateral dimension is large enough for a reasonable extrapolation of the data with the first 9 points neglected (solid black line). For the dashed black line only these 9 points are taken into account. This extrapolation yields significantly lower extraction efficiencies compared to the prior case as the contributing extraction process stem from high extraction coefficients. Hence, these points should not be taken into account for extrapolating the extraction efficiency. In contrast, neglecting more than 9 points, e.g. the first 14 points (dotted black line), has only negligible impact on the extrapolated extraction efficiency. Thus, the extrapolated values for the extraction efficiency given in this work are obtained by neglecting the first 9µm. The dash-dotted line indicates the extraction efficiency of the unstructured reference LED obtained from FDTD simulations. A comparison of this value with the corresponding one from the transfer-matrix method of section 4.1 reveals a deviation of the FDTD simulations of less than 10%.

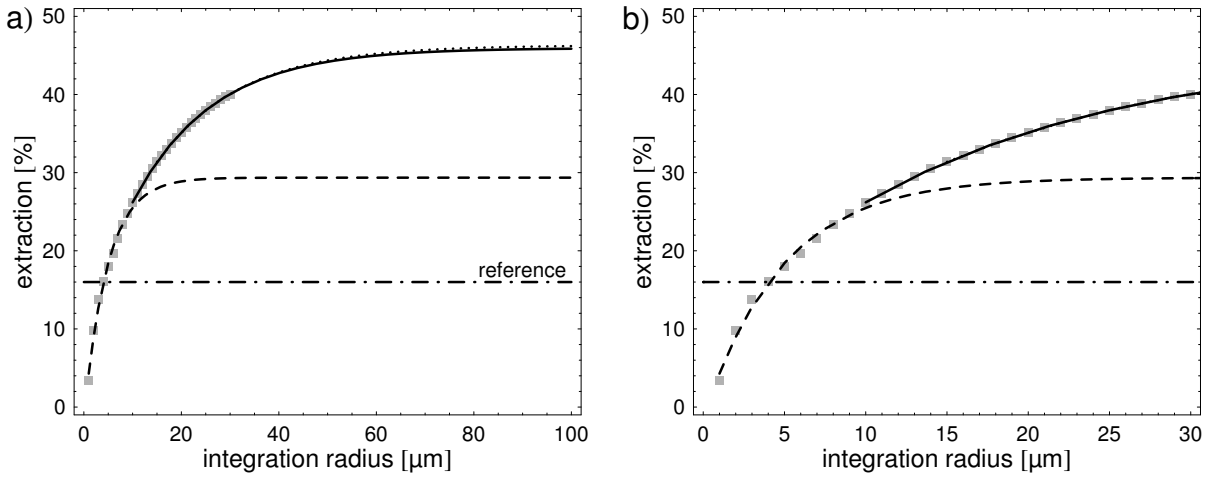

Fig. 4.6: Example for the extrapolation of the extraction efficiency; grey symbols represent the extraction efficiency calculated from the simulation by increasing the integration radius; the black solid (dotted) line is a fit to these values according to (4.43) while neglecting the first 9 (14) points. The dashed black line is obtained from a fit that only takes into account the first 9 points. (b) is a close-up to the data shown in (a).

The data are obtained from a green emitting LED as sketched in Fig. 4.5c with n_{SC}=2.4, n_{amb}=1, a silver bottom mirror (see section 4.3.6), a 300nm deeply etched hexagonal PhC with pitch a=600nm and filling fraction F=0.5. The distance between the source and the mirror is 160nm, the peak wavelength is 520nm and a FWHM of 30nm of the Gaussian emission spectrum is taken into account by calculating the extraction efficiency at 71 different wavelengths in the interval [470nm;570nm].

4.3.3 Purcell Factor

The calculation of the Purcell factor is analogous to the derivation given in [90]. From its definition (2.4) the Purcell factor is the ratio between the radiative decay rate Λ_{rad} in the system under study with respect to the decay rate $\Lambda_{rad,0}$ in bulk material with the same refractive index as the active region. It can now be shown [90] that the ratio of the quantum mechanically given decay rates is equivalent to the ratio of the corresponding power fluxes from dipole sources

$$F_P = \frac{\Lambda_{rad}}{\Lambda_{rad,0}} = \frac{P_{tot}}{P_{tot,0}} \tag{4.44}$$

with P_{tot} the total power flux emitted from a dipole in the system under study

$$P_{tot} = P^+_{x,in} + P^-_{x,in} + P^+_{y,in} + P^-_{y,in} + P^+_{z,in} + P^-_{z,in}\,, \tag{4.45}$$

and $P_{tot,0}$ the total emitted power flux from a dipole located in a homogeneous optical environment. For the calculation of the Purcell factor the function *transmission()* of FDTD Solutions was used. In general, the calculation of the Purcell factor puts least demand on the computational setup.

4.3.4 Far Field Radiation Pattern

A major objective of this work is to study the emission patterns of PhC LEDs in order to clarify their applicability for étendue limited systems. Therefore, the lateral dimensions have to be large enough to ensure negligible impact of the finite sized simulation volume on the

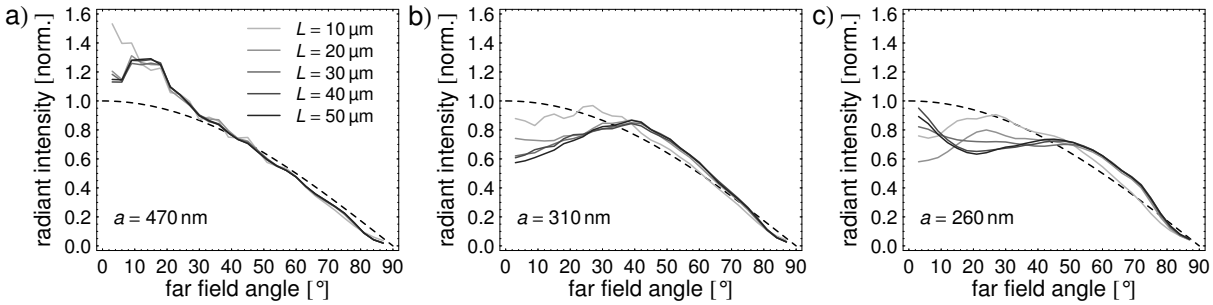

Fig. 4.7: Azimuthally averaged far field patterns for a LED similar to the one used in Fig. 4.6 except the overall thickness is ~6µm and the pitch is a=470nm (a), a=310nm (b), and a=260nm (c). The darker the corresponding solid line the larger the simulation dimensions, ranging from L=10µm up to L=50µm. The dashed line represents a Lambertian far field pattern with I(θ)=cosθ.

radiation pattern. Fig. 4.7 shows azimuthally averaged far field patterns for the LED already used in Fig. 4.6 except for the overall thickness being ~6µm and the pitch being 260nm, 310nm and 470nm, respectively. Depending on the simulation dimensions different far field shapes are obtained for the same LED structure. For a pitch of a=470nm the earliest convergence is achieved for a length of L=20µm. For smaller pitches of a=310nm and a=260nm lengths greater than $L\geq$30µm and $L\geq$40µm are necessary, respectively.

We used the *farfield3d()* command of FDTD Solutions for the calculation of the far field patterns from the electric and magnetic field distribution within the plane that the extracted power flow is calculated from, see Fig. 4.5c. Additionally, a Gaussian averaging according to the emission spectrum as described in section 4.3.2 has been carried out to obtain the results as presented in Fig. 4.7.

4.3.5 Calculating Dispersion Relations

Apart from power fluxes and far field radiation patterns FDTD is also capable of calculating the dispersion relation of arbitrary periodic structures. For these calculations so called Bloch boundary conditions and "white" dipole sources are used.

According to Bloch's theorem (3.5) the different eigensolutions of the master equation (3.3) or (3.4) can be distinguished by their k-vector and their frequency. For every value of **k** discrete values of $\omega_n(\mathbf{k})$ exist corresponding to the different bands of the dispersion relation.

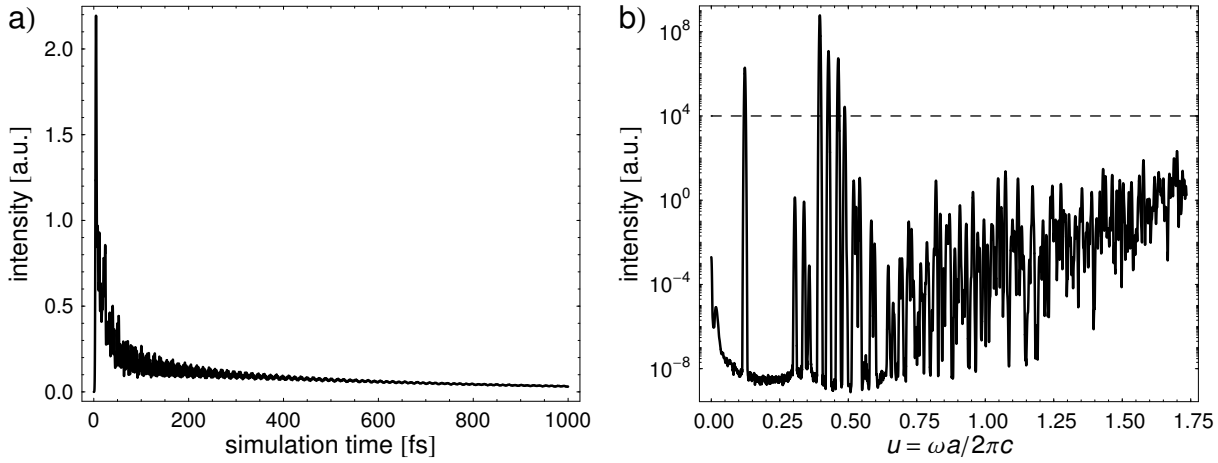

Fig. 4.8: (a) Example of a temporal intensity evolution for a single value of the in-plane k-vector. (b) The corresponding frequency analysis. Only the values above a certain threshold (dashed line) are collected for the dispersion relation.

In order to obtain every frequency eigenvalue for a given in-plane propagation direction several dipole sources each with a very sharp emission pulse in time are located within the computational domain. Hence, a broad frequency range is excited. Even though coherent, more than one dipole source has to be used as every possible mode profile has to be launched. The Bloch boundaries select the k-vector of interest as they only allow field distributions of the corresponding Bloch modes. According to the periodicity of the Bloch modes, a simulation volume enclosing one unit cell is sufficient, e.g. as depicted in Fig. 4.5b. The discrete frequency values $\omega_n(\mathbf{k})$ are detected by a frequency analysis of the temporal field evolution as highlighted in Fig. 4.8; the peaks in this spectrum above a certain threshold value are collected. By running several simulations with different Bloch boundary settings, the k-space is sampled and the dispersion relations as shown in Fig. 3.7 are obtained.

4.3.6 Model for Metallic Mirrors

The correct representation of dispersive materials within multiple frequency FDTD simulations requires to describe the refractive index dispersion by analytical functions. In this work, dispersion is only taken into account for the silver mirror of the green InGaN LED. The parameters of the other materials are assumed constant, i.e. $n_{GaN}=2.4$. The refractive index values of silver are taken from [91] and are shown in Fig. 4.9. The analytical function is obtained from a fit to these values based on a combined Plasma-Lorentz model [92]

$$\varepsilon(\omega) = \varepsilon_0 - \underbrace{\frac{\omega_P^2}{\omega(\omega + i\nu_c)}}_{\text{Plasma}} + \underbrace{\frac{\varepsilon_{Lo}\omega_0^2}{\omega_0^2 - 2i\delta_0 - \omega^2}}_{\text{Lorentz}}, \tag{4.46}$$

with $\varepsilon_0=3.75$, $\omega_P=1.39\ 10^{16}$, $\nu_c=3.11\ 10^{13}$, $\varepsilon_{Lo}=1.17$, $\omega_0=1.71\ 10^{15}$, and $\delta_0=3.52\ 10^{16}$.

However, in most LEDs the reflectivity of the GaN-Ag interface obtained from these values is not as good as shown in Fig. 4.10 (black line) since thin, heavily absorbing layers are used in-between to ensure better adhesion of GaN and Ag. The accurate description of these thin layers in FDTD would require a huge computational effort. To circumvent this problem we instead increased the collision frequency ν_c of the Plasma part by a factor of 10 to decrease the reflectivity of this combined mirror down to reasonable values.

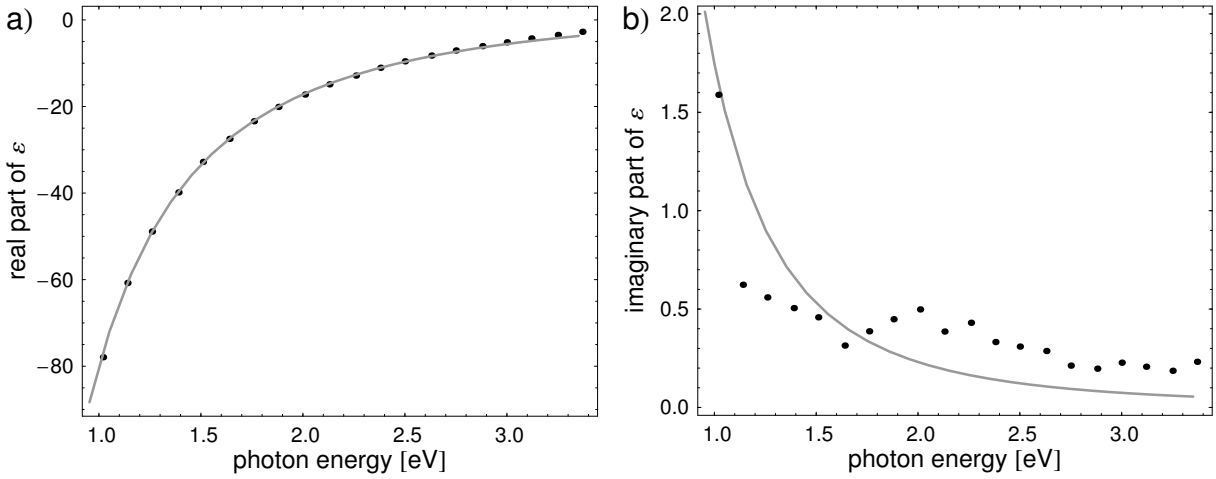

Fig. 4.9: Experimental dispersion of silver from [91] (black dots) and a fit according to (4.46) (grey solid line). (a) Real part of the dielectric function; (b) imaginary part.

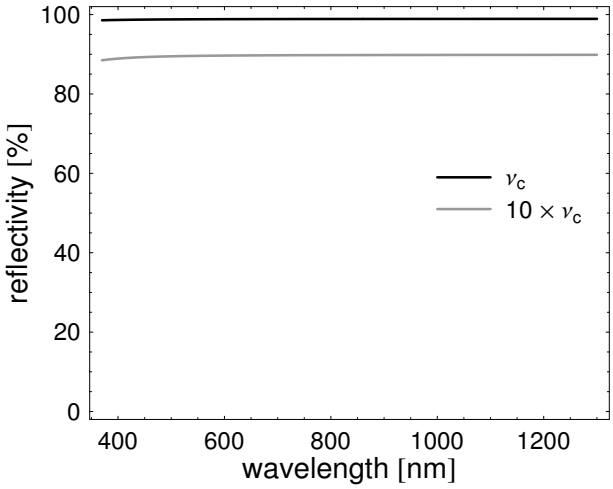

Fig. 4.10: Reflectivity of GaN-Ag interface under normal incidence for material parameters as obtained from the fit Fig. 4.9 (black line) and for a 10 times higher collision frequency (grey line).

5 Weak PhC LEDs

For the incorporation of PhCs in LEDs several possible implementations can be thought of [69][93] with the two basic configurations shown in Fig. 5.1. In the first instance, Fig. 5.1a, the whole chip area is used for light generation as well as light extraction. Hence, the radiance is fairly homogenous across the chip and every part of the chip contributes to light generation. However, in this case etching through the active layer has to be avoided as an amount of light generation area equal to the area fraction of holes is lost. Consequently, at a given driving current the current density at the remaining active regions is increased and less radiant flux is emitted from the same chip area as the droop causes a decreased efficiency. Additionally, due to surface states at the walls of the holes the electron-hole pairs tend to recombine non-radiatively at the surfaces [14]. Therefore, the internal quantum efficiency is further reduced. However, it has been shown recently that an appropriate annealing step could heal the etch-induced damage [94] and that the surface recombination process is less pronounced in the case of green emission [95]. The second configuration is realized by separating light generation and light extraction, see Fig. 5.1b. The patterned area should be larger than the propagation distance of the light before it is extracted and/or absorbed. Here, etching through the active area implies no penalties on the efficiency. But the radiance decreases exponentially with increasing distance from the light generation area. Furthermore, the active area is reduced as compared to the first case. As higher current densities have to be used, these devices are less efficient. Nevertheless, since the directly emitted light is spatially separated from the light diffracted from guided modes, these devices give a clear insight into the operation principle of PhCs [21][30].

In summary, for high efficiency devices a setup as shown in Fig. 5.1a is preferred. Hence, we will investigate this case. For weakly coupled PhCs, i.e. if the etch depth of the PhC is small compared to the overall thickness of the LED, it is convenient to separate the 3D problem of a PhC LED into a 2D+1D problem. According to the diffraction model the two-dimensional part – represented by the Fourier transform $|\Delta\varepsilon_{\mathbf{G}}|^2$ of the lattice – includes the lattice pitch, the lattice type itself and the filling fraction. The one-dimensional part consists

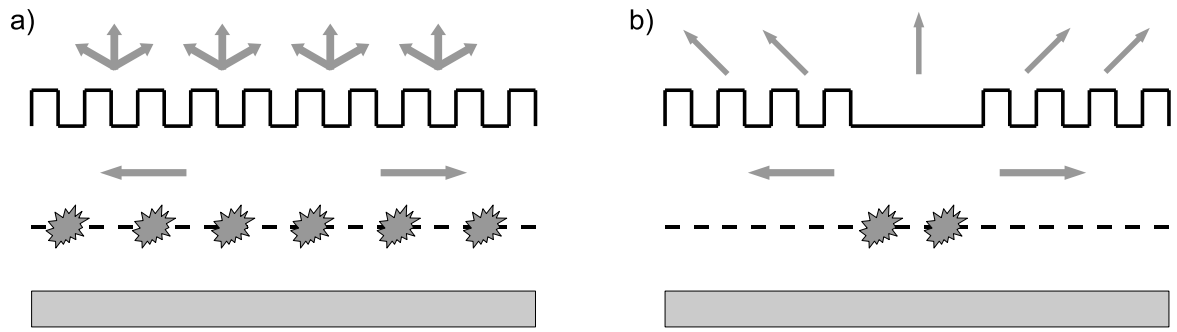

Fig. 5.1: Two possible PhC LED configurations. In (a) light generation and light extraction are obtained from the same area, whereas in (b) both regions are laterally separated. In order to achieve high efficiency devices with a homogenous radiant emittance, case (a) will be used in this work.

of the design of the vertical layer stack and the resulting mode distribution. Here, the amount of spontaneous emission B_m into each mode and the coupling integral κ_{mk} between modes have to be taken into account. The two parts are coupled to each other by the filling fraction of the PhC that influences the Fourier transform of the PhC on the one hand and determines the average refractive index of the PhC layer on the other hand.

In the upcoming sections the properties of the lattice and the vertical layer stack are discussed. Along with geometrical considerations, the diffraction model is utilized to investigate the relevant mechanisms. Our conclusions will be confirmed by calculations with FDTD as a reference including the whole physics. As a sample structure we use a green emitting InGaN LED as shown in Fig. 5.2 because it exhibits a simple structure while still being relevant for applications. The refractive index profile within real InGaN LEDs varies negligibly so that the whole layer stack is assumed to have the same refractive index, $n_{GaN}=2.4$. Even though the active region of these LEDs can consist of several quantum wells we only take into account a single well in order to reduce the computational effort for the FDTD simulations. Several quantum wells in varying distances from the mirror would require several simulation runs each with a different vertical position of the dipole. Consequently, in order to ensure good comparability between FDTD and the diffraction model, the active region in the latter is represented by a single 1nm thin layer with the same distance from the mirror as the FDTD dipole. The mirror has the refractive index function as presented in section 4.3.6 and air is taken as the ambient medium, $k_{amb}=k_0$.

Unless stated otherwise during the upcoming chapters results are obtained for the following values of the LED structure. The emission spectrum is assumed to be Gaussian with a peak wavelength of $\lambda_{peak}=520$nm and a FWHM of 30nm. The FDTD calculations include 71 supporting wavelength points within the interval [470nm;570nm]. For the diffraction model calculations have been carried out in steps of 2nm ranging from 480nm to 560nm. The active layer is embedded into a 3µm thick GaN layer, where the PhC is 300nm deeply etched into. The distance between the active layer and the mirror is 160nm. The PhC itself consists of a hexagonal lattice with filling fraction $F=0.5$ and pitch $a=600$nm corresponding to a primitive reciprocal lattice vector $G_0=k_0$. The resulting PhC LED will be proven to yield high extraction efficiencies while the internal quantum efficiency and the electrical efficiency should remain unchanged compared to standard thin-film LEDs.

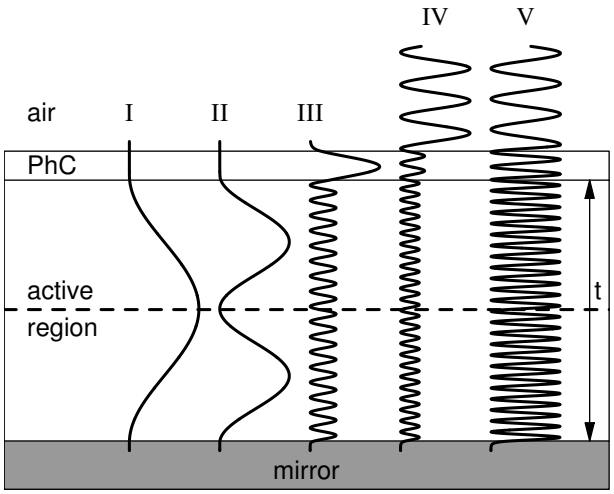

Fig. 5.2: Schematic of the sample LED used throughout this chapter. The thickness of the unetched GaN core is labelled t. Different mode profiles are sketched (I-III guided modes, IV and V radiative modes). The PhC layer's dielectric constant is calculated according to the filling fraction, $\varepsilon_{PhC}=F+(1-F)\varepsilon_{GaN}$.

5.1 Lateral Part: Reciprocal Lattice Vector, Lattice Type and Filling Fraction

In this section, first we focus on the impact of the pitch or equivalently the reciprocal lattice vector on the diffraction process. Afterwards, different lattice types are compared and the filling fraction is optimised. In order to derive the underlying principles the diffraction process of single guided modes is studied and the impact of additional modes is neglected. This will be discussed in section 5.2 as the vertical layer stack plays an important role here.

5.1.1 Reciprocal Lattice Vector

The impact of the reciprocal lattice vector **G** on the diffraction process is best seen by investigating the diffraction of a single guided mode according to Bragg's law as shown in Fig. 5.3 by the solid black circle.

In general, the diffracted k-vectors can be divided into three classes according to the light lines in the dispersion relation Fig. 3.2. The first one covers the segment of the solid black circle outside the ring of guided modes, $\beta_k > k_{SC}$. These states are neglected as they correspond to evanescent propagation within the LED. The second class contains diffraction from a guided mode into another guided mode, $k_0 < \beta_k < k_{SC}$. Here, owing to the finite number of guided modes only a finite number of diffraction processes redistributes the energy stored within the guided modes. On the one hand, light has an additional chance to escape from the structure after redistribution. On the other hand, it suffers from absorption losses. In contrast, an infinite number of diffraction processes is possible for case three: the guided mode is diffracted into the extraction cone, $\beta_k < k_0$, and the extraction efficiency improves. This process is possible if $\beta_m - k_0 < G < \beta_m + k_0$ is fulfilled.

In order to diffract as much different in-plane propagation directions $\boldsymbol{\beta}_m/\beta_m$ as possible into the extraction cone the reciprocal lattice vector has to be adjusted. Owing to the infinite number of radiative modes the possible diffraction processes to air scale with the arc length within the extraction disk $L_{arc} = 2\beta_m\varphi$ with the in-plane angle determined by the law of cosines, see Fig. 5.3,

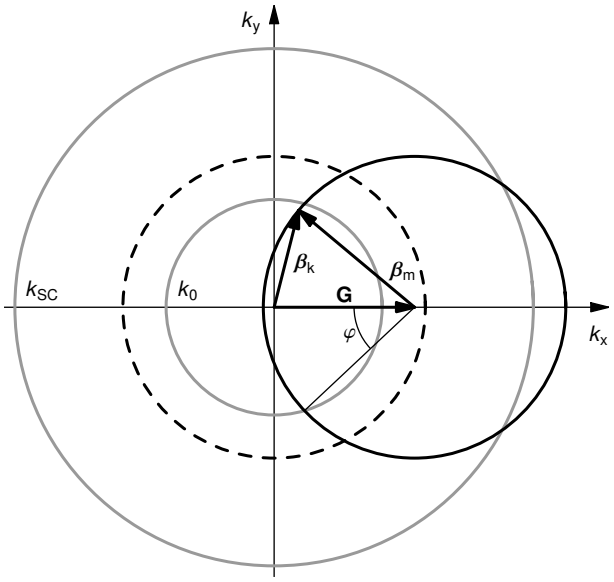

Fig. 5.3: Geometrical construction in order to determine every possible diffracted k-vector according to Bragg's law. The inner grey circle depicts the extraction cone, the outer one the maximum k-vector available within the LED. The in-plane angle 2φ determines the fraction of in-plane propagation directions that are diffracted into air according to the diffraction process $\boldsymbol{\beta}_k = \boldsymbol{\beta}_m + \boldsymbol{G}$

$$\cos\varphi = \frac{G^2 + \beta_{\mathrm{m}}^2 - k_0^2}{2\,G\,\beta_{\mathrm{m}}}. \tag{5.1}$$

For simplicity we first assume constant coupling of the guided mode to each radiative mode, κ_{mk}=const., and consider only a single reciprocal lattice vector. Fig. 5.4 shows the arc lengths for different guided modes according to (5.1). Evidently, each guided mode has a separate optimum reciprocal lattice vector for maximum extraction and is diffracted into air if $|G-\beta_{\mathrm{m}}|<k_0$. Depending on the curvature of the mode circle the optimal reciprocal lattice vector length G has to be shorter than the in-plane k-vector length β_{m}. In the case of the guided mode with $\beta_{\mathrm{m}}=1.1k_0$ an almost 60% shorter reciprocal lattice vector compared to the guided modes' eigenvalue yields best extraction. Furthermore, due to this curvature more in-plane propagation directions are extracted from guided modes with small β_{m} compared to those with larger β_{m}. Hence, guided modes with small β_{m} are extracted more efficiently than guided modes with large β_{m}.

If we now expand our considerations towards the whole Fourier spectrum of the PhC as shown in Fig. 5.5b, every possible **G** has to be considered. According to the diffraction model each diffraction process has to be weighted by the corresponding Fourier intensity $|\Delta\varepsilon_{\mathbf{G}}|^2$, i.e. the photonic strength of the lattice [23][29]. Thus, the diffraction coefficient for a guided mode can be approximated by the sum over every reciprocal lattice vector resulting in $\beta_{\mathrm{k}}<k_0$ according to

$$\Gamma_{\mathrm{m}\to\mathrm{air}}^{\mathrm{PhStr}} = \sum_{\substack{\mathbf{G} \\ |G-\beta_{\mathrm{m}}|<k_0}} L_{\mathrm{arc}}(G,\beta_{\mathrm{m}})\left|\Delta\tilde{\varepsilon}_{\mathbf{G}}\right|^2. \tag{5.2}$$

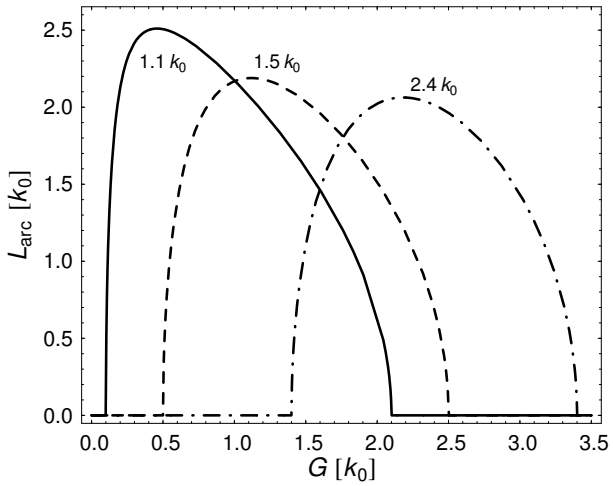

Fig. 5.4: Length of the circle segment of the diffracted guided mode within the extraction cone for $\beta_{\mathrm{m}}=1.1k_0$ (solid line), $\beta_{\mathrm{m}}=1.5k_0$ (dashed line), and $\beta_{\mathrm{m}}=2.4k_0$ (dash-dotted line). Guided modes with short in-plane k-vector are diffracted more efficiently into the extraction cone due to the higher curvature of the circle. Furthermore, the optimum reciprocal lattice vector has to be shorter than the guided mode k-vector.

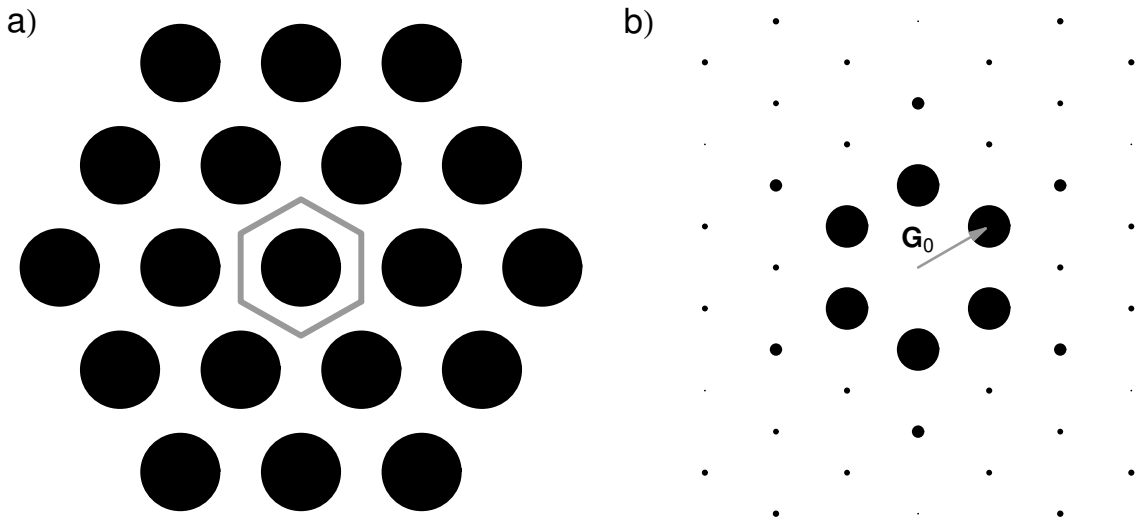

Fig. 5.5: (a) Hexagonal PhC lattice with F=0.4. (b) Corresponding Fourier transform; the disks' radii account for the squared modulus of the Fourier amplitude $|\Delta\varepsilon_{\mathbf{G}}|^2$; for better visibility the square root of the Fourier peaks is taken.

In Fig. 5.6 this diffraction coefficient is shown as a function of the primitive reciprocal lattice vector length G_0 for a hexagonal PhC with F=0.4. Compared to the pure geometrical consideration in Fig. 5.4 now guided modes with large in-plane k-vector length are also extracted by reciprocal lattice vectors with $G_0<\beta_m-k_0$ owing to high order diffraction processes, i.e. diffraction by $G=3^{1/2}G_0$, $G=2G_0$ etc. in the case of a hexagonal lattice. The diffraction coefficient is rather low due to the low corresponding Fourier intensities $|\Delta\varepsilon_{\mathbf{G}}|^2$. In contrast, no diffraction is possible for $G_0>\beta_m+k_0$ as the hexagonal lattice does not support any reciprocal lattice vectors with $G<G_0$. The guided mode with $\beta_m=1.1k_0$ is diffracted even more efficient compared to the other modes due to the contribution of high order diffraction processes. These are favoured by the rather short optimum $G_0=0.3k_0$ that is roughly 70% shorter than the in-plane k-vector. Simultaneously, this optimum G_0 ensures that the arc length related to diffraction by $G=G_0$ with the highest Fourier intensity still is significant as can be seen in Fig. 5.4.

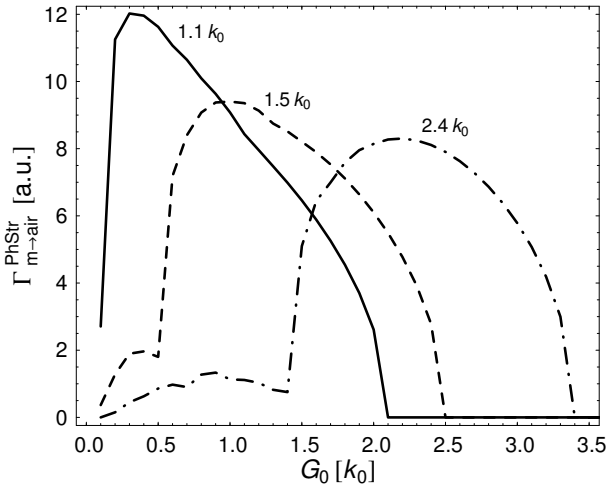

Fig. 5.6: Calculations of the diffraction coefficient considering the whole Fourier spectrum of the PhC with F=0.4 according to (5.2), i.e. κ_{mk}=const., for guided modes with $\beta_m=1.1k_0$ (solid line), $\beta_m=1.5k_0$ (dashed line), and $\beta_m=2.4k_0$ (dash-dotted line). Guided modes with short β_m are diffracted even more efficient compared to Fig. 5.4 as high order diffraction processes also result in $\beta_k<k_0$.

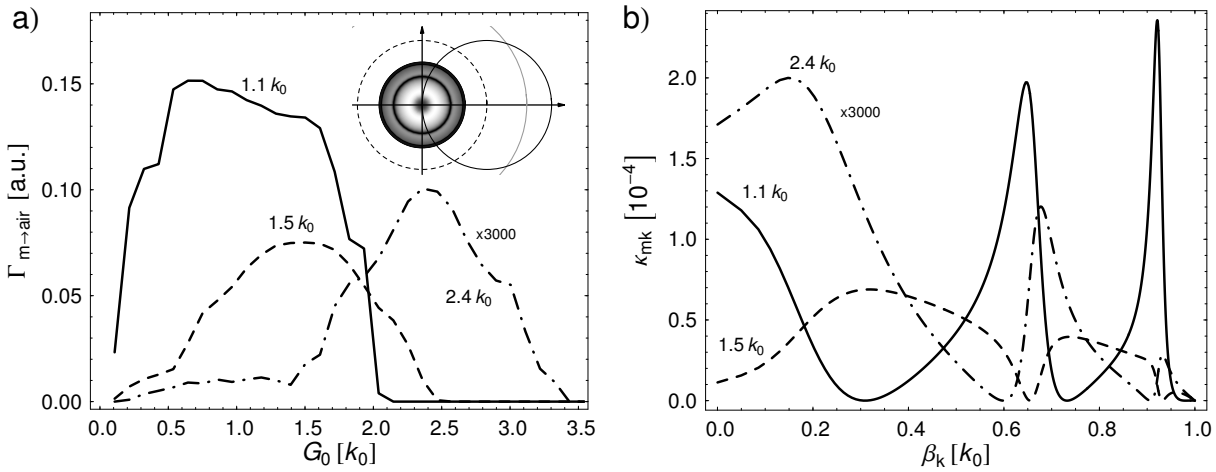

Fig. 5.7: (a) Calculations from the diffraction model according to (4.37) for the LED as given in the introduction to chapter 5 but with $F=0.4$. This structure supports among others three TE-polarized modes at $\lambda=558$nm with $\beta_m\approx 1.1k_0$ (solid line), $\beta_m\approx 1.49k_0$ (dashed line), and $\beta_m\approx 2.4k_0$ (dash-dotted line). The inset sketches the diffraction process of $\beta_m\approx 1.49k_0$ by $G_0=\beta_m$. The different grey levels within the extraction disk indicate the varying coupling integral between the guided mode and the radiative modes. (b) The coupling integral κ_{mk} of the guided modes in (a) with each radiative mode. As the guided mode with $\beta_m\approx 2.4k_0$ has only tiny overlap with the PhC – mode I in Fig. 5.2 shows the corresponding mode profile – compared to the other modes its diffraction coefficient und coupling integral is multiplied by a factor of 3000. Due to the radial symmetry of the coupling integral the impact of the curvature of the guided modes' circles on the diffraction coefficient vanishes and $G_0\approx\beta_m$ is a reasonable choice in terms of high diffraction coefficient.

Before discussing results of the diffraction coefficient obtained from the diffraction model one should keep in mind that the guided mode's profile plays an important role for the diffraction coefficient according to the coupling strength, see (4.30). For instance, the guided mode III in Fig. 5.2 probably will be diffracted more efficiently than modes I and II due to its potentially larger coupling integral with radiative modes. These issues will be discussed in section 5.2; now, we investigate the impact of the coupling integral on the choice of G_0 for best diffraction of a single guided mode and will not compare $\Gamma_{m\to air}$ for different guided modes. From Fig. 5.7a it can be seen that the asymmetry of the diffraction coefficient around $G_0=\beta_m$ declines comüared to Fig. 5.6 when taking into account the coupling integral between the guided mode and the radiative modes. Owing to the radial symmetry of the coupling integral κ_{mk}, as depicted in the inset of Fig. 5.7a, the impact of the curvature and higher order diffraction processes on the diffraction coefficient decreases compared to Fig. 5.6 and primitive reciprocal lattice vector lengths of $G_0=\beta_m$ yield high diffraction rates. This effect is almost the same for each of the three modes under investigation regardless of the actual characteristics of the coupling integral that is shown in Fig. 5.7b.

In conclusion, for the efficient diffraction of a guided mode to air a PhC with primitive reciprocal lattice vector $G_0\approx\beta_m$ should be chosen. Higher order diffraction processes along with the curvature of the mode's circle cause higher diffraction rates to air for guided modes with short in-plane k-vector length β_m compared to highly guided modes with $\beta_m\approx 2.4k_0$.

5.1.2 Lattice Type: Omni-directionality

As the in-plane k-vector length of a guided mode fulfils $\beta_m>k_0$ only a fraction of the possible propagation directions of a guided mode can be extracted by a single reciprocal lattice vector while the remaining are not extracted [19]. Fig. 5.8a shows this fraction as a function of the in-plane k-vector β_m of the guided mode under the assumption $G=\beta_m$. The fraction drops from 33% for $\beta_m=k_0$ down to 13% for $\beta_m=2.4k_0$. Thus, in the latter case 87% of the guided mode's propagation directions are not diffracted to air by a single reciprocal lattice vector.

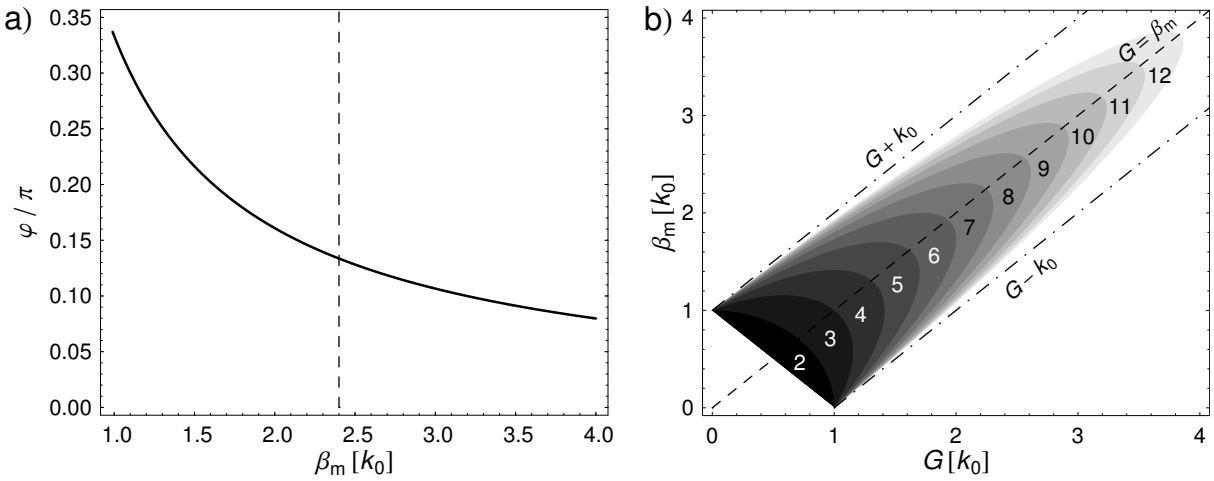

*Fig. 5.8: (a) Fraction of all in-plane propagation directions diffracted into the extraction cone in dependence of the in-plane k-vector β_m in the case $G=\beta_m$. The dotted vertical line indicates the maximum available in-plane k-vector for GaN, $\beta_m=2.4k_0$. (b) Range of guided modes diffracted omni-directionally as a function of the reciprocal lattice vector length and the number of reciprocal lattice vectors having this length (the fading black indicates increasing number of **G** from 2 to 12). The dashed line indicates $G=\beta_m$. The dash-dotted lines enclose the guided mode region that is diffracted into the extraction cone $|G-\beta_m|<k_0$.*

However, as can be seen in Fig. 5.5b a hexagonal lattice supports not only a single reciprocal lattice vector with a given length but several, e.g. six **G** with $G=G_0$. Each of these reciprocal lattice vectors acts on a different fraction of in-plane propagation directions of the guided mode. Consequently, all in-plane propagation directions can be diffracted to air if the number of reciprocal lattice vectors with the same length is high enough. In this case the lattice offers omni-directional diffraction. Fig. 5.8b shows the range of in-plane k-vectors that are omni-directionally diffracted into the extraction disk by a given reciprocal lattice vector length G in dependence of the number of reciprocal lattice vectors **G** with $|\mathbf{G}|=G$. We assumed these vectors to be evenly distributed on a circle with radius G. A finite number of reciprocal lattice vectors with the same length G hardly extracts all the guided modes with $|G-\beta_m|<k_0$ omni-directionally, as the shaded areas never cover the complete area between the dash-dotted lines.

For six reciprocal lattice vectors, e.g. the reciprocal lattice vectors of a hexagonal lattice with $G=G_0$, guided modes with in-plane k-vector lengths of $k_0<\beta_m<2k_0$ are extracted omni-directionally by $G=3^{1/2}k_0$. For guided modes with $\beta_m>2k_0$ a higher number of reciprocal lattice vectors with the same length has to be used. In the case of a hexagonal lattice, second order diffraction processes, i.e. $G=3^{1/2}G_0$ and $G=2G_0$, could be used as they have similar lengths and six reciprocal lattice vectors exist for each length. In the following we assume an average reciprocal lattice vector length of $G=(2+3^{1/2})/2G_0=1.87G_0$ for the second order diffraction processes of the hexagonal PhC. With these second order processes it is possible to fold all in-plane propagation directions above the light line for guided modes with eigenvalues as high as $\beta_m=3.85k_0$. However, the whole range of guided modes $k_0<\beta_m<3.85k_0$ is not diffracted completely, as the lower limit for omni-directional diffraction also increases. Hence, in the case of GaN twelve reciprocal lattice vectors extract every guided mode within the range $k_0<\beta_m<2.4k_0$ completely, only if their length is in the range $1.53k_0<G<1.93k_0$. If both first and second order processes are taken into account, every guided mode is folded above the light line if $G_0<3^{1/2}k_0$, since the first Brillouin zone fits completely into the extraction cone, see Fig. 3.4. In general however, the drawback of second order processes is their low Fourier intensity resulting in a poor diffraction coefficient compared to first order diffraction, see Fig. 5.6.

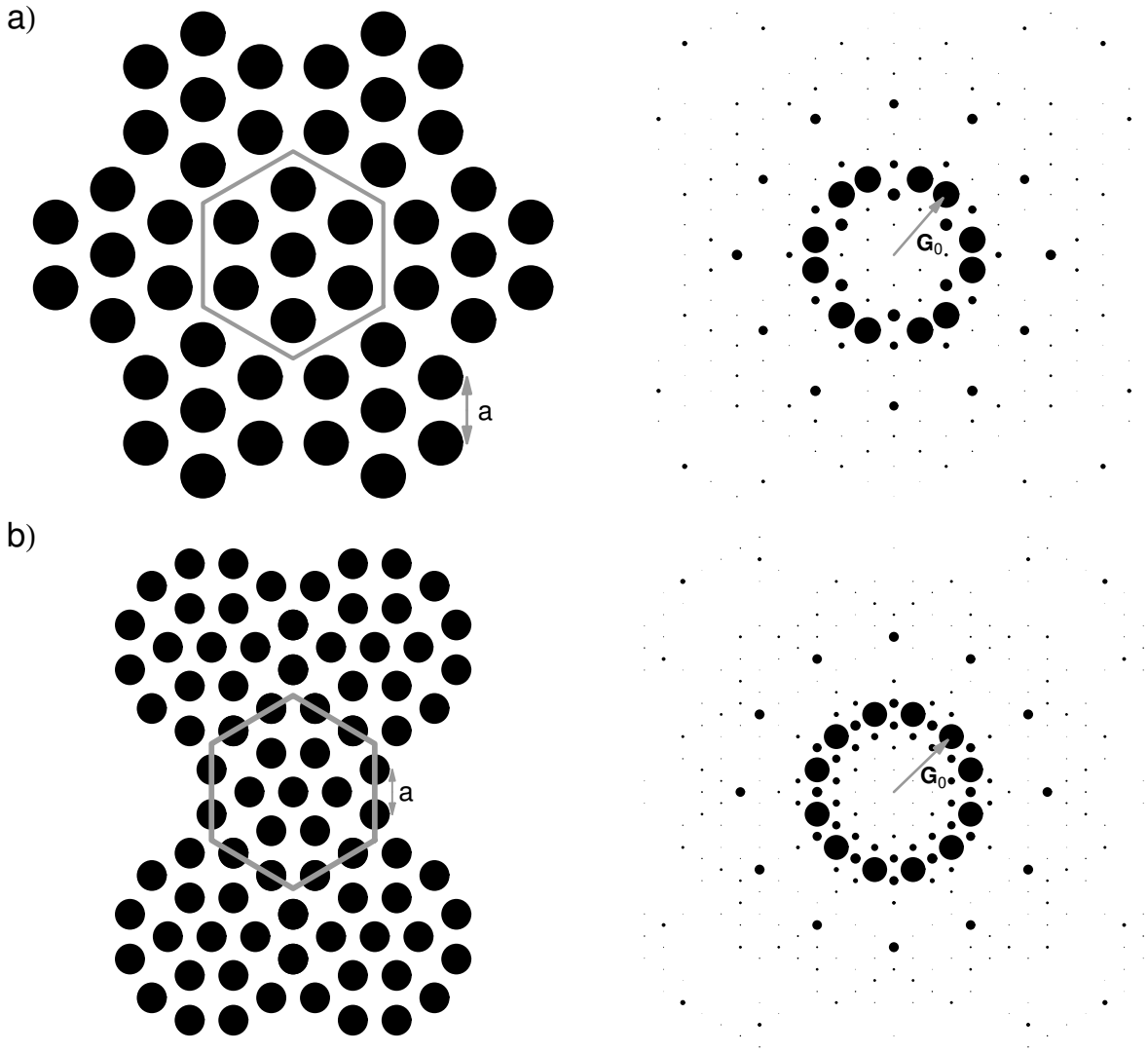

Fig. 5.9: Archimedean lattices with F=0.4: (a) hexagonal lattice with 7 holes per unit cell (grey hexagon); (b) hexagonal lattice with 13 holes per unit cell (grey hexagon). Left column shows the real lattices, right column the corresponding Fourier spectrum (same scaling as in Fig. 5.5b). The reciprocal lattice vector with the highest Fourier intensity is labelled G_0 for convenience.

In order to accomplish omni-directional light extraction by first order diffraction Archimedean lattices have been proposed [20]. In Fig. 5.9 Archimedean lattices with 7 holes per unit cell (A7) and 13 holes per unit cell (A13) are depicted. Due to the higher complexity of one unit cell a higher symmetry of the Fourier spectrum is achieved compared to the hexagonal lattice. Advantageously, twelve reciprocal lattice vectors with highest Fourier intensity are observed. Thus, omni-directional light extraction is achieved for the same range of guided modes as in the case of second order diffraction by the hexagonal lattice but with higher photonic strength. However, the diffraction coefficient calculated according to the photonic strength (5.2) and the diffraction model (4.37) shows a slightly worse performance of the A13 lattice compared to the hexagonal lattice, see Fig. 5.10a and Fig. 5.10b, respectively. This is attributed to the fact that due to the spreading of the Fourier spectrum the total Fourier intensity $|\Delta\varepsilon_{G,tot}|^2$ for all reciprocal lattice vectors $|G-G_0|<0.1k_0$ of the A13 lattice is ~20% smaller compared to the hexagonal lattice. By contrast, the hexagonal lattice extracts roughly only 82% of the guided mode with $\beta_m=2.4k_0$ by $G=G_0$, whereas the A13 lattice extracts every in-plane propagation direction. Thus, the hexagonal lattice empties the in-plane directions that it is capable of very fast according to its high Fourier intensities but

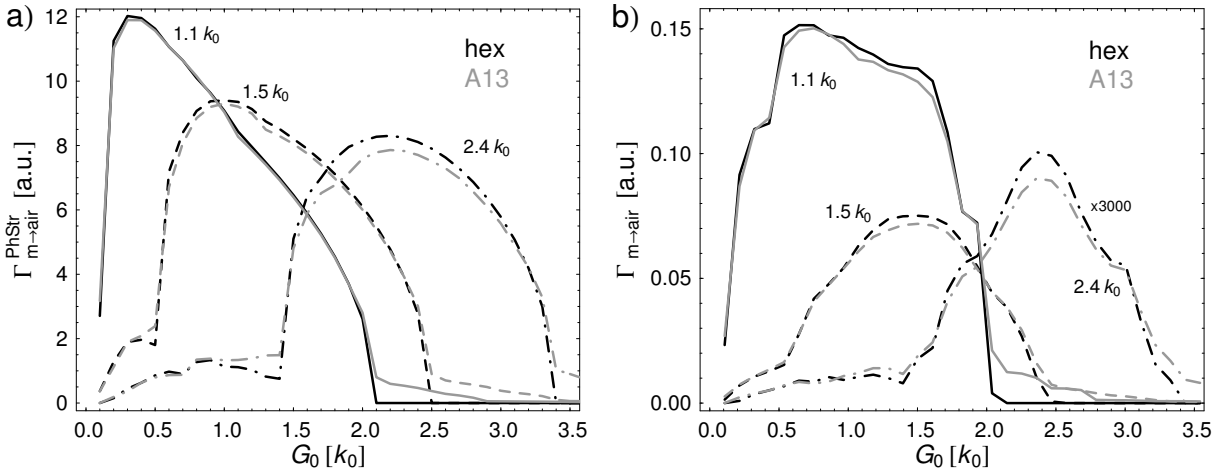

Fig. 5.10: (a) Diffraction coefficient according to the photonic strength (5.2) for the hexagonal lattice (black lines) and the A13 lattice (grey lines) and guided modes with $\beta_m = 1.1\,k_0$ (solid line), $\beta_m = 1.5\,k_0$ (dashed line), and $\beta_m = 2.4\,k_0$ (dash-dotted line). The A7 has been proven to show the same dependency as the A13 and is not shown for clarity. (b) Diffraction coefficient according to the diffraction (4.37) for the LED as given in the introduction to chapter 5 but with $F = 0.4$. This structure supports three TE-polarized modes at $\lambda = 558\,nm$ with $\beta_m \approx 1.1\,k_0$ (solid line), $\beta_m \approx 1.49\,k_0$ (dashed line), and $\beta_m \approx 2.4\,k_0$ (dotted line). Even though the A13 offers omni-directional diffraction it does not outperform the hexagonal lattice in terms of diffraction coefficients due to its lower Fourier intensities corresponding to $G = G_0$.

leaves the others unextracted. These directions have to be redistributed firstly and are prone to absorption during this process, before they potentially get diffracted to air. The A13 on the other hand depletes the guided mode uniformly but with lower Fourier intensities. In sum, both lattices perform almost similarly in terms of overall diffraction coefficients.

From these considerations, three regimes can be distinguished if we take absorption into account and the resulting in-plane dependency of the extraction efficiency of the guided modes, see (4.41):

i) In the case of heavily absorbing LED structures, i.e. when the absorption length is much shorter than the extraction length, it is necessary to extract the light as fast as possible. Thus, the hexagonal lattice is a good choice due to its higher Fourier intensities. Especially, if no high order diffraction processes contribute to the diffraction, i.e. for large β_m, the hexagonal lattice benefits from its high Fourier peaks of the primitive reciprocal lattice vectors.

ii) For less absorbing LEDs the Archimedean lattices take advantage of their omni-directional diffraction behaviour. The decrease in Fourier intensity compared to the hexagonal lattice is less important as light can propagate over larger distances before being absorbed.

iii) In the limit of vanishing absorption every diffraction process – even the higher ones – contribute similarly to the extraction. Hence, both lattice types offer omni-directional extraction behaviour and the hexagonal lattice catches up to the Archimedean lattices in terms of extraction efficiency.

In order to verify the above conclusions, Fig. 5.11 shows FDTD results for two different main reciprocal lattice vectors $G_0 = k_0$ and $G_0 = 2.3\,k_0$ of a hexagonal and an A13 PhC, both with $F = 0.5$. In the case of short $G_0 = k_0$ both lattices yield similar results as the diffraction coefficient is almost the same for every guided mode according to Fig. 5.10. This can also be seen from the almost parallel extraction characteristics. The slightly higher extraction of the A13 lattice is attributed to a larger range of guided modes diffracted

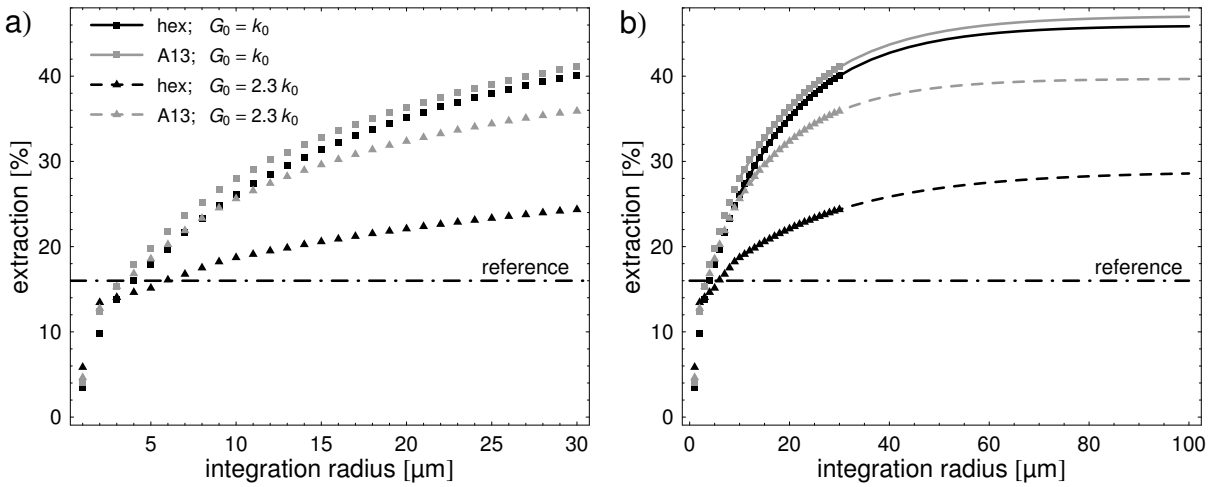

Fig. 5.11: FDTD simulation for the structure as given in the introduction to chapter 5 for two main reciprocal lattice vectors $G_0=k_0$ (solid line and boxes) and $G_0=2.3k_0$ (dashed line and triangles) of a hexagonal lattice (black lines and symbols) and a A13 lattice (grey lattice and symbols). (a) Extraction efficiency as calculated from the simulations; (b) the data from (a) along with the corresponding fits. The dash-dotted line gives the extraction efficiency of the unstructured LED.

omni-directionally, see Fig. 5.8b. By contrast, for large $G_0=2.3k_0$ a clear advantage of the A13 lattice is observed due to its omni-directionality. Thus, we can conclude that the presented LED operates in the intermediate regime (ii) with decreased absorption. The drop in efficiency for $G_0=2.3k_0$ compared to the short G_0 that is observed for both lattices stems from numerous guided modes supported by that LED each having different coupling strength. This issue is discussed in detail in section 5.2.2.

In conclusion, a hexagonal lattice only diffracts guided modes up to $\beta_m<2k_0$ omni-directionally by first order diffraction. In the case of Archimedean lattices with their twelve-fold symmetry the guided modes in the range $k_0<\beta_m<2.4k_0$ are folded entirely above the light line if $1.53k_0<G_0<1.93k_0$. In terms of diffraction coefficient both lattices perform equally regardless of the in-plane k-vector length with a slight advantage for the hexagonal lattice. However, the Archimedean lattices benefit all the more from their omni-directionality the lower the absorption of the LED structure is.

5.1.3 Filling Fraction

In order to derive the impact of the filling fraction on the diffraction behaviour we again utilize the photonic strength model. For each filling fraction the maximum diffraction coefficient was derived from a variation of the main reciprocal lattice vector, i.e. from a calculation as shown in Fig. 5.6. Fig. 5.12a shows these maxima for three guided modes and two lattice types, hexagonal and A13. As the PhC itself vanishes in the limits $F\rightarrow 0$ or $F\rightarrow 1$ the diffraction coefficient also decreases. The optimal filling fraction shifts with increasing in-plane k-vector length from $F=0.5$ down to $F=0.4$ for both lattices. As second order diffraction processes do not contribute to the extraction of the guided mode with $\beta_m=2.4k_0$, only the Fourier intensity of the main reciprocal lattice vectors is the decisive factor. According to Fig. 5.12b the total Fourier intensity of all **G** with $G=G_0$ is maximum for $F=0.4$. In contrast, if the guided mode is also diffracted by higher order diffraction processes, e.g. $\beta_m=1.1k_0$ or $\beta_m=1.5k_0$, the total Fourier intensity for all contributing **G** is maximum for

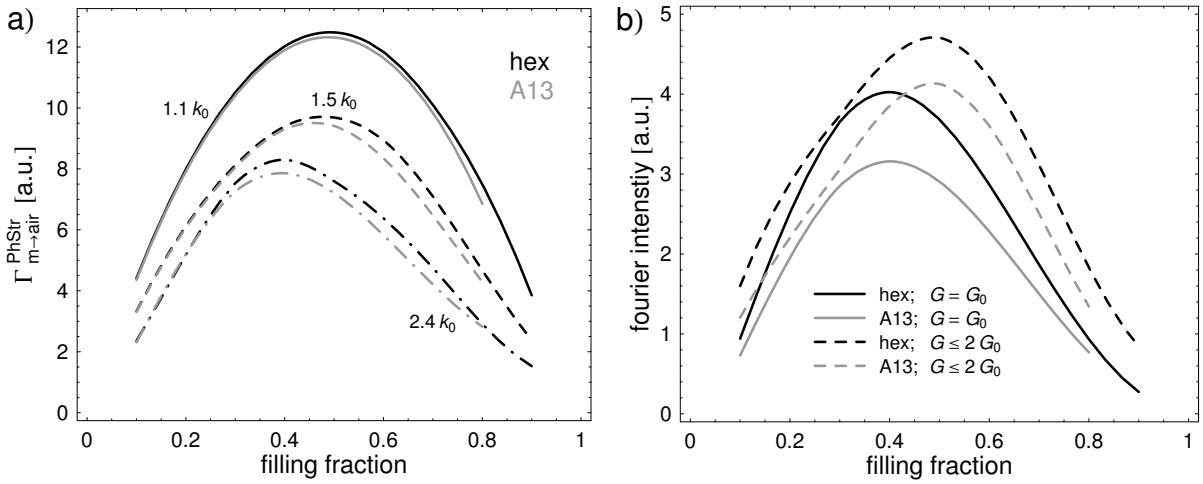

Fig. 5.12: (a) Maximum diffraction coefficient according to the photonic strength (5.2) as a function of the filling fraction for the hexagonal lattice (black lines) and the A13 (grey lines) and guided modes with $\beta_m = 1.1\,k_0$ (solid line), $\beta_m = 1.5\,k_0$ (dashed line), and $\beta_m = 2.4\,k_0$ (dash-dotted line). (b) Total Fourier intensity according to (4.39) for all $\boldsymbol{G}$ with $G = G_0$ (solid lines) and $G \le 2\,G_0$ (dashed lines). For decreasing in-plane k-vector length the optimal filling fraction shifts from 0.4 up to 0.5 as the Fourier intensity of higher order diffraction processes has to be taken into account.

F=0.5. Therefore, the optimal filling fraction depends on the guided modes that should be extracted[6].

The FDTD simulations in Fig. 5.13 show the same fundamental behaviour as predicted by the above considerations. However, the impact of the filling fraction on the overall extraction efficiency of the LED is less pronounced. Several issues have to be taken into account in this case. Firstly, the competition between absorption and diffraction weakens the influence of an enhanced diffraction coefficient. Variations of the latter due to an altered filling fraction only contribute fully to the extraction efficiency in case of heavy absorbing structures, as discussed at the end of section 4.2.2. Thus, in the case of intermediate absorption the impact of the filling fraction causing a change of the diffraction coefficient is

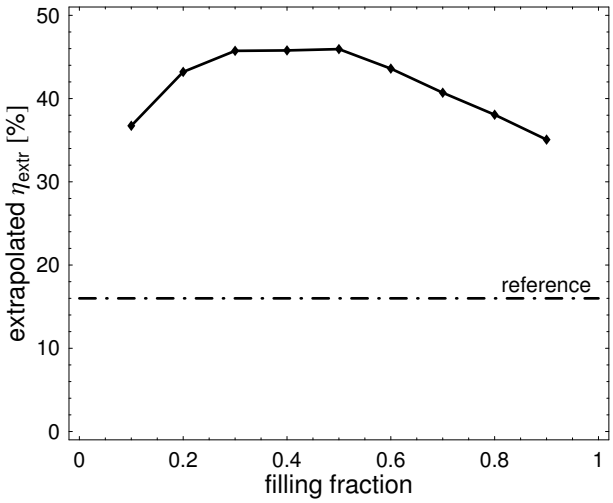

Fig. 5.13: FDTD simulation for the structure as given in the introduction to chapter 5 with varying filling fraction. The dots indicate the different simulations. The dash-dotted line gives the extraction efficiency of the unstructured LED. The filling fraction plays a minor role for the optimisation of PhC LEDs.

[6] We can also conclude from Fig. 5.12 that the three regimes of the former section regarding the absorption are valid for every filling fraction, as the hexagonal lattice always offers higher Fourier intensities compared to the A13. The omni-directionality, however, is independent of the filling fraction.

less pronounced. Additionally, the LED under consideration supports numerous guided modes in the range $k_0<\beta_m<2.4k_0$. Therefore, a distinct maximum is hardly to be expected. The high extraction efficiency for $F=0.3$ stems from the overlap of the guided modes with the PhC layer that varies for the different modes and filling fractions. This issue will be discussed in detail in the upcoming section. Thus, as long as the Fourier intensity of the main reciprocal lattice vectors is high (for filling fractions of $F=0.3$-0.5) the overall extraction efficiency is almost equal.

In conclusion, the filling fraction has only small impact on the extraction efficiency of PhC LEDs as long as it is chosen around $F=0.4$. Hence, in terms of processing it is a less crucial parameter.

5.2 Vertical Part: LED Layer Stack

After this detailed discussion regarding the two-dimensional part of PhC LEDs it is now of great importance to derive the impact of the vertical LED layer stack on the performance of such LEDs. However, the optimisation of the layer stack has to account for several issues beyond the pure optical optimisation in order to provide high wall-plug efficiency. For instance, sufficient current spreading has to be ensured to avoid current crowding within the LED and to achieve lateral homogenously injected carriers. Otherwise, the high current density at some areas decreases the internal quantum efficiency, whereas the remaining area generates almost no light. Thus, the overall efficiency is low compared to a LED with smooth current distribution. Other issues are ESD (electro-static discharge) stability and the aging of the devices.

In the upcoming section we restrict the discussion to considering a single guided mode and derive the relation between etch depth and diffraction coefficient. Afterwards, additional guided modes are included and the relevant distinctive factors are pointed out.

5.2.1 Etch Depth and LED Thickness

The etch depth of the PhC will be discussed for two reasons. Firstly and most important, its impact on the extraction efficiency will be investigated. Secondly, we will compare the diffraction coefficient of a single guided mode with an analytical expression found in [25]. Thus, we can give a verification of our model apart from the fully numerical FDTD simulations presented at the end of this section.

In [25] a thorough analysis of the diffraction coefficient of guided modes with $\beta_m>n_{PhC}k_0$ that are evanescent in the PhC, is given based upon Poynting flux considerations from [96]. By only taking into account the vertical field profile of the guided mode and the average refractive index of the PhC it is shown, that the diffraction coefficient is related to the remaining core thickness t by

$$\Gamma_{m\rightarrow air} \propto t^{-3}. \tag{5.3}$$

In Fig. 5.2 mode I and II show corresponding mode profiles. In [25] this dependency is compared to results from a three-dimensional scattering matrix algorithm and exhibits very good agreement. Thus, we can compare our results indirectly with an additional method solving Maxwell's equations without any assumptions.

Fig. 5.14 shows the diffraction coefficient (black solid line) obtained from the diffraction model for two TE-polarized guided modes, one with no roots named TE_0 (a) the other with 10 roots named TE_{10} (b) in their vertical mode profile. The calculations are

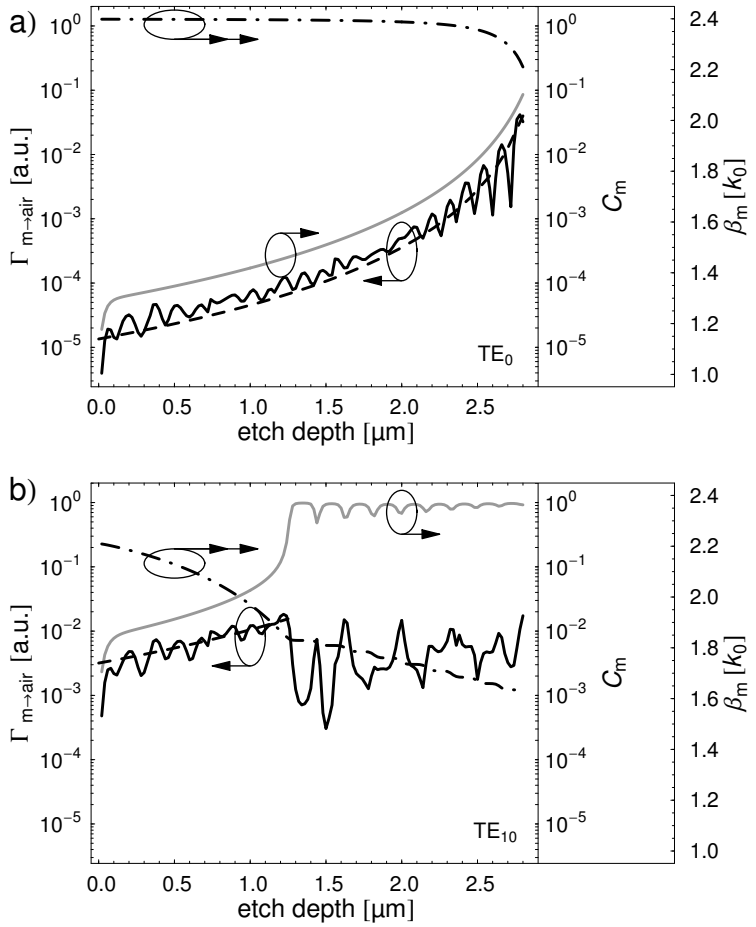

Fig. 5.14: Diffraction coefficient (black solid line, left y-axis) obtained from the diffraction model for guided modes with no roots (a), TE_0, and 10 roots (b), TE_{10}, in their vertical mode profile at $\lambda = 520$nm and $G_0 = 2.4k_0$. The remaining core thickness t is equal to a total GaN thickness of 3µm less the etch depth. The diffraction coefficient is in good agreement with a fit according to (5.3) (dashed black line, left y-axis) as long as $\beta_m > n_{PhC}k_0$ (black dash-dotted line, additional right y-axis). The fundamental characteristics of the diffraction coefficient are related to the overlap C_m of the vertical field profile with the PhC layer (grey solid line, right y-axis).

obtained from a structure as described in the introduction to this chapter at λ=520nm but with G_0=2.4k_0 and increasing etch depth in order to realize decreasing core thickness t. As the distance between the mirror and the source is only 160nm we used a maximum etch depth of the PhC of 2800nm in order to leave the active region unperforated.

First of all, we observe two different regimes that can be distinguished according to the eigenvalue (black dash-dotted line) of the TE_{10} guided mode [25]. On the one hand, as long as the mode is evanescent inside the PhC layer, $\beta_m > n_{PhC}k_0$, a monotonically increasing diffraction coefficient is obtained apart from some oscillations. On the other hand, as soon as $\beta_m < n_{PhC}k_0$ (mode III in Fig. 5.2) the diffraction coefficient shows fluctuating behaviour. We start our investigations with the first regime and expand them step by step to other properties of the guided mode, like absorption and spontaneous emission. Afterwards, the second regime is subject of our interest. In general, the dependency of the in-plane k-vector length of the guided modes on the remaining core thickness stems from a growing fraction of the low-index PhC while the high-index semiconductor gets thinner and thinner. Hence, the optical thickness of the layer stack given by $(n_{PhC}d+n_{GaN}t)/\lambda$ with the etch depth d decreases. With diminishing optical thickness less guided modes are supported by the stack and the guided modes' eigenvalues decrease. Before we close this chapter with results from FDTD simulations we briefly reconsider the filling fraction of the previous section as it links the lateral part to the vertical part of PhC LEDs.

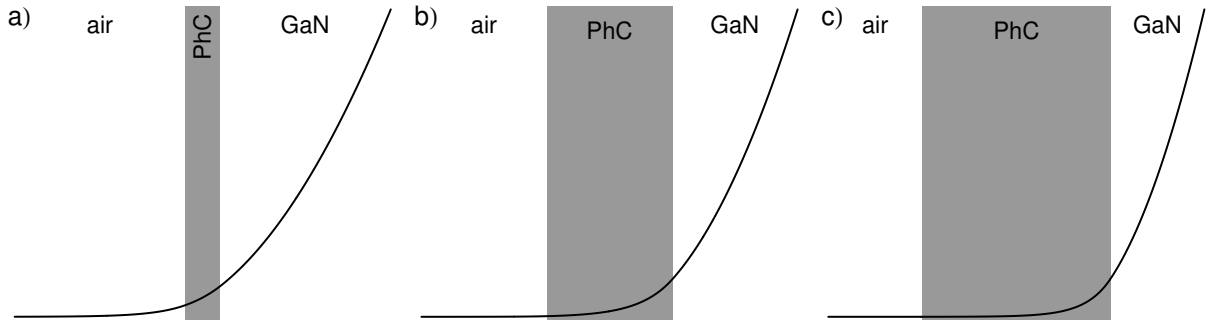

Fig. 5.15: Intensity profiles (black lines) of the TE_0 mode for different etch depths of the PhC (grey area) of 20nm (a), 100nm (b) and 200nm (c). The in-plane k-vector length of the guided mode is $\beta_m \approx 2.4 k_0$ and the attenuation length is 54nm in each case.

Initially, we observe a very good agreement between $\Gamma_{m\to air}$ (black solid line) calculated from the diffraction model and a fit (black dashed line) according to the t^{-3}-dependency of (5.3) for both modes as long as $\beta_m > n_{PhC} k_0$. The simulations with the scattering matrix algorithm in [25] also reveal oscillations similar to those in Fig. 5.14. These stem from the coupling of the guided mode with radiative modes. However, the fundamental contribution to the t^{-3}-dependency can now be related to the overlap C_m (grey solid line) of the vertical guided mode profile with the PhC layer as indicated in Fig. 5.14. For small PhC's etch depths <100nm, the attenuation length[7] $i/\gamma_{PhC,m}$ of the guided mode profile within the PhC layer is larger than the etch depth, see Fig. 5.15a. Hence, a steep increase of both $\Gamma_{m\to air}$ and C_m is found until the mode profile negligibly penetrates into air as shown in Fig. 5.15b. For etch depths >100nm, the diffraction coefficient grows since the guided mode is squeezed more and more between the mirror and the PhC layer and hence, the overlap with the PhC layer rises. This case is illustrated in Fig. 5.15c. Right before the eigenvalue of TE_{10} in Fig. 5.14b (black dash-dotted line) drops below $\beta_m = n_{PhC} k_0$ the diffraction coefficient reaches its maximum and further etching does not enhance the extraction of the guided mode anymore [25] even though C_m is very high. Hence, one might conclude that etching as deep as technologically possible is most preferable.

However, the absorption has to be taken into account that is present in thin-film LEDs due to the mirror. As C_m increases also the overlap of the guided mode with the mirror grows simultaneously for the same reason. Thus, as can be seen in Fig. 5.16 no net effect arises for the extraction efficiency of the guided modes due to deeper etching apart from the sharp resonances. Here, we calculated the ratio (black solid line) between the absorption coefficient α_m (4.19) and the diffraction coefficient from Fig. 5.14. The extraction efficiency cannot be calculated from this ratio as the in-plane diffraction behaviour has to be taken into account, see (4.41). However, it can be used as a measure for the extraction efficiency. Therefore, the extraction of a single guided mode is hardly enhanced due to deeper etching.

By contrast, the resulting overall extraction efficiency of the whole LED might be enhanced nevertheless, as it takes into account the extraction efficiency of each individual mode along with the spontaneous emission distribution. As can be seen in Fig. 5.16 the spontaneous emission (grey solid line) into the modes changes in different manner with increasing etch depth. Consider for instance a case with two guided modes, the overall extraction efficiency depends on the extraction efficiencies η_1 and η_2 of the two modes and the amount of spontaneous emission B_1 and B_2 and is given by

[7] Here, $\gamma_{PhC,m}$ is the vertical k-vector component of the guided mode β_m inside the PhC layer, i.e. j=index of PhC layer in (4.5).

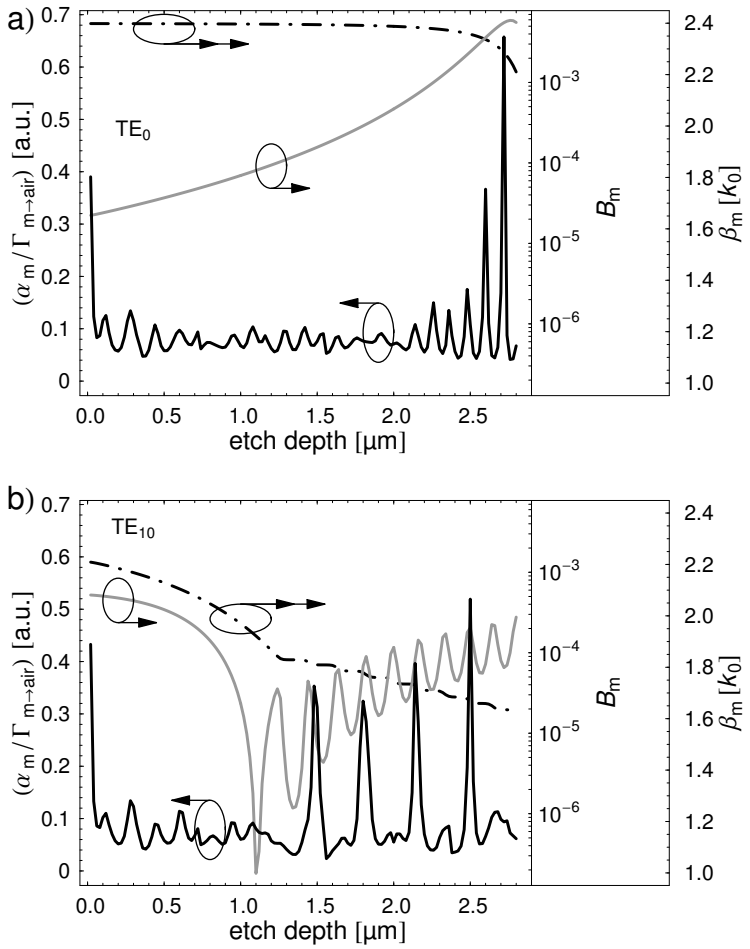

Fig. 5.16: Ratio (black solid line, left y-axis) between the absorption coefficient α_m and the diffraction coefficient as shown in Fig. 5.14 for the TE_0 (a) and the TE_{10} (b) guided mode at $\lambda = 520nm$ and $G_0 = 2.4k_0$. Due to the squeezing of the guided modes between the PhC and the mirror no net extraction enhancement is observed. Along with the in-plane k-vector length (black dotted line, additional right y-axis) is the overlap B_m of the guided mode with the active region shown (grey solid line, right y-axis).

$$\eta_{extr} = \frac{\eta_1 B_1 + \eta_2 B_2}{B_1 + B_2}. \tag{5.4}$$

From Fig. 5.17 it is evident, that a changed spontaneous emission distribution between guided modes significantly alters the overall extraction efficiency of the LED even though the extraction efficiency of each individual mode stays constant. In general, the overlap with the active layer is large as long as the guided mode is confined by the PhC and the mirror. As soon as $\beta_m < n_{PhC} k_0$ the upper boundary of the cavity is the semiconductor-to-air rather than the semiconductor-to-PhC interface. Thus, the guided mode profile is spread over a larger spatial dimension and the overlap decreases. However, in typical LEDs this effect averages out owing to the large number of supported guided modes and due to shallow etched PhCs.

Regarding the second regime, $\beta_m < n_{PhC} k_0$, we focus on the TE_{10} guided mode shown in Fig. 5.14b. In general, conclusions from the diffraction model have to be drawn with care as the overlap of the guided mode with the PhC is very large. Thus, we are about to leave the regime of weakly coupled PhCs. In the case of the dips in C_m the diffraction model should yield reliable results. These dips and the maxima in $\Gamma_{m\to air}$ can be identified with resonances of the guided mode's vertical field profile within the whole layer stack as shown in Fig. 5.18a (black and grey solid lines). The resonances are a result of the RCLED effect and stem from

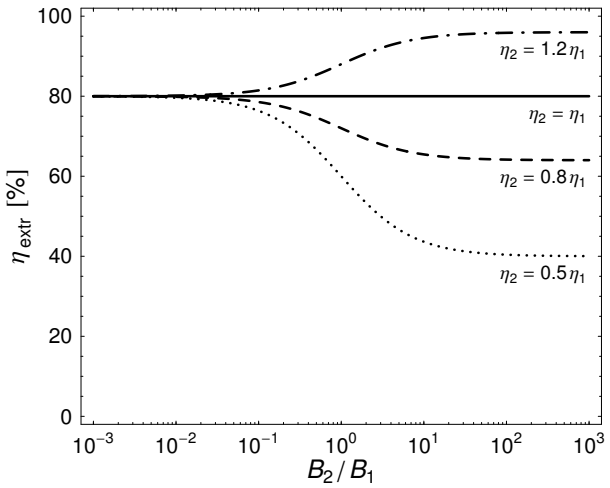

Fig. 5.17: Extraction efficiency according to (5.4) for a two mode case as a function of the spontaneous emission distribution between the two guided modes. The different lines correspond to $\eta_2 = \eta_1$ (solid line), $\eta_2 = 0.8\eta_1$ (dashed line), $\eta_2 = 0.5\eta_1$ (dotted line), and $\eta_2 = 1.2\eta_1$ (dash-dotted line) with $\eta_1 = 80\%$.

the constructive interference of up- and downward propagating plane waves. Hence, if we neglect the evanescent parts of the guided mode within air and within the mirror, the corresponding interference term reads

$$f(d) = \cos\left(d\, \gamma_{\mathrm{PhC,m}}(d) + t\, \gamma_{\mathrm{GaN,m}}(d) \right), \tag{5.5}$$

with d the etch depth, $d+t$ the overall LED thickness of 3µm in the above example and $\gamma_{\mathrm{GaN,m}}$ ($\gamma_{\mathrm{PhC,m}}$) the vertical k-vector component of the m-th guided mode inside the GaN (PhC) layer. The vertical k-vector components are functions of the in-plane k-vector length and hence depend on the etch depth. In the case of constructive interference the overall field amplitude within the vertical stack is higher compared to the case of destructive interference. Thus, even though the overlap with the PhC is low in the prior case, the coupling of the guided mode to radiative modes in general is high owing to the field enhancement. Therefore, the diffraction coefficient and the overlap with the active region B_{m} (black dashed line) follow these resonances. The former is additionally altered due to the coupling between the guided mode and the radiative modes. However, the absorption diminishes this benefit as it is also high in the case of constructive interference, see Fig. 5.18b (black dashed line). From the overlap with the PhC we can infer, that in the case of constructive interference the guided mode is mainly located inside the unetched core rather than inside the PhC layer owing to the dips of C_{m}. Nevertheless, high diffraction rates are obtained along with high spontaneous emission rates.

If we briefly summarize the findings made so far we can conclude that an optimum PhC LED consists of an unetched core that supports a single guided mode [25]. To ensure high spontaneous emission into that mode the active region should be embedded into this core. This, moreover, does not imply a loss of active area due to etching through the active layers. The PhC layer should be thicker than the attenuation length of the guided mode confined to the core. If this results in an overall thickness of the LED supporting more than one guided mode, the overall thickness and/or the position of the active layers should be adjusted for very low spontaneous emission into that additional mode. In this way, the PhC can be chosen for optimum diffraction of a single guided mode. However, to take advantage of the resonances a precise control over the layer thickness in the order of a few tens of nm is necessary. Furthermore, such a thin layer stack hardly provides reasonable current spreading. And apart from the active layer, also the functionality of current spreading layers is affected

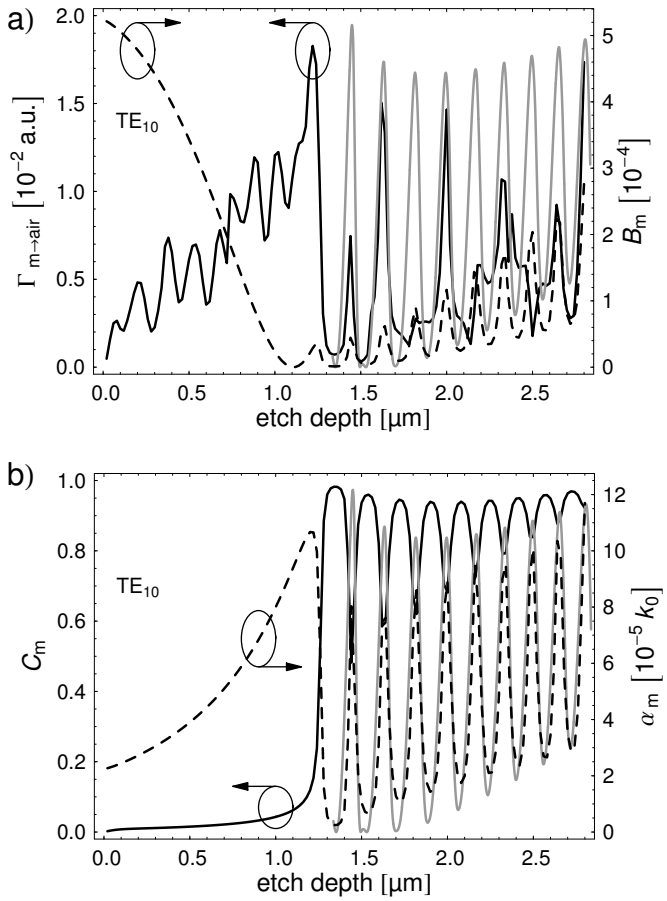

Fig. 5.18: (a) Comparison of the diffraction coefficient from Fig. 5.14b for the TE_{10} guided mode (black solid line and left y-axis) with the interference term (grey solid line) given in (5.5). The dashed line shows the overlap with the active region B_m (right y-axis). For the calculation of B_m the active region is placed 160nm above the mirror. (b) Corresponding overlap with the PhC C_m (solid black line and left y-axis) and absorption (dashed black line and right y-axis) in comparison to the interference term (5.5) (grey solid line).

by etching as the perforation limits their lateral conductivity. Typically, transparent conductive oxides (TCOs) can be used in such cases [33] in order to guarantee sufficient current spreading. However, the introduced absorption has carefully to be considered. Another possible workaround is presented in [26][27]. Here, the PhC is embedded into the vertical layer stack rather than etched into the semiconductor-to-air interface. This is accomplished by the challenging task of lateral epitaxial overgrowth. Nevertheless, the PhC can be used to define the thin core that supports only a single guided mode while above the PhC current spreading layers may follow that are thick enough to ensure reasonable current spreading. The modes mainly located in these layers exhibit only poor overlap with the active region within the core and thus gather only small amounts of spontaneous emission.

The last issue that remains open is the increasing absorption with decreasing core thickness due to the squeezing of the guided modes inside the unetched core. In order to separate the guided modes from the mirror, a non-absorbing layer with refractive index n_{low} well below that of GaN can be inserted between the mirror and the semiconductor. Consequently, the guided modes are pushed away from the mirror as long as they are evanescent inside the low index material, i.e. $\beta_m > n_{low} k_0$. As such layers are typically dielectrics and therefore isolating, electrical contact between the mirror and the semiconductor can be obtained by via holes through the low refractive index material filled with metal. Here, the lateral conductivity of the semiconductor puts an upper limit on the distance between the individual via holes.

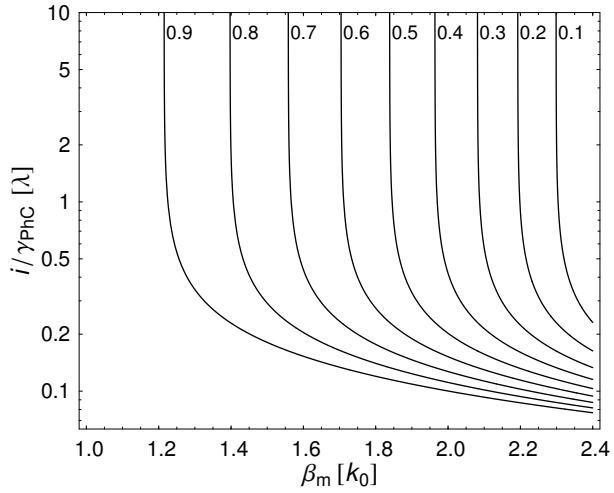

Fig. 5.19: Attenuation length of guided modes that are evanescent inside the PhC layer, $\beta_m > n_{PhC} k_0$, as a function of their in-plane k-vector length β_m and the filling fraction of the PhC. Each line is labelled with the corresponding filling fraction.

Before we verify our conclusions with FDTD let's briefly re-investigate the results of the FDTD simulations for the filling fraction in Fig. 5.13. For decreasing filling fraction the refractive index of the PhC tends towards the refractive index of the semiconductor, $n_{PhC} \rightarrow n_{GaN}$ for $F \rightarrow 0$. Consequently, the guided modes that are evanescent inside the PhC are less confined to the remaining core, their attenuation length $i/\gamma_{PhC,m}$ inside the PhC and their interaction with the PhC increases. Fig. 5.19 shows the attenuation length as a function of the in-plane k-vector length and the filling fraction. Hence, especially for the diffraction of strongly guided modes, $\beta_m \approx n_{GaN} k_0$, low filling fractions are preferable as long as the Fourier intensity of the first order is high. This contributes to the rather high extraction efficiency for a filling fraction of $F=0.3$ in Fig. 5.13.

Regarding the etch depths, Fig. 5.20a shows the extrapolated extraction efficiency obtained from FDTD simulations for the LED configuration as described in the introduction to this chapter with varying etch depth from 50nm to 1000nm. As an alternative to achieve reduced core thickness the extrapolated extraction efficiency for decreasing LED overall thickness at constant etch depth is given in Fig. 5.20b. As the investigated LED supports numerous guided modes, the interaction with the PhC, the spontaneous emission, and the absorption of each individual guided mode contributes in sum to the overall extraction efficiency. As we have seen during this section every mode reacts differently on an altered cavity and thus the net effect is hard to predict. However, we can identify the initial increase in extraction efficiency from 50nm to 100nm etch depth with the corresponding increase of the diffraction coefficient in Fig. 5.14 as long as the guided modes leak through the PhC layer into air. In contrast, as soon as the PhC layer is thick enough the extraction efficiency saturates as both the interaction of the guided modes with the PhC and the absorption at the mirror grow simultaneously. The slight increase for the 1µm thick PhC is attributed to a positive net effect owing to an altered distribution of guided modes and a reduced number of guided modes compared to the other cases. The deeper the PhC with its lower average refractive index is etched the less modes are guided by the layer stack. In general, it seems preferable to use PhCs on LEDs supporting only a low number of guided modes, as can be concluded from Fig. 5.20b. By continuously reducing the overall thickness and thus the number of guided modes the extraction efficiency increases. Due to the discrete diffraction behaviour of the PhC it extracts light more efficiently if it is distributed over a low number of guided modes. In general, an altered guided mode distribution calls for a re-adjustment of the PhC that has not been carried out in Fig. 5.20. Hence, even more extraction enhancement can be expected by reducing the total number of guided modes.

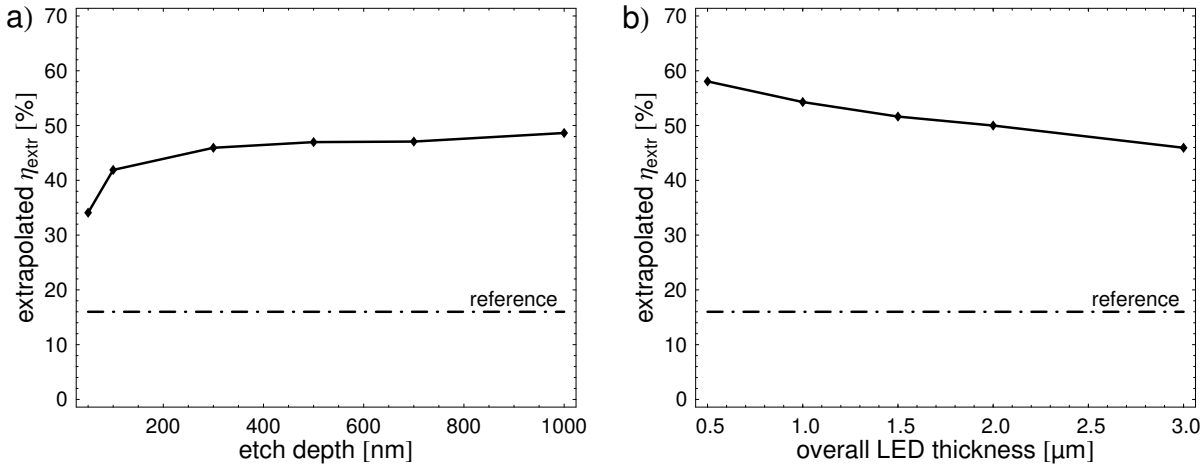

Fig. 5.20: FDTD simulation for the structure as given on page 49 with (a) varying etch depth at constant overall thickness of 3µm and (b) varying overall thickness at constant etch depth of 300nm. The dots indicate the different simulations. Only the extrapolated extraction efficiencies are shown. The dash-dotted line gives the extraction efficiency of the unstructured LED.

In conclusion, to ensure sufficient interaction of the guided modes with the PhC it should be etched deeper than the attenuation length of the modes within the PhC layer. Further etching enhances the diffraction coefficient as long as the guided mode is evanescent within the PhC layer. However, the absorption and the spontaneous emission of each mode have carefully to be considered in order to ensure high overall extraction efficiency of the LED. Also the impact of etching on the light generation area and consequently on the wall-plug efficiency owing to insufficient current spreading or perforation of the active region have to be taken into account while optimising a PhC LED. In general, thin vertical layer stacks are preferable due to a low number of guided modes.

5.2.2 Multimode Case

As the previous discussion suggested various quantities have to be taken into account in order to determine the optimum main reciprocal lattice vector length G_0 for extracting as much light as possible from a multimode LED. Additionally, due to the discrete diffraction behaviour none PhC lattice extracts all guided modes reasonably. For instance in the case of GaN, only a small window $1.4k_0<G_0<2k_0$ diffracts every guided mode in the range $k_0<\beta_m<2.4k_0$ into air. However, the diffraction coefficient for the different modes varies according to the mismatch between their in-plane k-vector length and the chosen main reciprocal lattice vector length. Consequently, the choice of G_0 relies on the interaction of each guided mode with the PhC, the amount of spontaneous emission and the Fourier spectrum of the PhC.

If we consider the usual sample LED and calculate the overlaps with the active region B_m and the PhC layer C_m – as a first approximation to the coupling integral in the case of shallow PhCs – we obtain Fig. 5.21. Due to the nearby located mirror and the resulting interference the overlap with the active region exhibits two distinct maxima in the case of TE-polarized guided modes. The second maximum in the case of TM-polarisation is less pronounced as only horizontal dipoles are taken into account. Thus, only the in-plane component of the guided mode's electric field contributes to Fermi's Golden Rule (2.3), i.e. determines the local electric field amplitude. Guided modes with $\beta_m<n_{PhC}k_0$ are best suited for diffraction since they interact strongly with the PhC and gather a significant amount of spontaneous emission. This mode region is highlighted by calculating the overlap product B_mC_m. However, the resonance of C_m does not necessarily result in high diffraction coefficients according to the findings of the previous section. The radiative modes show

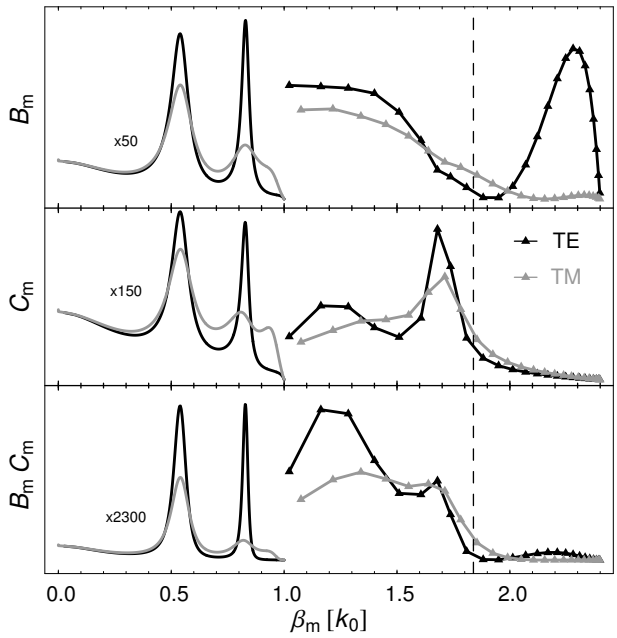

Fig. 5.21: Overlap with the active region B_m, with the PhC layer C_m and the corresponding product $B_m C_m$ at peak wavelength $\lambda_{peak}=520$nm for TE-polarized guided (black triangles), TE-polarized radiative (black lines), TM-polarized guided (grey triangles), and TM-polarized radiative (grey lines) modes. The LED structure is described in the introduction to this chapter. The dashed vertical line indicates $\beta_m = n_{PhC} k_0$.

typical Fabry-Perot-like resonances due to the cavity formed by the semiconductor-to-air interface and the mirror. Their impact on the diffraction process is discussed in detail in section 5.3.2.

In order to prove our forecast regarding the optimum mode region we calculate the overall diffracted intensity in air in dependence of the main reciprocal lattice vector length G_0, as shown in Fig. 5.22a. The overall diffracted intensity in air is obtained by summing up the diffraction coefficient $\Gamma_{m\rightarrow air}$ of every TE- and TM-polarized guided mode weighted with B_m. When $G_0=k_0$ ($a=600$nm) guided modes from the region with high overlap product are diffracted by first order diffraction and thus, high diffracted intensities are obtained. Even though the density of guided modes with $\beta_m>2k_0$ is high and these modes gather a large amount of the total spontaneous emission the extremely low interaction with the PhC suppresses efficient light extraction from these modes. Hence, the overall diffracted intensity in air drops when adjusting the PhC to this mode region, i.e. $G_0>2k_0$ or $a<300$nm. On the other hand, rather short $G_0<k_0$ cannot diffract the modes with $\beta_m\approx 1.7k_0$ sufficiently to air.

A comparison of the results received from the diffraction model with full numerical FDTD simulation as shown in Fig. 5.22b reveals an excellent forecast of the optimum G_0. Also the characteristics of the extraction efficiency as a function of G_0 correspond very well with the prediction of the diffraction model. The impact of absorption and of light that escapes the structure without the help of the PhC weakens the impact of reciprocal lattice vector as these are not included into the diffraction model.

In conclusion, the main reciprocal lattice vector with its maximum Fourier intensity should be adjusted to the mode region exhibiting both high interaction with the PhC and high overlap with the active region. This ensures high diffracted intensities. The optimisation of the overall extraction efficiency, however, additionally has to include the absorption of the guided modes.

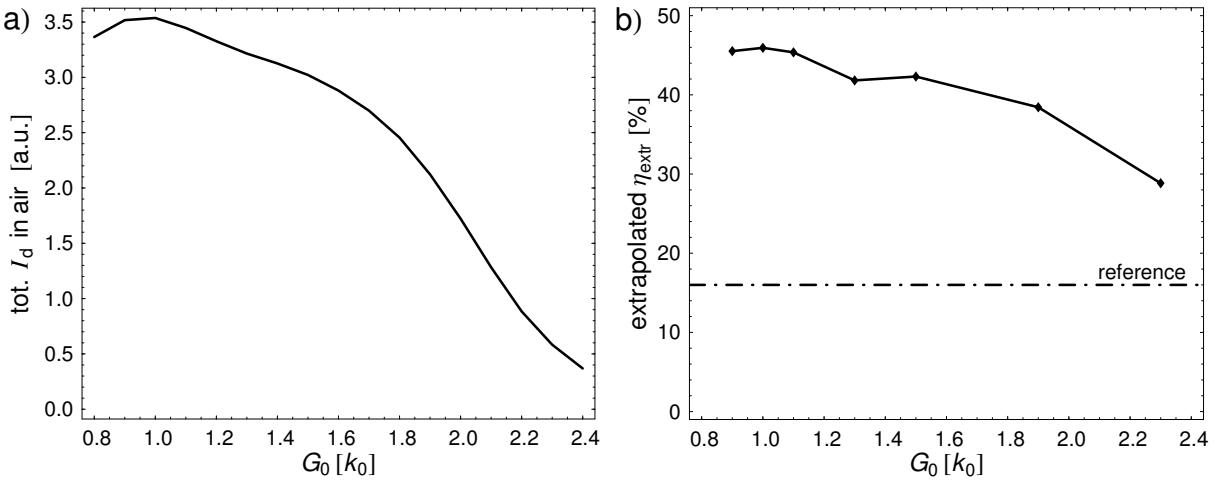

Fig. 5.22: (a) Total diffracted intensity I_d in air obtained from the diffraction model for varying main reciprocal lattice vector length G_0. Results include a Gaussian wavelength average for the LED as introduced on page 49. (b) Extrapolated extraction efficiency obtained from FDTD corresponding to (a). The dash-dotted line gives the extraction efficiency of the unstructured LED. The extraction efficiency is well predicted by the diffraction model even though absorption and directly emitted light are neglected.

5.2.3 Spontaneous Emission Distribution

As the last remaining parameter in this section we discuss different distributions of spontaneous emission between the guided modes. So far, only little attention has been paid to this issue in literature. According to the RCLED effect it is sufficient to change the distance between the active layer and the mirror in order to alter the spontaneous emission. Thus, all other parameters stay constant, namely the eigenvalues of the modes, the overlap with the PhC and the absorption of the guided modes. The impact of the semiconductor-to-air interface on the spontaneous emission distribution can be neglected as it is several wavelengths away from the active region. Fig. 5.23 shows the overlap with the active region of TE-polarized guided modes for different distances between the active layer and the mirror. The resonances due to the interference of the source with its mirror image shift towards larger in-plane k-vector lengths and additional resonances occur with increasing distance. For short distances <70nm surface plasmons play an important role for the spontaneous emission as described in

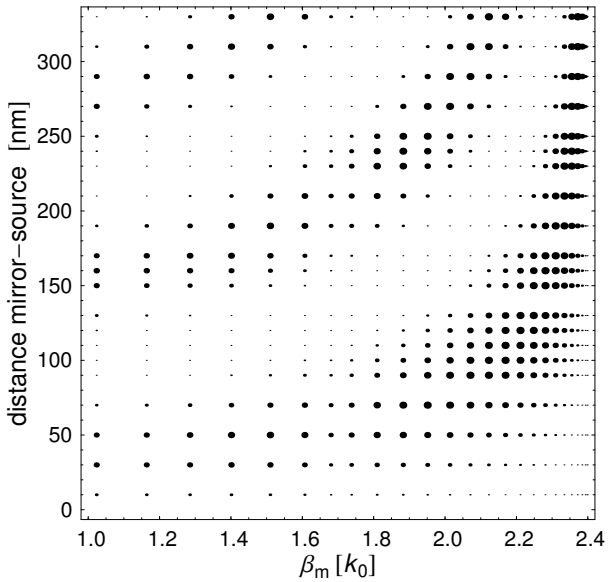

Fig. 5.23: Overlap with the active region of TE-polarized guided modes for different distances between the source and the mirror. The dot diameter is proportional to the overlap.

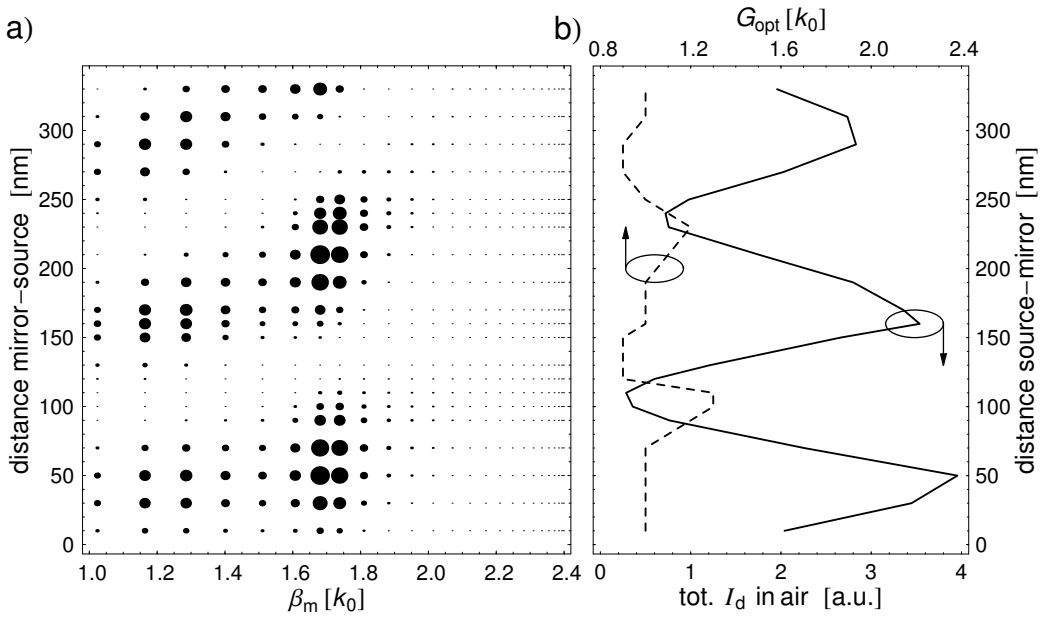

Fig. 5.24: (a) Overlap product of TE-polarized guided modes for different distances between the source and the mirror. The dot diameter is proportional to the overlap product. (b) Total diffracted intensity in air (solid line) and optimum G_0 for varying distance between the source and the mirror.

chapter 6. Hence, the results are only shown for completeness but not discussed in detail.

For every distance we calculated the diffracted intensity in air as a function of G_0, see Fig. 5.22a, and collected the maximum along with the corresponding optimum main reciprocal lattice vector length G_{opt} in Fig. 5.24b. The minima of the diffracted intensity at 110nm and 240nm coincide with configurations revealing poor overlap product for every guided mode, see Fig. 5.24a. The mismatch between the guided modes with high B_m and guided modes with high C_m causes the overall low overlap product. In contrast, when the two regions overlap, e.g. at 50nm, 160nm, and 290nm, a large amount of the generated light is diffracted efficiently to air. For increasing distance the difference between a maximum and the following minimum decreases as more and more resonances enter B_m, see Fig. 5.23. These resonances get sharper and consequently the mode region with high overlap product, too. Thus, only few modes are best suited to diffraction compared to shorter distances and the overall diffracted intensity in air diminishes.

The fundamental relationship between the overlap product and the diffracted intensity to air is also reflected by the fact that the optimum G_0 roughly follows the guided mode region with highest overlap product. For instance, at a distance of 130nm the guided modes around $\beta_m \approx 1.2k_0$ have maximum overlap product and $G_{opt}=0.9k_0$. With increasing distance G_{opt} successively moves up to $G_{opt}=1.2k_0$ at 240nm and the optimum overlap product shifts to $\beta_m \approx 1.7k_0$.

The mismatch between G_{opt} and the in-plane k-vector length corresponding to the maximum overlap product stems from the discrepancy between the overlap product and the exact coupling integral κ_{mk}. In Fig. 5.25 C_m is shown along with κ_{mk} summed over every radiating mode $\beta_k < k_0$ according to

$$\kappa_m = \sum_{\beta_k < k_0} \kappa_{mk} \ . \tag{5.6}$$

By calculating the overlap product with κ_m instead of C_m the resonance at $\beta_m \approx 1.7k_0$ vanishes in Fig. 5.24a and the main contribution to the diffracted intensity results from guided modes around $\beta_m \approx 1.2k_0$. Nevertheless, the overlap C_m with the PhC layer is a practical approximation to the coupling integral.

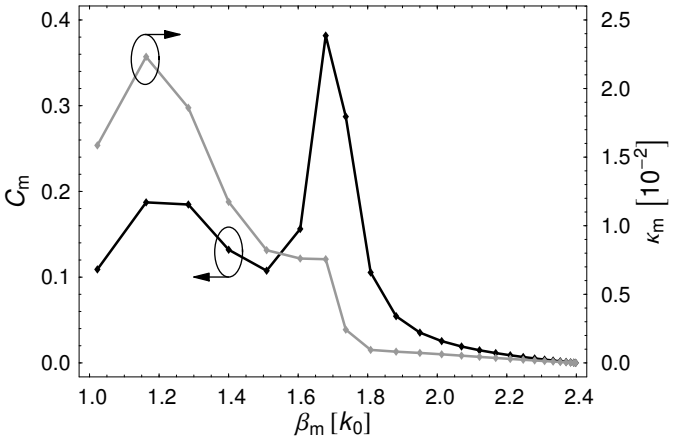

Fig. 5.25: Overlap C_m with the PhC layer (black symbols; left y-axis) and summed coupling integral κ_m (grey symbols; right y-axis) for TE-polarized guided modes at peak wavelength of the LED described in the introduction to chapter 5. The lines are just a guide to the eye.

The results from FDTD simulations as shown in Fig. 5.26 confirm the basic characteristics derived from the diffraction model in Fig. 5.24b. However, the main reciprocal lattice vector was not adjusted for every distance, but was kept constant at $G_0=k_0$. The enormous dependency of the diffracted intensity to air is weakened in the presence of absorption and directly emitted light. The slightly better extraction efficiency for a distance of 140nm is attributed to a higher extraction efficiency of the directly emitted light compared to 160nm, see Fig. 2.10a.

In conclusion, the major amount of the total emission should be gathered by guided modes with reasonable interaction with the PhC. Hence, it is not sufficient to only generate a guided mode region with high overlap product but this region should be as broad as possible. Here, the PhC defines an upper limit as it only diffracts guided modes with $|G-\beta_m|<k_0$ into the extraction disk. Furthermore, the guided modes in resonance with the PhC layer should not be chosen for diffraction, as the corresponding coupling integral is rather low. With regard to processing, the layer thicknesses have to be controlled within 20nm according to the diffraction model. However, owing to absorption and direct emission the impact of deviations is less crucial.

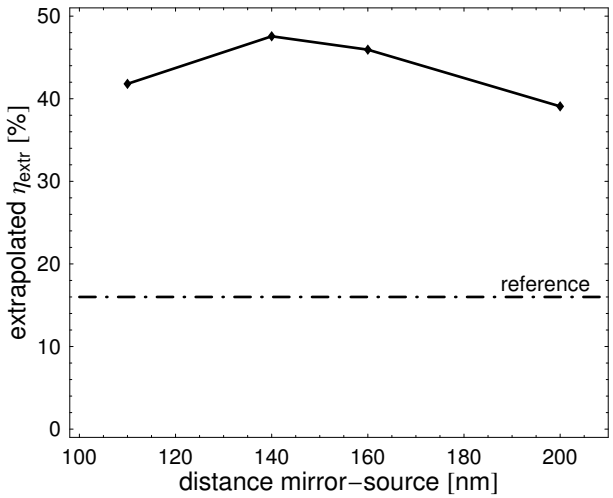

Fig. 5.26: Extrapolated extraction efficiencies obtained from FDTD simulations for constant $G_0=k_0$ around the maximum in diffracted intensity occurring at 160nm in Fig. 5.24b.

5.3 Directionality

After this detailed discussion regarding the parameter choice in order to obtain high extraction efficiency from PhC LEDs we now dedicate ourselves to the emission pattern. Of special interest in this regard is the ability of the PhC to collimate the far field, i.e. to extract the light primarily towards the surface normal. As discussed in 2.4 this is of great interest for étendue limited applications, when a larger fraction of the emitted light needs to be extracted into a limited numerical aperture of an optical system. The radiant flux emitted into this limited angle with respect to the overall emitted flux is referred to as directionality. Additionally, PhCs open the road to asymmetrical far fields by incorporation of one-dimensional gratings [32] or to generate flat far fields, so-called batwing shaped emission patterns.

We start with basic geometrical considerations in order to derive some limitations for the beam shaping properties of the PhC. Afterwards, we also take into account the impact of the vertical layer stack on the directionality. Here, we firstly discuss the dependency of the directionality on the radiative modes. Secondly, the guided mode distribution is taken into account. Finally, the impact of the omni-directionality of the PhC lattice on the far field shape is investigated.

5.3.1 Geometrical Considerations

The limited numerical aperture in air corresponding to an acceptance angle θ_L translates into an in-plane k-vector length $\beta=k_0\sin\theta_L$ in k-space. Hence, we can distinguish the diffracted k-vectors within the extraction disk into two separate cases, see Fig. 5.27. Firstly, all k-vectors with $k_0\sin\theta_L<\beta_k<k_0$ that are diffracted outside the limited acceptance angle and therefore, decrease the directionality. In contrast, the k-vectors with $\beta_k<k_0\sin\theta_L$ enhance the directionality. The directionality resulting from the diffraction of a single guided mode is then given by the ratio between the diffracted intensity into the desired extraction cone and the total diffracted intensity. We will show that even for single-mode scattering it is not possible to achieve 100% directionality within acceptance angles $\theta_L<90°$ since simultaneously to diffraction within this angle diffraction outside of it takes place.

In order to estimate the degree of directionality, we first assume constant diffracted intensity I_d from every in-plane propagation direction $\boldsymbol{\beta}_m/\beta_m$ of the guided mode, i.e. κ_{mk}=const. If we further neglect the curvature of the mode's circle by choosing $\beta_m \gg k_0$ and $G=\beta_m$, the directionality in this mono-mode case boils down to the ratio of two lengths

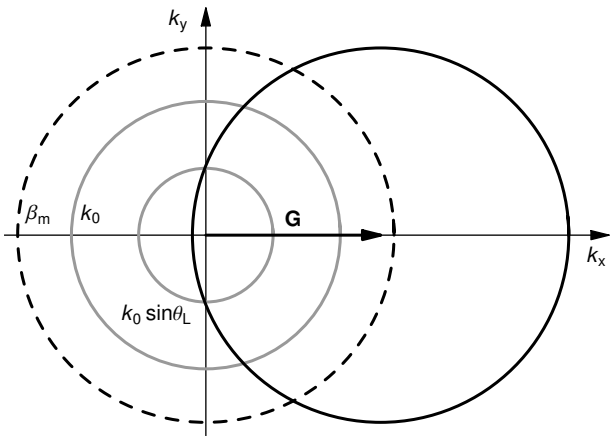

Fig. 5.27: Illustration of the diffraction process. The inner grey circle depicts a limited acceptance angle θ_L in air.

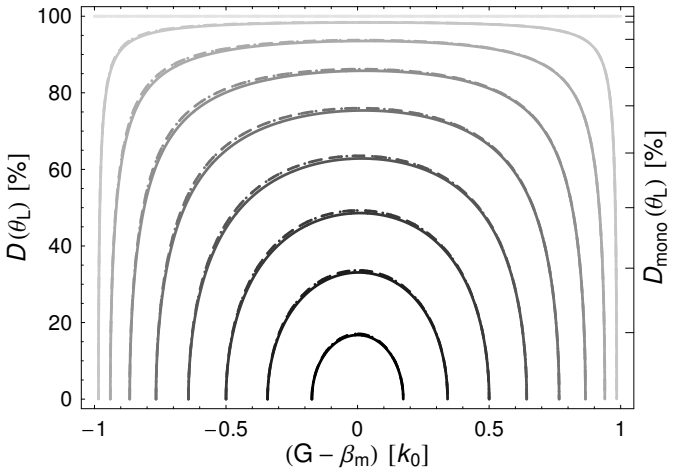

Fig. 5.28: Directionality within different acceptance angles as a function of the mismatch between the in-plane k-vector length and the reciprocal lattice vector length for three guided modes with $\beta_m = 1.1k_0$ (solid line), $\beta_m = 1.5k_0$ (dashed line), and $\beta_m = 2.4k_0$ (dotted line); fading black indicates different θ_L ranging from 10° to 90° in steps of 10°. The in-plane k-vector length has almost no impact on the resulting directionality. The latter is maximum for $G = \beta_m$ and is reasonably represented by the mono-mode result from (5.7). The ticks of the right y-axis are drawn at the values of the directionality in the mono-mode case corresponding to the acceptance angles.

$$D_{\text{mono}}(\theta_L) = \frac{2k_0 I_d \sin\theta_L}{2k_0 I_d} = \sin\theta_L . \tag{5.7}$$

The numerator (denominator) is the diameter of the circle corresponding to the limited acceptance angle (the diameter of the extraction disk). By contrast, a typical roughened thin-film LED has a Lambertian emission profile [59] with directionality $D_{\text{Lam}}(\theta_L)=\sin^2\theta_L$, i.e. the directionality in this case is the ratio of two areas, the disk within the limited acceptance angle and the extraction disk. Hence, we can expect more enhancement for smaller acceptance angles, since the mono-mode case is by a factor of $1/\sin\theta_L$ more directional than a Lambertian emitter. For instance, the Lambert yields 25% (75%) directionality within an acceptance angle of $\theta_L=30°$ ($\theta_L=60°$), whereas the mono-mode case has 50% (87%) and thus, is 2x (1.15x) more directional.

Fig. 5.28 depicts the directionality as a function of the mismatch between the in-plane k-vector length β_m and the reciprocal lattice vector length G. We used (5.1) to calculate the directionality, where k_0 was replaced by $k_0\sin\theta_L$. In contrast to the total arc length within the extraction cone as shown in Fig. 5.4 the curvature and the in-plane k-vector length have only negligible impact on the directionality within θ_L. Thus, the deviation from the mono-mode case can be neglected and maximum directionality is achieved for $G=\beta_m$.

In order to study the contribution of additional guided modes to the directionality consider for instance Fig. 5.29a. Here, the diffraction of three guided modes is illustrated with in-plane k-vector lengths $\beta_1<\beta_2<\beta_3$ by a single reciprocal lattice vector with $G=\beta_2$. According to the above findings diffraction of β_2 results in maximum directionality, whereas diffraction of β_3 decreases the overall directionality as no diffracted k-vectors lie within the limited acceptance angle, $\beta_d=|\boldsymbol{\beta}_3-\mathbf{G}|>k_0\sin\theta_L$. The resulting k-vectors from diffraction of β_1 contribute positively to the directionality. But they do not necessarily give an improvement compared to a Lambertian emitter as the fraction of diffracted k-vectors within the limited acceptance angle has to be larger than $D_{\text{Lam}}(\theta_L)$. The analogous conclusions can be drawn if more than one reciprocal lattice vector diffracts a guided mode into the extraction disk as sketched in Fig. 5.29b.

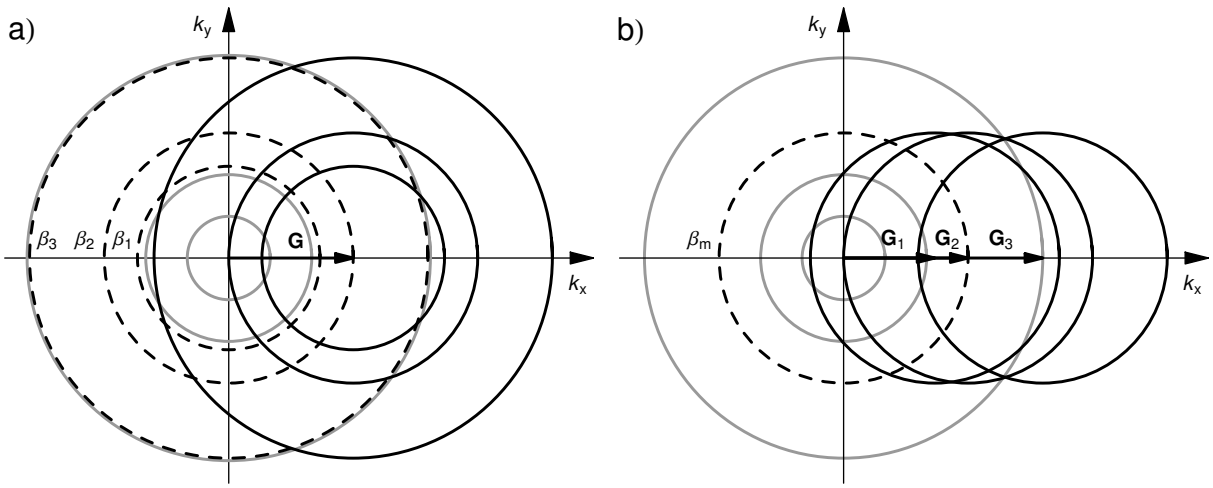

Fig. 5.29: (a) Geometrical construction to determine the contribution of several guided modes to the directionality; the guided modes have $\beta_1 = 1.1\,k_0$, $\beta_2 = 1.5\,k_0$, and $\beta_3 = 2.4\,k_0$ and $G = \beta_2$. (b) Analogous construction to (a) for a single guided mode $\beta_m = 1.5\,k_0$ but three reciprocal lattice vectors with $G_1 = 1.1\,k_0$, $G_2 = \beta_m$, and $G_3 = 2.4\,k_0$. Only if $|\beta_m - G| < k_0 \sin\theta_L$ the diffraction process improves the directionality within θ_L.

A quantitative investigation of the directionality resulting from diffraction of two guided modes is given in Fig. 5.30a where the overall directionality was calculated according to (5.1) for two modes. Since we have chosen $G=\beta_2$ the second mode with in-plane k-vector length β_1 contributes equally to the directionality for small differences $\beta_2-\beta_1$. For increasing mismatch between the two modes diffraction of the second mode decreases the overall directionality until a minimum is reached at $|\beta_2-\beta_1|=k_0\sin\theta_L$. Here, the arc length within the extraction cone but outside the limited acceptance angle is decisive. As the characteristics of the directionality are rather flat up to the vicinity of the minimum a large fraction of guided modes within the range $|\beta_m-G|<k_0\sin\theta_L$ contribute similarly to the directionality. With growing $|\beta_2-\beta_1|$ the arc length of mode β_1 diminishes and the overall directionality reaches the mono-mode maximum. Hence, guided modes with $\beta_m \approx |G \pm k_0|$ contribute negligibly to the directionality. The asymmetry of the overall directionality with respect to $\beta_2-\beta_1=0$ is up to the fact that due to the curvature the mentioned arc length is larger if $\beta_1>G$ compared to $\beta_1<G$ for a given difference $|\beta_2-\beta_1|$. For larger in-plane k-vectors this asymmetry vanishes since the curvature is less dominating. The same characteristics are observed in Fig. 5.30b

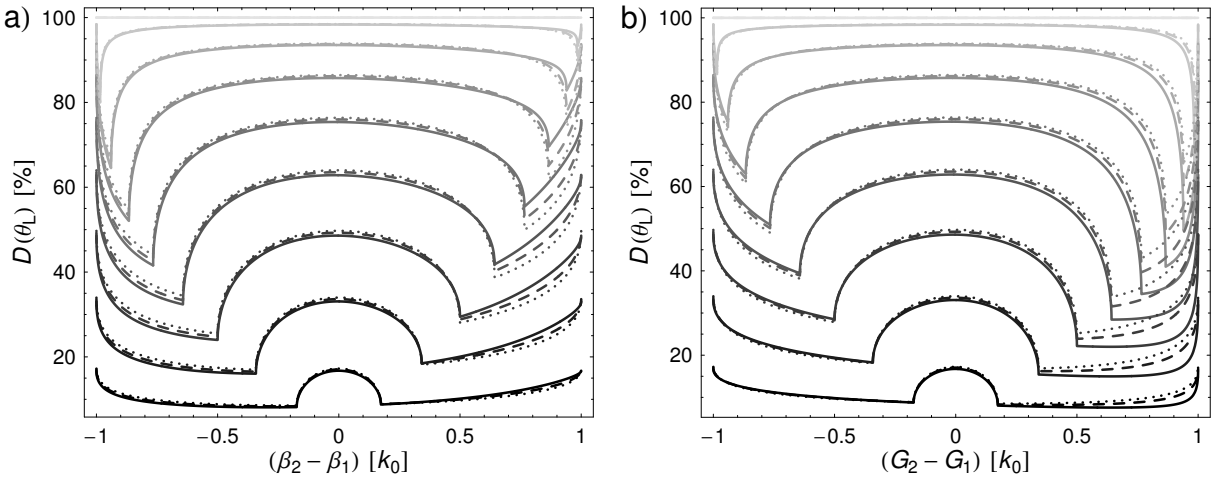

Fig. 5.30: (a) Overall directionality within an acceptance angle θ_L ranging from 10° to 90° in steps of 10° (illustrated by different grey levels) resulting from diffraction of two guided modes with in-plane k-vector length β_1 and β_2 by a reciprocal lattice vector with $G=\beta_2$. The solid/dashed/dash-dotted line corresponds to $\beta_2 = 1.1\,k_0$, $\beta_2 = 1.5\,k_0$, and $\beta_2 = 2.4\,k_0$, respectively. (b) Analogous calculation for a single guided mode β_m and two reciprocal lattice vectors with G_1 and $G_2=\beta_m$.

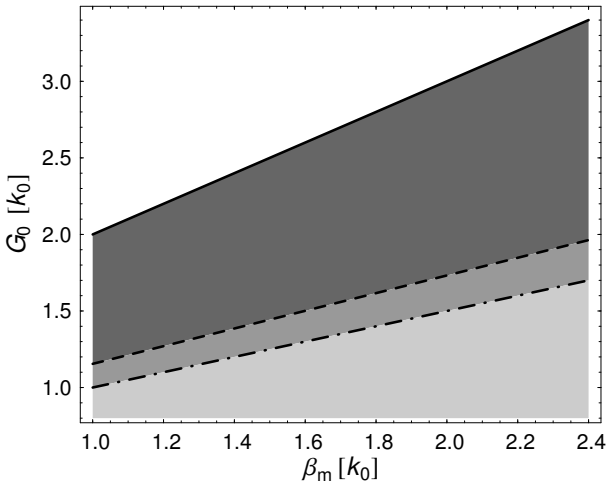

Fig. 5.31: The dark grey area indicates the range of main reciprocal lattice vector lengths G_0 that result only in first order diffraction of the guided mode with in-plane k-vector length β_m into the extraction disk. In the narrow region between the dashed and the dash-dotted line also the second order process with $G=3^{1/2}G_0$ contributes to the diffraction. Below the dash-dotted line further high order processes cannot be avoided. Above the dark grey area the guided mode is not diffracted into the extraction disk.

when a single guided mode β_m is diffracted by two reciprocal lattice vectors $\mathbf{G}_1$ and $\mathbf{G}_2$ with $G_2=\beta_m$. Only the asymmetry is worse, as the curvature of the diffracted circle does not change owing to constant β_m. In contrast, in Fig. 5.30a the curvature decreases as β_1 increases.

Due to the discrete Fourier spectrum of a PhC only few different reciprocal lattice vector lengths occur. Consider for instance a hexagonal lattice with its main reciprocal lattice vector length G_0 and the two second order diffraction processes with length $G_a=3^{1/2}G_0$ and $G_b=2G_0$. The differences G_a-G_0 and G_b-G_0 are in general too large to result in diffracted k-vectors within the same acceptance angle. Consequently, in terms of directionality higher order processes should be avoided, i.e. the resulting k-vectors should lie outside the extraction disk, $|\beta_m-G|>k_0$ for $G>G_0$. Fig. 5.31 illustrates the range of G_0 that result only in diffraction processes by G_0 within the extraction disk as a function of β_m (dark grey area). Owing to their lower Fourier intensity the impact of higher order diffraction processes on the directionality is moderated, but they still should be eliminated.

In conclusion, we have again seen that a mono-mode LED is most preferable to achieve highest directionality, too. Additional guided modes are only acceptable as long as they can be diffracted into the limited acceptance angle, i.e. $|\beta_m-G|<k_0\sin\theta_L$ for a given G. In order to achieve an improved directionality compared to the Lambertian emitter, this range has to be further clipped as the fraction of the diffracted circle within the limited acceptance angle has to be larger than the corresponding fraction of the Lambertian. In any case, higher order diffraction processes should be avoided when targeting directionality, since they hardly diffract light into the same limited acceptance angle as the first order process. Furthermore, it is not possible to achieve 100% directionality within any acceptance angle $\theta_L<90°$ because along with diffraction into this angle diffraction outside cannot be omitted.

5.3.2 Radiative Modes and Directionality

For the derivation of the directionality in the mono-mode case (5.7) we assumed constant diffracted intensity from every in-plane propagation direction towards air or equivalently constant coupling of the guided mode with every radiative mode. This assumption, however, has to be proven as the coupling integral is hardly constant, see Fig. 5.7b. For instance, the coupling integral with mode V in Fig. 5.2 is probably larger than with mode IV due to the different field intensities within the PhC layer.

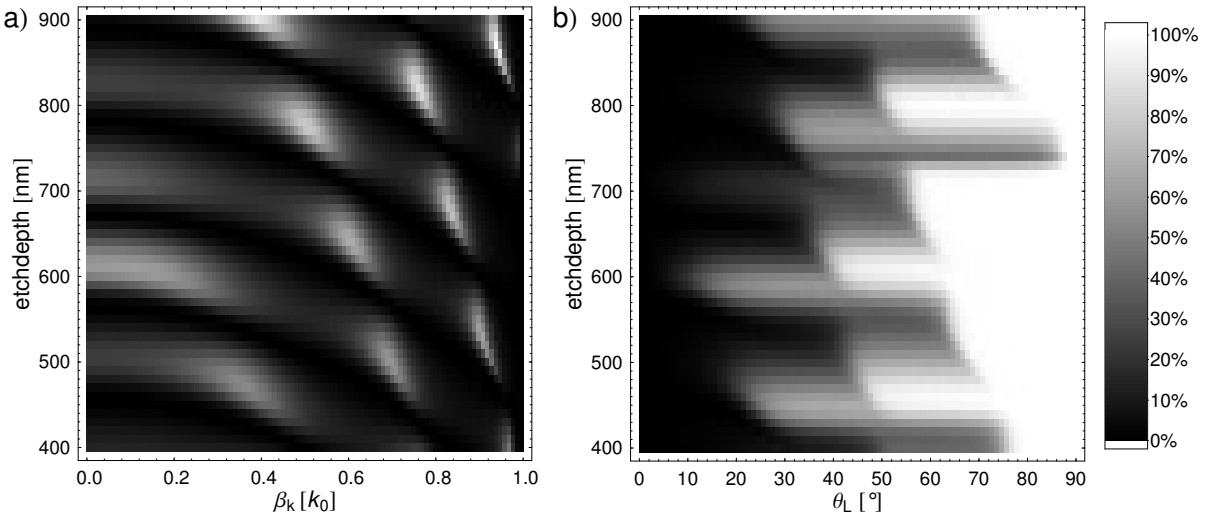

Fig. 5.32: (a) Coupling integral for different etch depths as a function of the k-vector length of the radiative modes; the guided mode has $\beta_m = 2.4k_0$ and the wavelength is 520nm. (b) Directionality resulting from diffraction of the guided mode in (a) with the coupling integral taken into account. The coupling integral drastically alters the directionality as derived from the mono-mode case.

For a direct validation, we choose the fundamental guided mode $\beta_m = 2.4k_0$ of the LED as described on page 49 but with $G_0 = 2.4k_0$ in order to observe only first order diffraction. Furthermore, the coupling integral is varied by changing the etch depth between 400nm and 900nm, see Fig. 5.32a. The directionality resulting from diffraction of this single guided mode is shown in Fig. 5.32b for $\lambda = 520$nm. By taking into account the coupling integral the directionality can significantly differ from the mono-mode case. For instance, at an etch depth of 730nm diffraction results in directionalities as low as 10% (73%) within 30° (60°). In contrast, for 590nm etch depth 60% (88%) within 30° (60°) are obtained. However, this effect varies within a few tenths of nm and therefore calls for a precise control of the layer thickness.

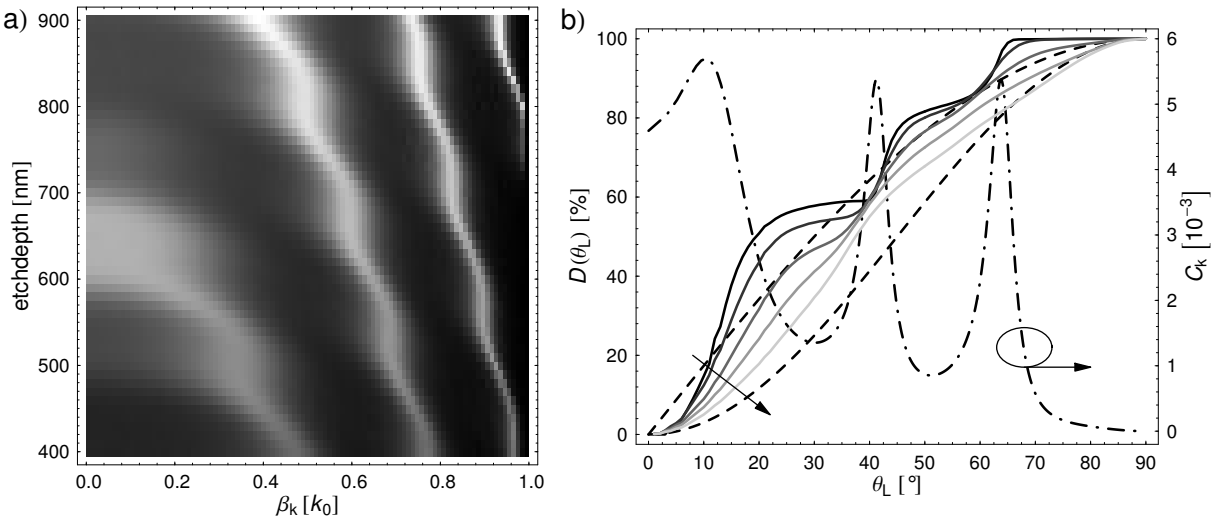

Fig. 5.33: (a) Overlap with the PhC of the radiative modes for different etch depths. The resonances determine the coupling integral. (b) Directionality for 590nm etch depth and different FWHM of the emission spectrum; the arrow indicates increasing FWHM=0nm, 5nm, 10nm, 15nm, and 30nm. The upper (lower) dashed line depicts the directionality for the mono-mode case (a Lambertian emitter). The dash-dotted line corresponding to the right y-axis shows the overlap of the radiative modes with the PhC. The resonances determine the leaps in directionality.

The sensitivity of the diffraction process on the etch depth can be related to the overlap of the radiative modes with the PhC that mainly determines the coupling integral for a given guided mode, compare Fig. 5.32a and Fig. 5.33a. As the resonances in the overlap with the PhC also depend on the wavelength, the directionalities as shown in Fig. 5.32b are hardly reached. Fig. 5.33b shows the directionality for 590nm etch depth at peak wavelength and for different FWHM of the internal emission spectrum taken into account. The steep increase in directionality coincides with the maxima of C_k. Due to the shift of these maxima with the wavelength the directionality drops for typical FWHM of 30nm to 35% (80%) within 30° (60°).

In conclusion, for a single wavelength the directionality resulting from diffraction of a guided mode can be well beyond the mono-mode case due to a proper tuning of the radiative modes' overlap with the PhC by accurately adjusting the vertical layer stack. However, as long as the contribution of these resonances can be neglected the mono-mode case still gives a practical limit for the directionality achievable from diffracting PhC LEDs. The impact of the resonances is the less the more of them exist, e.g. in sufficient thick LEDs. Besides, due to a broad emission spectrum the contribution of the individual resonances averages out. Furthermore, it should be mentioned, that the screening of the piezo-electric fields shifts the emission spectrum towards shorter wavelength in the InGaN material system. Thus, the resulting directionality is current dependent due to the varying mismatch between the emission spectrum and the cavity. The vertical layer stack has to be adjusted for a specific operational point in terms of driving current. In other material systems like AlGaInP or AlGaAs, a shift of the emission spectrum towards longer wavelength due to heating puts similar demands on the optimisation of the PhC LED.

5.3.3 Multiple Guided Modes

The basic contribution of additional guided modes to the directionality has been determined by a geometrical consideration as shown in Fig. 5.30a. However, how much light actually gets diffracted obviously relies on the diffracted intensity from each guided mode. In order to investigate this issue we come back to the usual sample structure with the overlaps given in Fig. 5.21. Analogous to the overall diffracted intensity as a function of the main reciprocal lattice vector length, see Fig. 5.22a, we calculate the directionality and the total diffracted intensity into different acceptance angles, see Fig. 5.34a. For small acceptance angles high diffracted intensity and high directionality into that angle are obtained from the same G_0. In this case, the guided modes with highest overlap product are diffracted symmetrically around the origin. The larger the acceptance angle the more shifts the optimum G_0 for diffracted intensity towards smaller values while the optimum G_0 for highest directionality stays almost constant. In the case of diffracted intensity the only criterion is to diffract as much light as possible within the desired acceptance angle. Therefore, the optimisation obeys the conclusions drawn in section 5.1 and 5.2 with a reduced target area due to the limited acceptance angle. As the guided modes best suited to diffraction have rather small eigenvalues the optimum G_0 decreases in order to take advantage of the curvature of the guided modes' circles according to Fig. 5.6. Additionally, more and more high order diffraction processes contribute to the diffraction. In contrast, high directionality is achieved when the optimum G_0 is adjusted to the guided mode region best suited for diffraction, regardless of the acceptance angle according to Fig. 5.28. Furthermore, as the ratio between the diffracted light within the acceptance angle and the overall diffracted light in air should be maximized, the diffracted intensity outside the acceptance angle should be minimized by avoiding high order diffraction processes due to Fig. 5.31. Of course, the target for the application in an étendue limited device is the overall diffracted intensity into the numerical aperture rather than a highly collimated far field at the expense of radiant flux. Thus, depending on the acceptance angle the pitch of the PhC has to be adjusted.

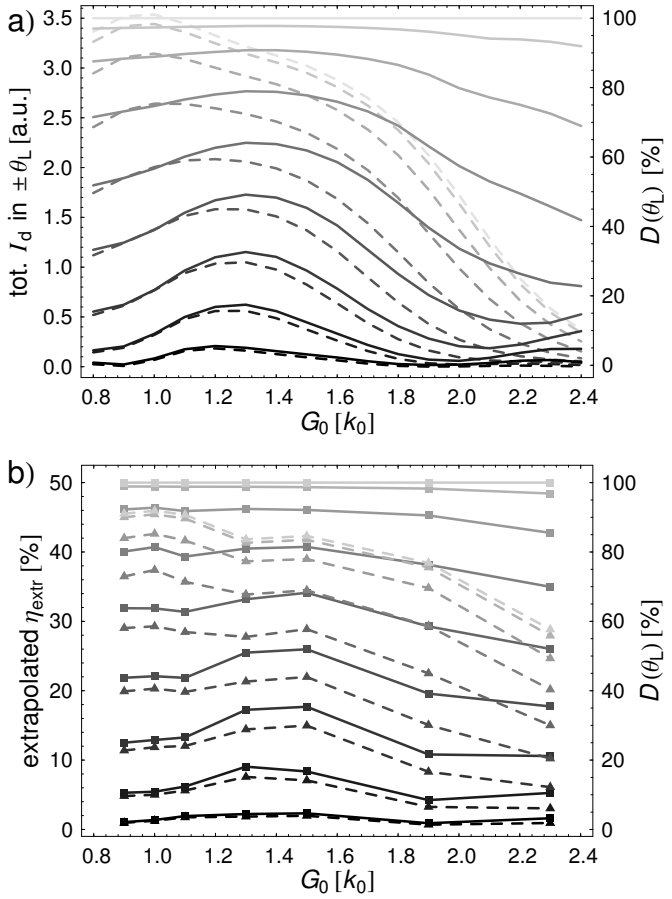

Fig. 5.34: (a) Total diffracted intensity (dashed lines, left y-axis) and directionality (solid lines, right y-axis) into different acceptance angles ranging from 10° to 90° in steps of 10° (indicated by fading black lines). A mismatch in optimum G_0 between directionality and diffracted intensity is observed due to the amount of diffracted intensity outside the desired acceptance angle. (b) Corresponding results for FDTD simulations; dashed lines indicate extrapolated extraction efficiency, solid lines directionality. The symbols indicate the various simulations.

Apart from directional far fields also the contrary is possible by diffracting guided light by PhCs. For $G_0 > 1.7 k_0$ the fraction of the emitted light between 60° and 90° is larger than the corresponding 25% of the Lambertian emitter. Flat far fields are obtained by diffracting the guided mode region with high overlap product into the vicinity of the extraction disk's edges. However, as the arc length of the diffracted modes' circles diminishes in this case, a reasonable enhancement of the extraction efficiency by diffracting PhCs is not very likely.

Within the assumptions of the diffraction model already discussed in section 5.2.2 a comparison with FDTD simulations reveals reasonable agreement also for the directionality. Additional information regarding the mismatch in directionality is given in the experimental section 5.4.1.

A comparison of the maximum directionality from Fig. 5.34a to the mono-mode case and a Lambertian emitter as a function of the acceptance angle is given in Fig. 5.35. As a large number of guided modes are diffracted into air the investigated LED has significantly worse directionality compared to the mono-mode case. However, due to the discrete diffraction behaviour of the PhC and a single guided mode region with high overlap product a reasonable enhancement compared to a Lambertian emitter can be achieved. The difference from both cases vanishes for increasing acceptance angles.

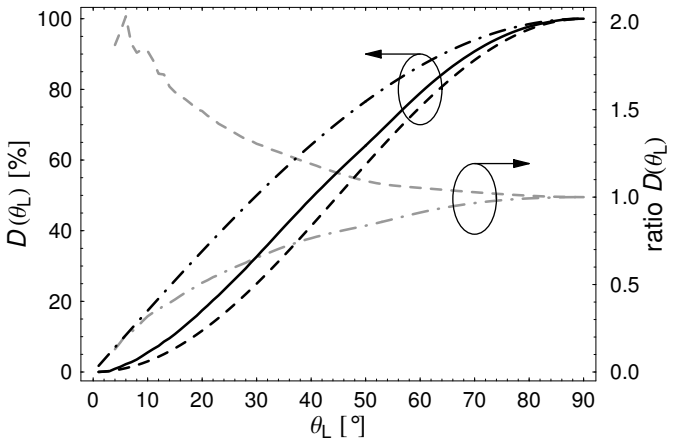

Fig. 5.35: Optimum directionality from the multimode LED in Fig. 5.34a (solid black line, left y-axis) as a function of the acceptance angle in comparison to the mono-mode case (dash-dotted black line, left y-axis) and a Lambertian emitter (dashed black line, left y-axis). The right y-axis gives the ratio between the multimode LED in relation to the mono-mode case $D(\theta_L)/D_{\mathrm{mono}}(\theta_L)$ (dash-dotted grey line) and the Lambertian $D(\theta_L)/D_{\mathrm{Lam}}(\theta_L)$ (dashed grey line).

In order to derive how important the existence of only one single guided mode region with high overlap product is, we utilize the variation of the distance between the source and the mirror of section 5.2.3. An altered spontaneous emission distribution can cause more than one guided mode region with high overlap product, see Fig. 5.24a. For better visibility Fig. 5.36 shows the overlap product calculated with κ_{m} according to (5.6) instead of C_{m} and normalized to the maximum value for each distance.

Hence, we expect a drop in directionality for distances of 110nm and 240nm due to two distinct maxima of the overlap product. The maximum directionality for each distance and acceptance angle as shown in Fig. 5.37a confirms this forecast for 240nm. From Fig. 5.37b it is evident that in this case a optimum $G_0=1.6k_0$ diffracts preferably the second maximum at $\beta_{\mathrm{m}}\approx 1.65k_0$. However, the first one at $\beta_{\mathrm{m}}\approx 1.05k_0$ is close nearby and hence decreases the directionality as it is diffracted outside the acceptance angle. In contrast, for a distance of 110nm the mode distribution favours a $G_0\approx 2k_0$ (depending on the acceptance angle) for highest directionality. Thus, the first maximum at $\beta_{\mathrm{m}}=1.05k_0$ is

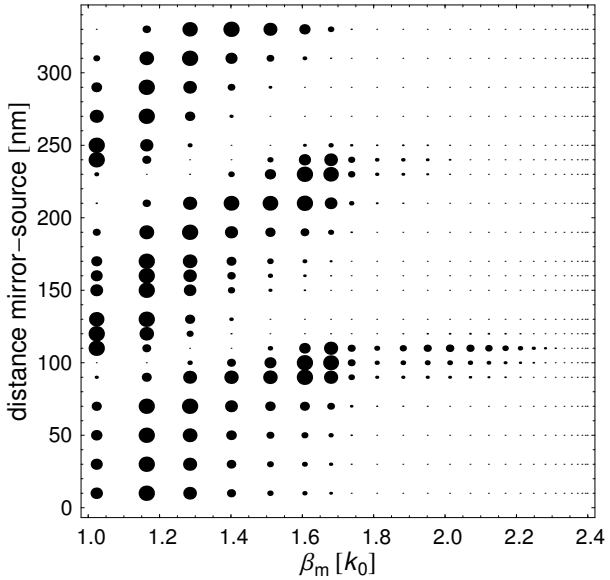

Fig. 5.36: Overlap product for increasing distance between the source and the mirror in dependence of the in-plane k-vector of the guided modes; the overlap product is calculated with κ_{m} according to (5.6) instead of the overlap C_{m} with the PhC layer. The data is normalized with the maximum for each distance.

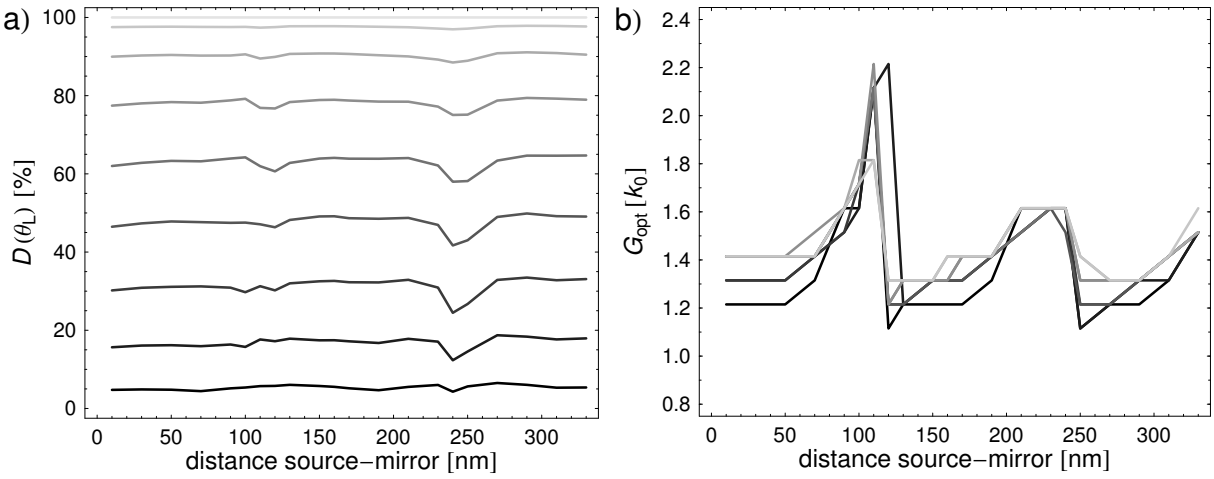

Fig. 5.37: (a) Optimum directionality within several acceptance angles (indicated by fading grey levels) within the range from 10° to 90° in steps of 10° as a function of the distance between the source and the mirror. (b) Optimum main reciprocal lattice vector length G_{opt} corresponding to the directionality shown in (a).

diffracted into the very vicinity of the extraction disk's edge and hardly shapes the far field. In any other case, the overlap product defines a single guided mode region that determines the directionality of the far field. As the resonances of the overlap with the active region get sharper with increasing distance between the source and the mirror, see Fig. 5.23, also the best suited guided mode region narrows. Consequently, a tiny increase in directionality is observed between a distance of 70 nm and 330 nm.

In conclusion, to achieve high directionality it is preferable to approximate the mono-mode case. The vertical layer stack should be designed to yield a single guided mode region with high overlap product. In this case also high diffracted intensities are obtained, see Fig. 5.24b. However, the contribution of additional guided modes decreases the directionality compared to the mono-mode case. Possible solutions are very thin stacks that support only a small number of guided modes, e.g. the structures used in [22][26][31][32]. From the extraction efficiency point of view this is preferable since the whole spontaneous emission is squeezed into a few modes that can be extracted very well. On the other hand, the wall plug efficiency has to be kept in mind.

5.3.4 Omni-Directionality and Directionality

From section 5.1.2 an in-plane omni-directional diffraction behaviour is preferable in some cases in order to diffract all in-plane propagation directions of the guided modes and hence, achieve high overall extraction efficiencies. By contrast, the omni-directionality of higher-order crystals decreases the directionality of the emission pattern as shown in Fig. 5.38 or experimentally demonstrated in [32].

Fig. 5.38 depicts the directionality within different acceptance angles from FDTD simulations for the A13 lattice and the hexagonal lattice as a function of the main reciprocal lattice vector length G_0. Almost no variation of the directionality is observed in the case of the A13, whereas the directionality from the hexagonal lattice exhibits the expected characteristics. From the geometrical point of view as sketched in Fig. 5.29a, the number of reciprocal lattice vectors with the same length cannot affect the directionality within a limited acceptance angle since every arc length appears equally often according to this number. However, if we consider the fraction of guided modes that are omni-directionally diffracted into the extraction disk by the two lattices according to Fig. 5.8b a remarkable fact arises. The higher the symmetry the larger the fraction of guided modes diffracted omni-directionally, as

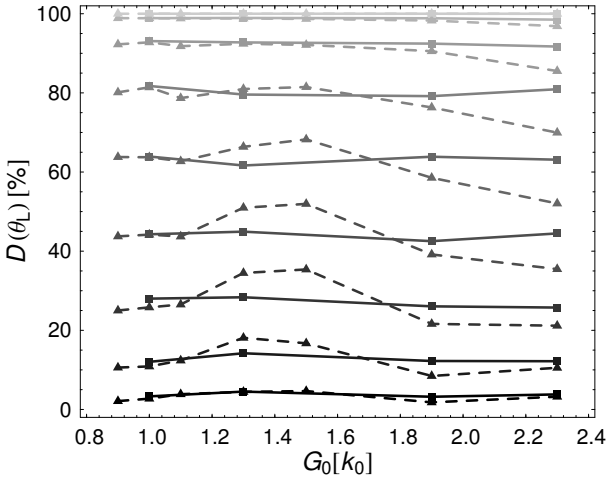

Fig. 5.38: Directionality within different acceptance angles obtained from FDTD simulations for a hexagonal (dashed line, triangles) lattice and the A13 lattice (solid lines, boxes). The fading black indicates the different acceptance angles ranging from 10° to 90° in steps of 10°. The symbols indicate the simulation results, the lines are a guide to the eye. Almost no beam-steering properties for the high-symmetry A13 lattice are observed.

already stated. Hence, with increasing omni-directionality more light is diffracted by first order processes outside the desired acceptance angle as this fraction expands almost symmetrically around G_0. This is similar to the impact of higher order diffraction processes on the directionality. Moreover, the Archimedean lattices offer more different reciprocal lattice vector lengths than the hexagonal lattice, compare Fig. 5.5 and Fig. 5.9, i.e. the Fourier spectrum is more distributed. Consequently, the diffraction processes from a guided mode are more spread over the entire extraction disk. This reduces the directionality especially in the case of weak absorption when the Fourier intensity is less important and all of these reciprocal lattice vectors contribute to the extraction of the guided modes. Therefore, the choice of the lattice relies on a trade-off between directionality and extraction efficiency.

In conclusion, the symmetry of the PhC plays an important role for the beam shaping properties of a PhC LED. From the limited variation in Fig. 5.38 it seems that better omni-directionality decreases the achievable directionality. As the extraction disk is more uniformly filled with the diffracted light from guided modes, the lower limit for the directionality in the case of high symmetry lattices is the Lambertian emission profile. The latter corresponds to constant intensity within the extraction disk.

5.4 Experimental Results and Comparison

In this section experimental results from [28] and [31] are summarized. The main challenge in fabricating PhC LEDs is the need for defining the PhC pattern with its features on a wavelength scale, i.e. hole radius of 100nm - 1000nm for the visible spectrum. Commonly used lithography techniques like contact lithography are limited to feature sizes of about 1µm by the diffraction limit or are extremely expensive, like deep-UV lithography.

On a R&D level e-beam lithography is widely used to define the PhC pattern into an appropriate resist. After the resist is developed it serves as an etching mask to transfer the pattern into the semiconductor. Even though e-beam is capable of fabricating feature sizes down to 20nm [97] along with arbitrary patterns, it is not applicable to mass production due to its extremely low throughput.

A very promising patterning technique is the nano-imprint technology [98]. It could be thought of as Gutenberg's book printing invention transferred to the nano-scale. Like in the

macroscopic world, firstly a stamp with the inverse pattern is fabricated, the so-called master. By pressure or capillary forces the pattern is printed into a resist already cast upon the LED surface. After heating and/or UV-curing the stamp is removed and the resist can act as an etching mask. The patterning process can be done on a wafer-scale and thus offers high throughput. As the master has to be fabricated first by conventional techniques, like e-beam lithography, it is less flexible compared to this method, however arbitrary patterns with feature sizes on the order of 10-20nm can be printed. The main challenge are impurities or in general topologies on the wafer surface, as the stamp can be damaged or the features are printed with insufficient quality. A possible solution to this problem are soft masters [99].

Other methods like laser-interference lithography [100] or self-organized lithography [101] are also used for fabricating PhC LEDs. However, they are limited to regular patterns, like hexagonal lattices, and require extremely sensitive experimental setups as in the case of the prior technique or suffer from a lack of long-range order and multiple layer stacking as in the case of the latter technique.

The last method in this brief summary, the selective growth of nano-rods [102][103], actually is not a patterning technique by itself. Here, the vertical layer stack is only grown on a pre-defined patterned substrate and forms nano-pillars of semiconductor material. Hence, no material has to be removed by etching and the resulting structure is inverse to structures obtained by etching. Of course, the pattern has to be defined first by a method as mentioned above. Furthermore, the goal in this research area is mainly focused on the defect-free growth of the semiconductor rather than the realization of PhC LEDs. However, PhC effects should be observed in appropriate patterns. Now, if only the vertical layer stack is grown in the usual manner such a PhC LED suffers from a loss of active area equivalently to etching through the active layer. To address this issue so-called core-shell growth has been proposed [104]. Here, the pillars consisting for instance of n-doped semiconductor are grown on the pre-defined patterned as described above. Afterwards, the whole surface of the pillars is overgrown by the pn-junction. Thus, a huge active area could be obtained that could compensate the area loss due to the selective growth.

5.4.1 Green InGaN Thin-Film LED

The investigated InGaN PhC LED was processed as a thin-film LED. Thus, its vertical layer stack is similar to Fig. 5.2 with an overall LED thickness of 6.3µm and a distance of 160nm between the active region and the Ag-based mirror. The hexagonal PhC was defined

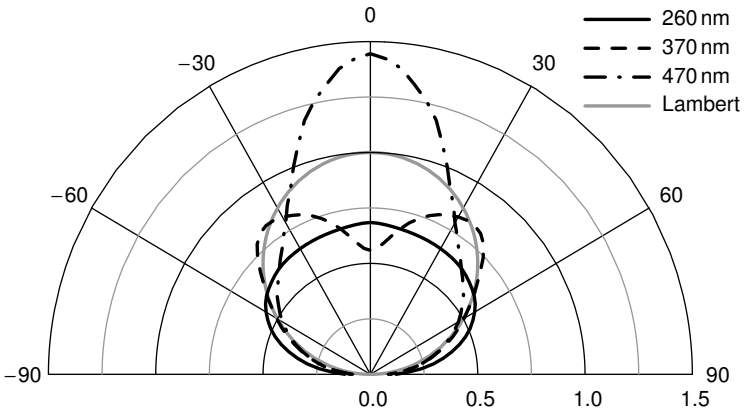

Fig. 5.39: Azimuthally and wavelength averaged far field patterns of PhC LEDs with pitch $a = 260nm$ ($G_0 = 2.3k_0$; black solid line), 370nm ($G_0 = 1.62k_0$; black dashed line), and 470nm ($G_0 = 1.28k_0$; black dash-dotted line). All patterns are normalized to 1W of radiant flux. The solid grey line indicates a Lambertian emission profile.

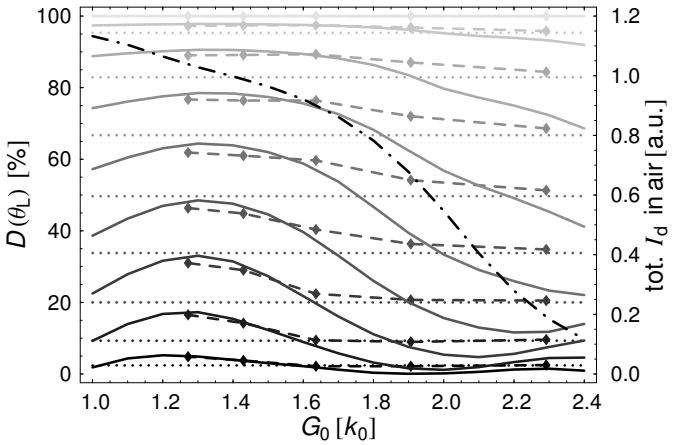

Fig. 5.40: Experimental directionality from PhC LEDs (symbols), a reference sample (dotted lines) and the diffraction model (solid lines) within different acceptance angles (indicated by fading grey levels). Additionally, the overall diffracted intensity (dash-dotted line; right y-axis) in air obtained from the diffraction model is shown.

by e-beam lithography with pitches varying from 260nm (G_0=2.3k_0) up to 470nm (G_0=1.28k_0), a filling fraction of F≈0.5 and an etch depth of ~300nm. The emission wavelength is about 520nm with a FWHM of 30nm. The 250µm x 250µm chips have been mounted on TO18 headers for characterisation.

Fig. 5.39 shows azimuthally and wavelength averaged far field patterns for three different pitches along with a Lambertian emission profile. The beam shaping properties of the PhC are clearly observed. The emission profiles are collected by an optical fibre mounted on an arm rotating around the sample in steps of $\Delta\theta$=3° and $\Delta\varphi$=10°.

Due to electrical shunts a quantitative evaluation of the PhC LEDs in comparison to the unstructured reference in terms of performance was not possible. However, an analysis of the far field patterns was performed and is shown in Fig. 5.40. Here, the experimentally obtained directionality (symbols) for the different samples is compared to calculations with the diffraction model (solid lines). Experiment as well as theory include an azimuthally and wavelength average according to the emission spectrum of the LED. In the case of high diffracted intensities to air (dash-dotted line; right y-axis) a reasonable agreement between the model and experiment is observed as the far field is mainly dominated by the diffracted light from guided modes. For decreasing diffracted intensity the experimental directionality shows an asymptotically behaviour. As the contribution from diffraction of guided modes is negligible in this case the light emitted directly from the LED, i.e. without the help of the PhC, defines the directionality. This directionality can be estimated by the corresponding value of the unstructured reference (dotted lines). As the diffraction model does not take into account the directly emitted light a poor agreement is observed. However, the diffracted intensity in air allows to qualitatively estimate the enhancement in extraction efficiency.

Fig. 5.41 shows the azimuthally averaged radiant intensity obtained from the experiment and from the diffraction model for a main reciprocal lattice vector length of G_0=1.27k_0. As the diffracted light from guided modes mainly contributes to the far field shape, an excellent agreement between the model and the experiment is achieved over the whole angle range.

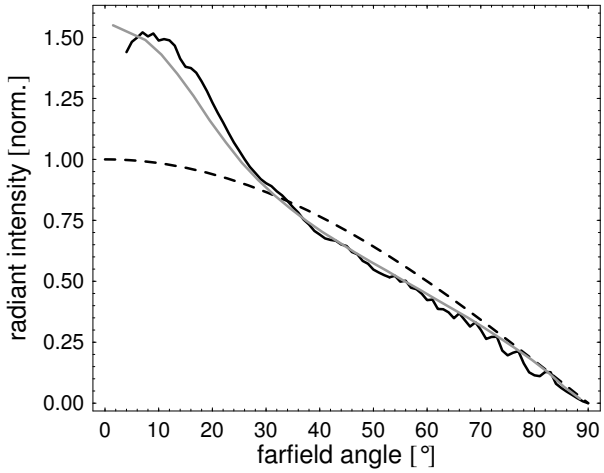

Fig. 5.41: Radiant intensity for the experimental PhC LED (grey solid line) and the diffraction model (black solid line) obtained from a PhC LED with $G_0 = 1.27k_0$. A Lambertian emission profile (black dashed line) is also shown for reference. All far fields are normalized to 1W of radiant flux.

5.4.2 Red AlGaInP LED

The AlGaInP based LED with a refractive index profile as shown in Fig. 5.42 was also processed as a 250µm x 250µm thin-film LED. Five GaInP quantum wells with $(Al_{0.5}Ga_{0.5})_{0.5}In_{0.5}P$ barriers are embedded between 400nm thick AlInP confinement layers to ensure reasonable electrical confinement. Sufficient current spreading on the n-side is obtained from a 3.8µm thick $Al_{0.6}Ga_{0.4}As$ layer and on the p-side by a Gold mirror covered with a transparent conductive oxide. The emission is centred at 658nm with a FWHM of 18nm. The hexagonal PhC was defined by e-beam lithography and was etched into the n-AlGaAs. For two etch depths of 200nm and 800nm a series of pitches ranging from 220nm ($G_0=3.4k_0$) to 450nm ($G_0=1.7k_0$) has been realized. The LEDs were mounted on TO18 headers and the overall emitted flux was measured at 10mA driving current in an integrating sphere.

The obtained radiant fluxes for the different PhC LEDs are shown in Fig. 5.43b with respect to the radiant flux of the reference sample. Enhancements of up to 1.45 are obtained for the 800nm deep PhC with $G_0=1.7k_0$. As the enhancement is due to diffraction of guided modes into the extraction disk the counterpart to the extraction enhancement in the modelling

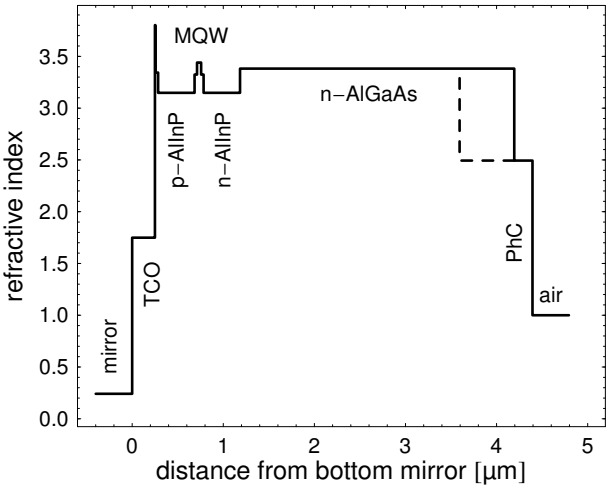

Fig. 5.42: Refractive index profile of the AlGaInP thin-film LED with 200nm deeply etched PhC. The dashed line indicates the 800nm sample.

is the overall diffracted intensity in air, see Fig. 5.43a. Since the diffraction model neglects the impact of absorption a quantitative comparison between the simulations and the experiments is not valid. However, the general dependency of the extraction efficiency on the main reciprocal lattice vector length and the etch depth is well predicted by the model.

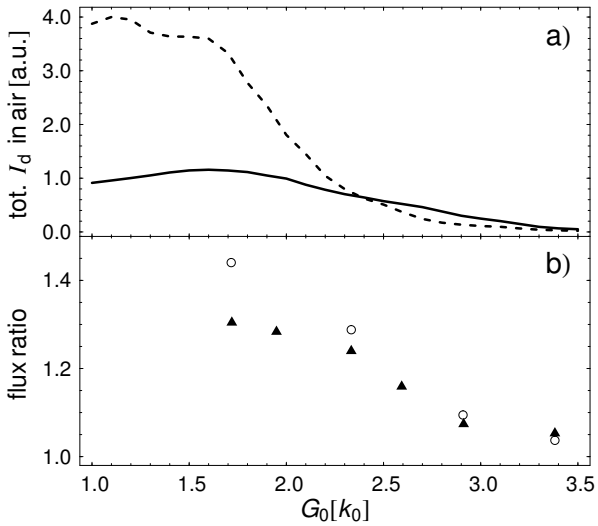

Fig. 5.43 (a) Overall diffracted intensity in air obtained from the diffraction model for the 200nm (solid line) and the 800nm (dashed line) PhC as a function of the main reciprocal lattice vector length G_0. (b) External quantum efficiency with respect to the unstructured reference for the 200nm (filled triangles) and the 800nm (open circles) deeply etched PhC.

6 Metallic PhCs: Surface Plasmon Polariton LED

In general, one could also think of structuring the bottom side of a thin-film LED before deposition of the mirror in order to place the PhC on the opposite side. However, the issue with metallic PhCs is twofold. On the one hand, they could be used in the usual manner to diffract guided light into the extraction cone [19]. On the other hand, the coupling of the active layer with so-called surface plasmons forms surface plasmon polaritons that heavily influence the internal quantum efficiency of the LED due to a very large Purcell factor [36][37]. The latter clearly has to be addressed separately from the pure diffraction process and will be discussed in this chapter.

First, the basics of surface plasmon physics is summarized and the quantities determining the light emission efficiency are pointed out. After a presentation of the FDTD simulation setup, we then use the simulation results to estimate the benefit of surface plasmon polaritons for a green InGaN LED.

6.1 Surface Plasmon Polaritons: Basics

A surface plasmon (SP) is a collective oscillation of the electron plasma at the surface of an extended metal film covered with a dielectric. If the permittivities of the two materials obey the following condition the photonic surface state forms a guided mode at the interface as depicted in Fig. 6.1 and is called a SP.

$$-\mathrm{Re}(\varepsilon_D) > \mathrm{Re}(\varepsilon_M)\,, \tag{6.1}$$

with ε_D (ε_M) the permittivity of the dielectric (metal). Hence, according to permittivity of pure silver as shown in Fig. 4.9 an interface between silver and GaN with n_{GaN}=2.4 supports SPs

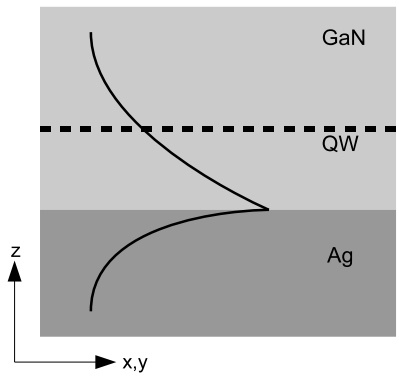

Fig. 6.1: Illustration of a surface plasmon (solid black line) confined at the interface between silver and GaN. The horizontal black line indicates a possible position of the QW in order to benefit from the coupling to the SP.

for photon energies below 2.97 eV or equivalently above a vacuum wavelength of 418 nm. Ag is the best choice for blue and green emitting InGaN based LEDs as it absorbs weakly. In the case of GaN also Aluminium could be used, but Al introduces high losses. By contrast, Gold has no sufficient negative real part of its permittivity and thus supports no SPs on GaN. However, it could be used in combination with AlGaInP or AlGaAs and the corresponding emission wavelengths. The data presented in this chapter was obtained from the silver data as given in section 4.3.6 but without the extra factor for the collision frequency ν_c.

Due to the confinement of the SP at the interface, its in-plane k-vector length β_{SP} is larger than the k-vector in GaN $\beta_{SP} > n_{GaN} k_0$. This fact is also reflected by the dispersion relation of the SP as shown in the left part of Fig. 6.2 because it is located right from the light line of GaN for photon energies below 2.97 eV. The corresponding attenuation of the mode profile as given in the middle of Fig. 6.2 indicates that the SP is squeezed within a very narrow volume. The resulting high electric field amplitudes increase the spontaneous emission rate significantly according to Fermi's Golden Rule (2.3) if the emitting layer is situated at the high local electric field amplitude, see e.g. Fig. 6.1. The additional contribution of the huge density of photonic states due to the flat characteristics of the dispersion relation results in extremely high Purcell factors; right part of Fig. 6.2. Therefore, high internal quantum efficiencies could be obtained by placing an emitter into the vicinity of the interface. The coupling of the photons with the SP forms the surface plasmon polariton (SPP). As the surface plasmon is a longitudinal surface wave only the TM-polarized part of the light emission couples to it. The distance between the emitter and the metal should be less than the attenuation length of the SP into the dielectric. In the case of Ag on GaN the attenuation length is ~30 nm at 520 nm. On the other hand, the confinement also causes very short propagation length L_{SP} of the SP due to the absorption in the metal; right part of Fig. 6.2. Consequently, a highly absorbing adhesion layer between GaN and Ag would dramatically reduce the propagation length. Therefore, the data for pure silver was used instead of the data obtained from the higher collision frequency.

However, the question arises how the light guided within the SP can be extracted and converted into "useful" light propagating in GaN before it is absorbed. Here, a periodic

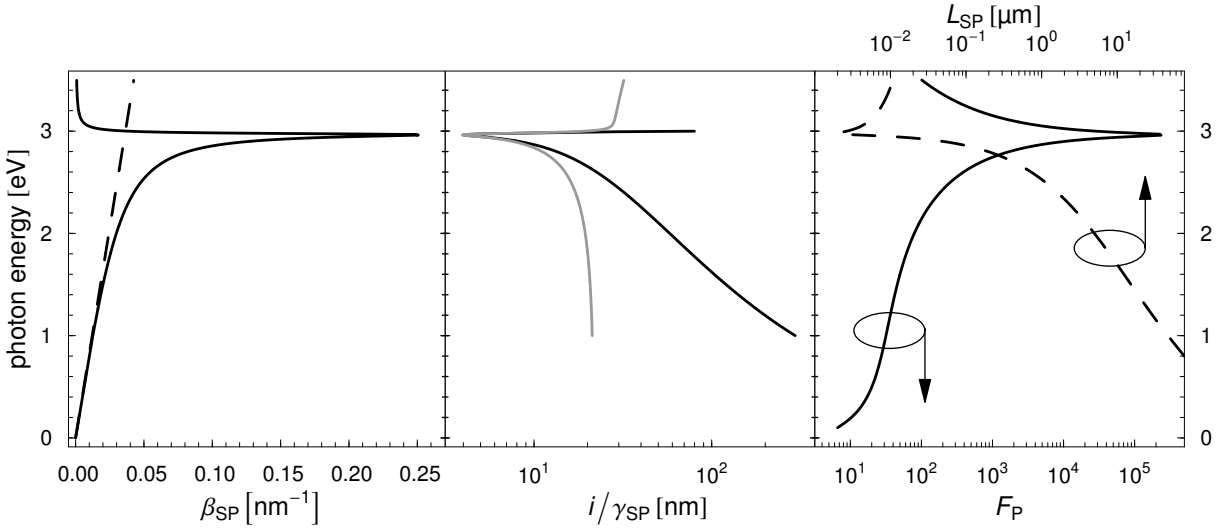

Fig. 6.2 (left) Dispersion relation of a surface plasmon (solid line) at the GaN-Ag interface; the refractive index of GaN is kept constant at $n_{GaN} = 2.4$, the permittivity of Ag is taken from the fit as shown in Fig. 4.9. The dashed line indicates the light line of GaN. (middle) Attenuation length of the mode profile into GaN (black line) and Ag (grey line) with γ_{SP} according to (4.5). (right) Purcell factor (solid line) of a horizontal dipole placed at the position of the interface. The dashed line (upper x-axis) shows the propagation distance L_{SP} of the SP.

structuring offers a solution as it folds the dispersion relation above the light line. The extraction of light depends on the interplay between the absorption length and the extraction length due to the grating. Thus, apart from the boost in internal quantum efficiency due to the high Purcell factor also the re-extraction of light from the SP has to be taken into account when considering the efficiency of a SPP coupled LED [42]. The effective internal quantum efficiency can be written as

$$\eta_{\mathrm{eff}} = \eta_{\mathrm{rad}} \underbrace{\frac{F_{\mathrm{P}} \Lambda_{\mathrm{rad}}}{F_{\mathrm{P}} \Lambda_{\mathrm{rad}} + \Lambda_{\mathrm{nrad}}}}_{\eta_{\mathrm{IQE}}}, \tag{6.2}$$

according to (2.2) and (2.4). The efficiency η_{rad} takes into account the extraction efficiency from the SP and the part of light that is generated without the help of the SP, i.e. light generation into guided, $k_0 < \beta_{\mathrm{m}} < k_{\mathrm{GaN}}$, and radiative modes, $\beta_{\mathrm{m}} < k_0$. In conclusion, the extraction of light from the SP is the decisive quantity no matter how high the Purcell factor is [42].

6.2 FDTD Simulation Setup

In order to quantify the effect of SP coupled emitters we utilized FDTD simulations that yield the important quantities, namely the Purcell factor F_{P} and the radiative efficiency η_{rad}. The simulation was setup as shown in Fig. 6.3. Only the GaN-Ag interface is taken into account. The GaN-to-air interface was not included, as we wanted to focus on the coupling process. Since the coupling of the emitter to the SP depends on its relative position to the grating four positions of the horizontal dipole are used for spatial averaging, see Fig. 6.3b. The emission of the source included wavelengths ranging from 480nm up to 560nm. The 2µm x 2µm x 0.5µm large simulation area was surrounded by PMLs. The Purcell factor and the radiative efficiency are calculated according to

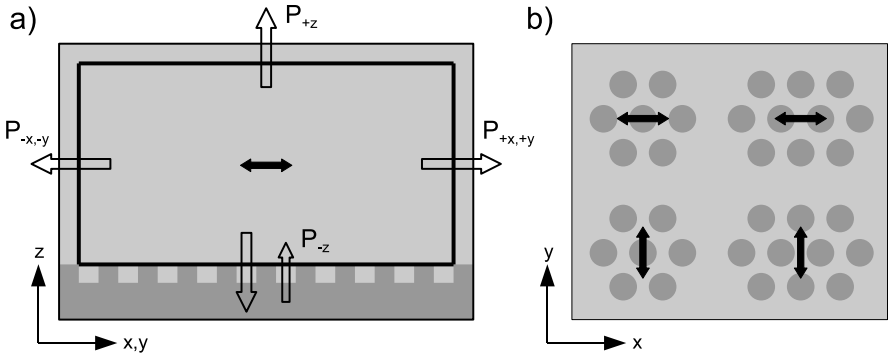

Fig. 6.3 (a) Sketch of the simulation setup used for calculating the Purcell factor and the radiative efficiency. The horizontal dipole source was placed within the GaN layer (light grey area) in increasing distances away from the structured mirror (dark grey area). The thick black lines indicate the planes for monitoring the power flux leaving the simulation volume into the PMLs. (b) Illustration of the four positions of the dipole relative to the hexagonal grating taken into account for spatial averaging. For each position a simulation was performed.

$$F_{\mathrm{P}} = \frac{P_{+\mathrm{x}} + P_{-\mathrm{x}} + P_{+\mathrm{y}} + P_{-\mathrm{y}} + P_{+\mathrm{z}} + P_{-\mathrm{z}}}{P_{\mathrm{tot},0}}$$
$$\eta_{\mathrm{rad}} = \frac{P_{+\mathrm{x}} + P_{-\mathrm{x}} + P_{+\mathrm{y}} + P_{-\mathrm{y}} + P_{+\mathrm{z}}}{P_{+\mathrm{x}} + P_{-\mathrm{x}} + P_{+\mathrm{y}} + P_{-\mathrm{y}} + P_{+\mathrm{z}} + P_{-\mathrm{z}}}, \tag{6.3}$$

with $P_{\pm \mathrm{x,y,z}}$ the Poynting flux in $\pm x$-direction, $\pm y$-direction, and $\pm z$-direction, respectively, and $P_{\mathrm{tot},0}$ the overall emitted flux from a dipole in a homogeneous optical environement. For the hexagonal PhC we used a primitive reciprocal lattice vector length according to the in-plane k-vector length of the SP, i.e. $G_0=\beta_{\mathrm{SP}}=3.47k_0$ at peak wavelength of 520nm or equivalently a pitch of $a=173$nm. The filling fraction is $F=0.5$ and the etch depth is 40nm to ensure a large overlap of the SP mode with the PhC.

In Fig. 6.4 the Purcell factor and the radiative efficiency obtained from FDTD simulations are compared to the results from the transfer matrix algorithm described in 4.1 for the unstructured reference and varying distance between the dipole and the mirror. All the calculations contain a Gaussian wavelength average according to a peak wavelength of 520nm with a FWHM of 30nm. The agreement between the two methods is good; the slight discrepancies are caused by an insufficient spatial resolution of the FDTD grid. However, a further improvement in this regard would have resulted in very long simulation runs especially in the cases of the structured mirror. The latter requires a very dense computational mesh in lateral direction; much denser compared to the PhC LED computations of the foregoing sections.

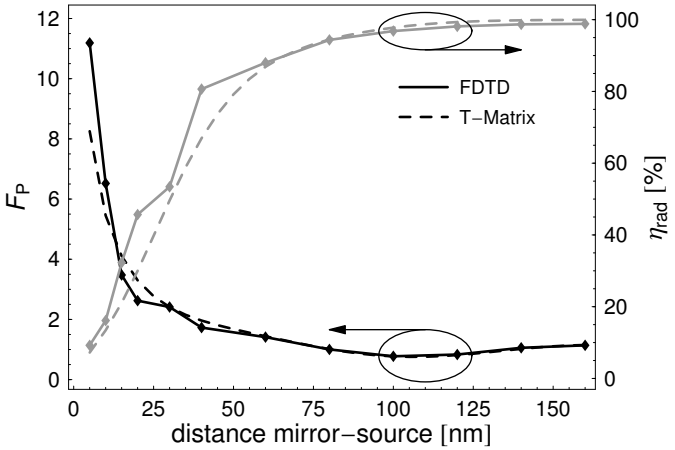

Fig. 6.4: Purcell factor F_{P} (black lines) and radiative efficiency (grey lines) from FDTD simulations (solid line with symbols) and the transfer matrix algorithm (T-Matrix) given in 4.1 (dashed lines) as a function of the distance between the source and the mirror.

6.3 Green InGaN SPP LED

According to the evanescent nature of the SP, it is evident that the coupling of the emitter depends on the distance between the source and the mirror as the electric field amplitude of the surface plasmon decays exponentially inside the GaN layer. The resulting drop in F_{P} is well reflected by the FDTD simulations in both cases, the unstructured reference and the structured mirror, see Fig. 6.5. As soon as the dipole does not couple to the SP anymore, oscillations of the Purcell factor owing to the interference of the source with its mirror image

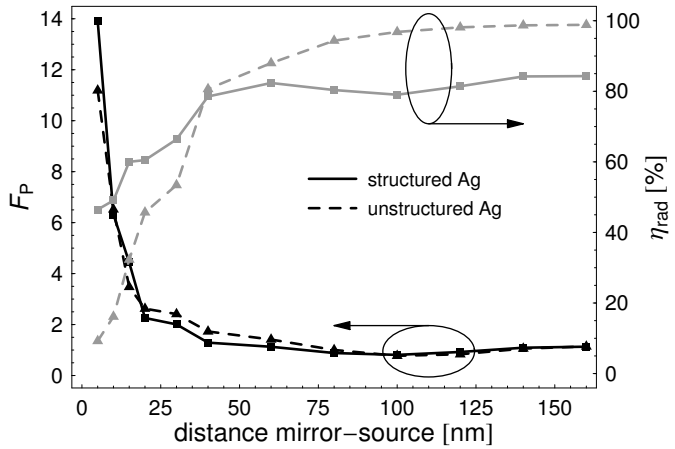

Fig. 6.5: Purcell factor F_P (black lines) and radiative efficiency (grey lines) from FDTD simulations for the SPP LED (solid line with boxes) and the unstructured mirror (dashed lines with triangles) as a function of the distance between the source and the mirror. Due to the structuring the light generated into the SP with high F_P can partially be extracted. However, the radiative efficiency at large distances is worse and thus, the mirror reflectivity is reduced compared to the pure unstructured silver mirror.

are observed. The radiative efficiency at small distances for the reference calculation is very low, as most of the light is emitted directly into the SP and gets absorbed by the metal. The less the impact of the SP the higher becomes the radiative efficiency. In contrast, the PhC extracts light from the SP partially and enables usage of the high Purcell factor. However, at large distances the structured mirror absorbs some of the emitted light due to the coupling to the SP by the grating. Thus, the structuring reduces the reflectivity of the mirror.

In order to estimate the benefit from SPP LEDs for the effective internal quantum efficiency, Fig. 6.6a shows η_{eff} as a function of the ratio between non-radiative and radiative recombination rates according to (6.2) for a standard unstructured InGaN LED with 160nm distance and a SPP LED with structuring and a distance of 10nm. The high Purcell factor of the SPP LED weakens the impact of the non-radiative processes on the internal quantum efficiency compared to the unstructured reference. From the crossing point between the two

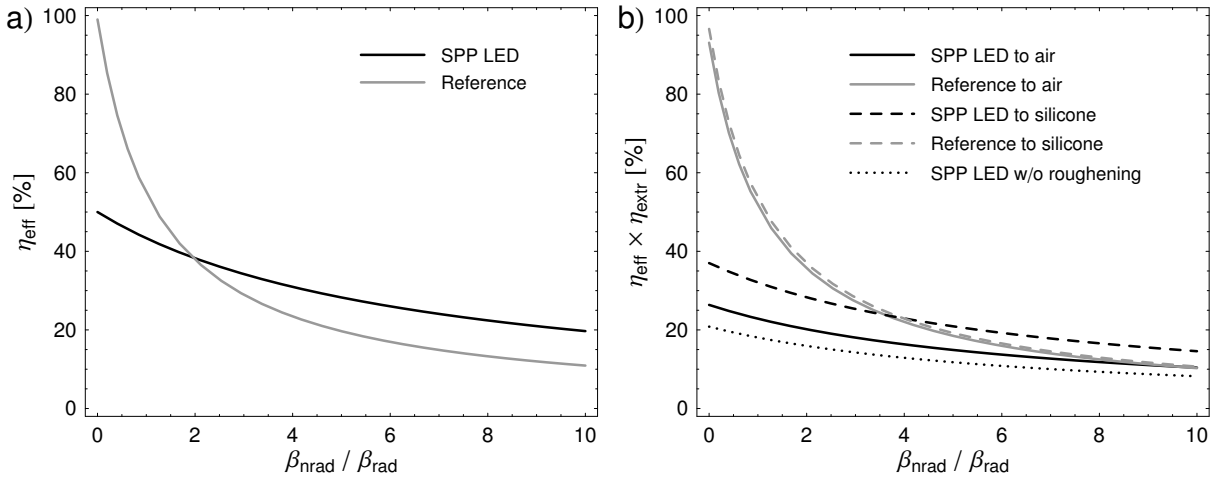

Fig. 6.6: (a) Effective internal quantum efficiency according to (6.2) for the SPP LED (black line) with 10nm distance between the source and the mirror and the reference LED (grey line) with 160nm. Owing to the moderate radiative efficiency the higher Purcell factor enhances the effective efficiency only for high non-radiative rates. (b) Calculations according to (a) with the extraction to air (solid lines) and silicone (dashed lines) taken into account. The benefit from the use of SPP coupled LEDs is limited to poor emitters or cases that are less dependent on the mirror reflectivity. The dotted line shows the results for a SPP LED without surface roughening.

graphs the efficiency of extracting light from the SP can be estimated to be 38%. Due to the low radiative efficiency a significant improvement is obtained only in the case of poor emitters, i.e. high non-radiative rates. The latter has already been derived by [42] based on a perturbational treatment of the coupling and could be quantified by these simulations.

However, the light still propagates inside the LED and has to be extracted to the ambient medium. The extraction from a SPP LED with a bare semiconductor-to-air interface can be estimated from the same geometrical construction as has been utilized for the mono-mode case, see Fig. 5.27. The diffraction of the SP is an excellent approximation to the mono-mode case as almost all the light is emitted into a single mode with a given in-plane k-vector length. Therefore, the extraction efficiency is approximately $1/2.4 \approx 42\%$. However, a comparison with a thin-film LED with rough surface but unstructured mirror limits the applicability of SPP LEDs to even less efficient emitters compared to the effective efficiency due to the lower extraction efficiency, see Fig. 6.6b. The incorporation of the SPP LED into a thin-film LED is advantageous but the reduced reflectivity of the structured mirror limits the extraction efficiency of this LED. The extraction efficiencies for the thin-film LEDs with rough surface are taken from Fig. 2.8. The structured mirror device has an extraction efficiency to air (silicone) of 53% (74%), whereas the unstructured reference achieves 94% (97%) in the case of a pure silver mirror without enhanced collision frequency. To calculate these extraction efficiencies we used the radiative efficiency at a distance of 160nm in both cases as an upper estimate for the mirror reflectivity. Realistically, the mirror reflectivity should only be calculated from the light emitted towards the mirror. The radiative efficiency instead contains both the upward and downward emitted light, where the prior does not experience absorption at the mirror. This partially explains the extremely high extraction efficiency to air for the unstructured reference of 94%. But also the Ag-data assume a very pure Ag that is hardly achieved in reality. As the mirror reflectivity is less important in the case of extraction to silicone or in the case of absorption within the semiconductor the use of SPPs could be more beneficial in these cases.

With the high directionality of the mono-mode case in mind, the SPP LED with bare semiconductor-to-air interface could also be a proper choice for étendue limited applications. A comparison of the effective external quantum efficiency into different acceptance angles is depicted in Fig. 6.7 for the bare SPP LED and a roughened thin-film LED without structured

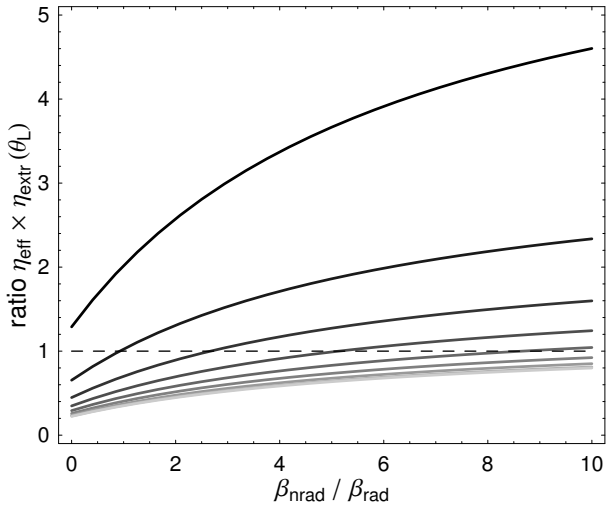

Fig. 6.7 Ratio of the effective external quantum efficiency of the bare SPP LED and the standard roughened thin-film LED taken from Fig. 6.6b into different acceptance angles. The decisive factor is the ratio in directionality between the mono-mode case and the Lambertian emitter, 1/sin(θ). The horizontal dashed line indicates the value of break-even.

mirror. However, the bare SPP LED has only superior performance within very narrow acceptance angles. The larger the acceptance angle the higher non-radiative rates are required for a break-even.

6.4 Conclusions on SPP LEDs

As already concluded in [42] the FDTD simulations also reveal that the applicability of SP coupled emitters is limited to low internal quantum efficiencies. On the one hand, the high Purcell factors weaken the impact of the non-radiative processes. On the other hand, the effective internal quantum efficiency is restricted by the poor re-extraction of light from the SPs due to the absorption inside the metal. This tendency to poor emitters is even stronger, if the incorporation of the structured mirror into a thin-film LED is taken into account. The reduced mirror reflectivity inhibits efficient light extraction to the ambient medium from a roughened LED as the redistributed light is more prone to absorption. If the mirror reflectivity has less impact on the extraction efficiency, e.g. for high bulk absorption or extraction to silicone, a structured mirror implies less penalties. A similar effect is found for the application of a SPP LED without roughening if the higher directionality is taken into account. However, the main disadvantage of a SPP LED, the absorption of the metal, still remains in any case. A possible workaround could be to insert a thin low-refractive index material between GaN and Ag in order to pull the mode out of the mirror and consequently reduce the absorption. However, as the confinement of the SP is reduced, the Purcell factor decreases simultaneously. Thus, it is questionable, whether a positive net effect is achieved. Another possibility is to replace the holes filled with Ag by holes filled with a non-absorbing dielectric with low-refractive index, e.g. air. The low average refractive index of the PhC reduces the absorption losses of the SP.

Based upon these results it is also possible to estimate the applicability of a metallic PhC for diffracting guided light from the semiconductor to air. From the diffraction point of view the metallic PhC should perform equally to a PhC at the semiconductor-to-air interface. However, the reduced mirror reflectivity will inhibit effective redistribution of light. Thus, a PhC that allows coupling between guided modes and SPs will have less extraction efficiency in any case compared to a PhC that allows no coupling. In the case of a PhC at the semiconductor-to-air interface this coupling is hardly possible as the coupling integral between guided modes and SPs vanishes due to the short attenuation length of the SP inside the semiconductor.

7 Comparison of PhC LEDs and Roughened LEDs

In this chapter we focus on the fundamental question: Is a PhC LED as efficient as a roughened thin-film LED? And furthermore, how much enhancement could we expect for étendue limited applications? For this purpose we compare results obtained from FDTD simulations for the usual structure as mentioned at the beginning of chapter 5 with a thin-film LED with a rough surface as shown in Fig. 2.7. Thereafter, we present an optimised PhC LED and expand our investigations by taking into account the radiation pattern of the LEDs.

7.1 Extraction Efficiency

Before we study the FDTD results, we utilize the photonic strength model in order to derive the difference between a random surface structure and a PhC.

7.1.1 Estimations from the Photonic Strength

Fig. 7.1a shows an approximation of a random surface structure with 924 randomly

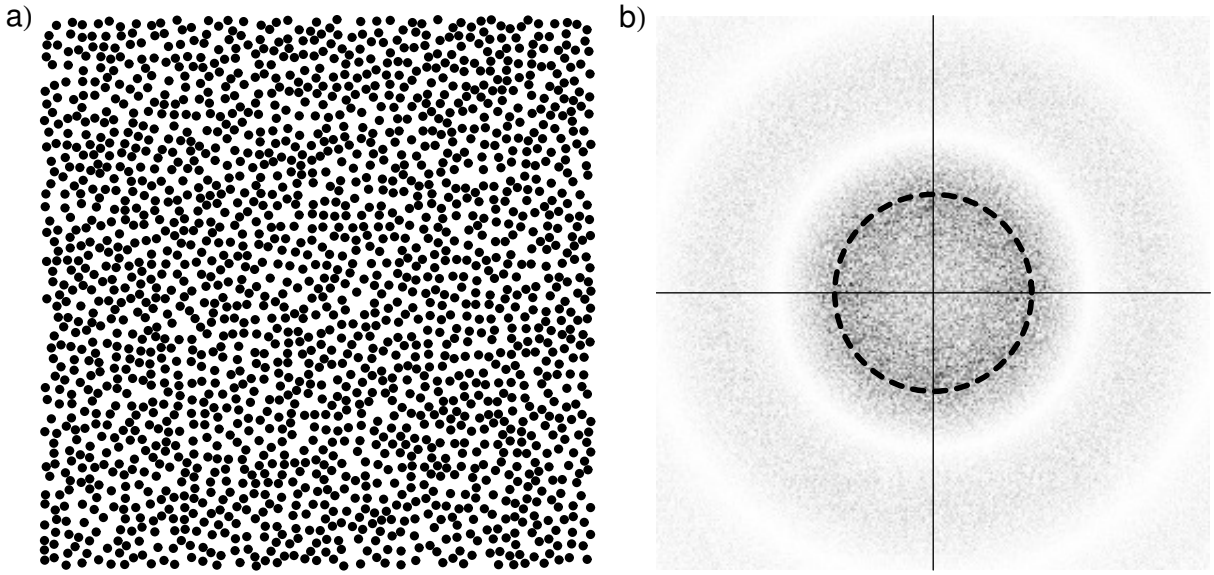

Fig. 7.1: Illustration of the rough surface (a) and its Fourier spectrum (b) used for comparison with a hexagonal lattice. The area for the Fourier transformation is $1600a^2$, with a the pitch of the reference hexagonal lattice which the number of distributed holes is derived from. The filling fraction was chosen $F = 0.4$. The dashed circle indicates the main reciprocal lattice vector length associated with this surface structure and corresponds to the primitive reciprocal lattice vector length of the reference hexagonal lattice.

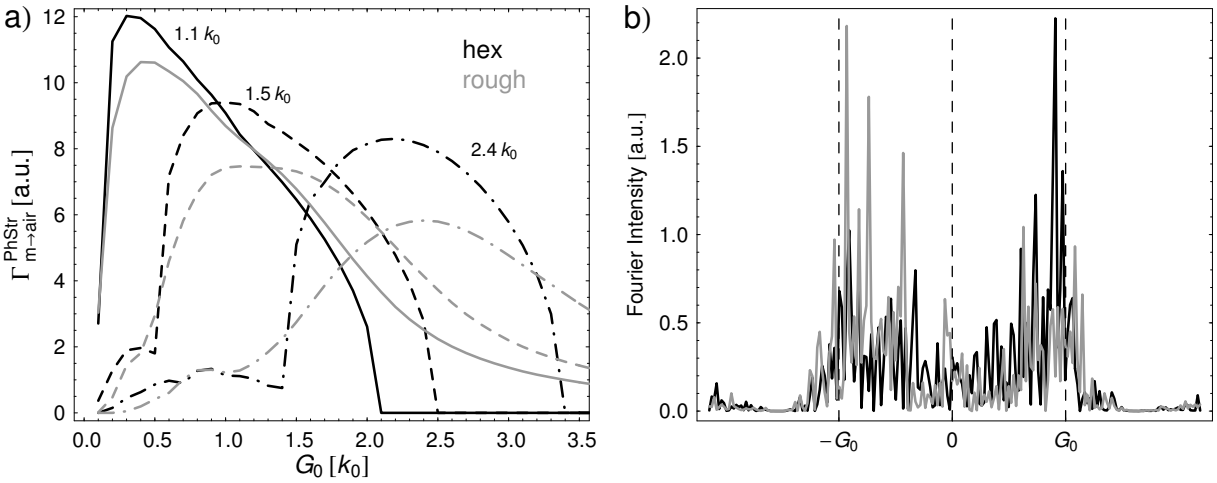

Fig. 7.2 (a) Diffraction coefficient obtained from the photonic strength model (5.2) for the hexagonal lattice (black lines) and the rough surface (grey lines) and guided modes with $\beta_m = 1.1\,k_0$ (solid line), $\beta_m = 1.5\,k_0$ (dashed line), and $\beta_m = 2.4\,k_0$ (dash-dotted line). Owing to the smooth distribution of the Fourier spectrum the rough surface has smaller diffraction coefficients than the hexagonal lattice but is less sensitive on the in-plane k-vector and offers omni directional diffraction for every guided mode. (b) Vertical (black) and horizontal (grey) slice through the Fourier spectrum for the rough surface as shown in Fig. 7.1b. The dependency of the diffraction coefficient on G_0 results from the high Fourier intensities around G_0.

positioned holes. The number of holes is equal to the number of holes that a hexagonal lattice offers within the same area. Therefore, the Fourier transform as shown in Fig. 7.1b has the same overall "content" as the hexagonal lattice and can be compared to the corresponding Fourier spectrum of a hexagonal lattice. The filling fraction is F=0.4, the pitch of the reference hexagonal lattice is a and the area used for the calculation of the Fourier transform is $40\text{x}40a^2$. Clearly, no discrete features are observed in the Fourier spectrum but an even distribution over a disk slightly larger than G_0.

The washed out Fourier spectrum results in a diffraction coefficient – obtained from the photonic strength model (5.2) – that is less sensitive to the exact value of the main reciprocal lattice vector compared to a hexagonal lattice, see Fig. 7.2a. This is of great advantage for thick LEDs supporting many guided modes and especially in the case of AlGaAs or AlGaInP-based LEDs. In these cases the guided modes are spread over a larger range of in-plane k-vectors owing to the refractive index at the corresponding emission wavelength of n_{SC}=3.5. However, the maximum values of the diffraction coefficient are lower compared to the hexagonal lattice and therefore, less intensity is diffracted per unit length into air from a single mode. The same tendency has also been observed in the case of Archimedean lattices, Fig. 5.10. Therefore, the rough surface is expected to be less efficient compared to a hexagonal lattice with the same main reciprocal lattice vector length in the case of strongly absorbing structures. But the rough surface offers omni-directional diffraction similar to the Archimedean lattices and hence, it should be more efficient in the case of less absorbing structures. In contrast to Archimedean lattices with their discrete Fourier spectrum the rough surface supports a huge number of reciprocal lattice vectors with the same length $|\mathbf{G}|=G$ for almost every G. According to Fig. 5.8b the omni-directionality of the Archimedean lattice is restricted at a given G by the twelve main reciprocal lattice vectors to a narrower range of guided modes compared to the rough surface that diffracts almost all the guided modes within the range $G\pm k_0$. Consequently, no far field shaping effect is expected from a rough surface. In summary, the rough surface diffracts every in-plane propagation direction of every guided mode to air, whereas the PhCs with their discrete Fourier spectrum always leave some parts of guided modes un-extracted. These parts may only be recovered by prior redistribution of the light into extractable guided modes. The dependency of the diffraction coefficient for the rough surface on G_0 is due to the crowding of high Fourier intensities

around G_0 as can be seen in Fig. 7.2b. Even though randomly positioned, the average distance between neighbouring holes causes this Fourier spectrum.

7.1.2 FDTD: PhC LED vs. Rough LED

For a quantitative comparison we now resort to FDTD simulations. The LED structure has a 3µm thick GaN layer with a bottom Ag-based mirror and the active region located 160nm away from the mirror. In terms of extraction efficiency this configuration has been proven to be very efficient in section 5.2.3. The PhC is 300nm deep with a filling fraction of F=0.5 and a main reciprocal lattice vector of $G_0=k_0$. For a realistic representation of the roughening of GaN-based thin-film LEDs as shown in Fig. 2.7c within FDTD randomly positioned pyramids along the surface of the LED are incorporated instead of the PhC. The etch depth of each pyramid is also chosen randomly up to a maximum of 1µm. The density of the pyramids was adjusted to avoid areas on the LED surface without pyramids. The angle of their sidewalls with respect to their base is 60°. In real LED chips this angle is obtained for GaN grown along the *c*-axis as the etching during the processing uncovers the {10-1-1} facets of the GaN crystal [105]. The only difference to real roughened surfaces is the base of the pyramids that is quadratic within the simulations instead of hexagonal. The results include a Gaussian average with a peak wavelength of 520nm and a FWHM of 30nm taken from data ranging from 470nm up to 570nm with 71 supporting wavelengths.

The extraction efficiency given in Fig. 7.3 for both cases firstly reveals a superior performance of the roughened thin-film LED compared to the PhC LED. The prior (latter) is roughly 3.7 (2.8) times more efficient than the unstructured reference. However, a closer look at the extraction efficiency for integration radii <5µm exhibits a higher extraction obtained from the PhC LED compared to the rough LED. The PhC extracts the guided modes with high overlap product very fast due to its high diffraction coefficient. The remaining modes are extracted less efficiently as the discrete Fourier spectrum offers no reciprocal lattice vectors. In contrast, the rough surface extracts all guided modes omni-directionally. Thus, simply replacing the standard structuring with a PhC will hardly result in more efficient LEDs. According to the etch depth variation of the PhC LED as shown in Fig. 5.20a almost no benefit arises for the PhC LED from etching the PhC down to etch depths of the pyramids.

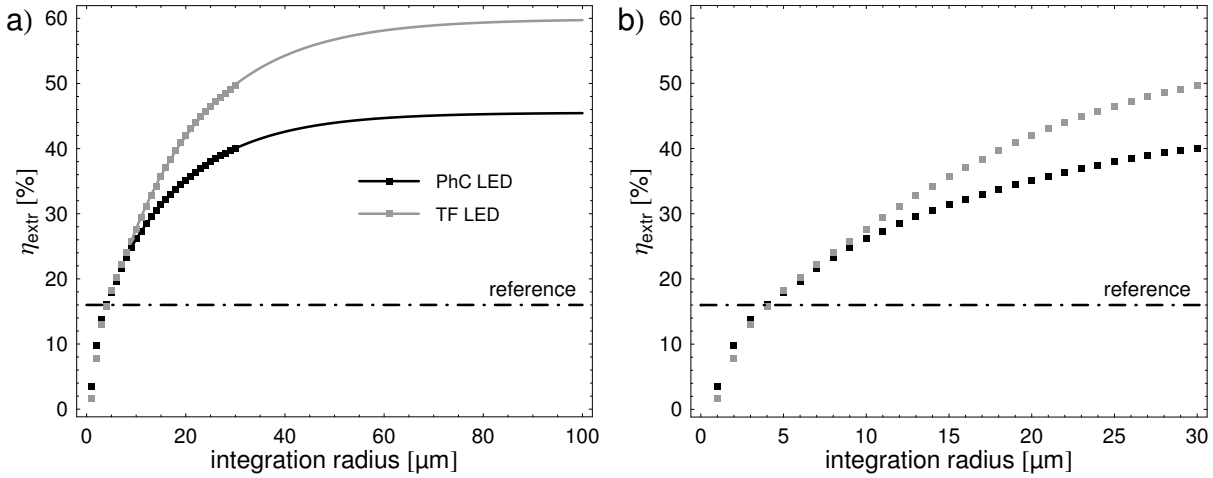

Fig. 7.3: Extraction efficiency obtained from the FDTD simulations for a PhC LED (black line and symbols) and for a roughened thin-film LED (grey line and symbols). The dash-dotted horizontal line depicts the extraction efficiency of the unstructured reference sample. (b) is a close-up to the data from (a) on the values obtained from the simulations. Even though the PhC extracts light initially efficiently it cannot compete with the omni-directional diffraction properties of the random surface.

7.1.3 Optimised PhC LED

Even though the PhC LED of the previous section is optimised regarding the PhC pattern in combination with the guided mode structure, the vertical layer stack can be improved. The main issue is to reduce the overall thickness of the LED in order to get rid of the high number of guided modes, see Fig. 5.20b. From the reduced thickness ensues an increased interaction of the guided modes with the PhC, on the one hand. On the other hand, the absorption increases simultaneously according to the t^{-3}-dependency. In order to enhance the extraction efficiency, a low-refractive index layer is inserted into the vertical layer stack between the GaN and the mirror. We use SiO_2 for this layer as its refractive index is n=1.5, it is transparent and can easily be processed. Fig. 7.4 shows the refractive index layer structure.

According to the thin overall thickness the stack supports only 14 guided modes. The resulting overlap with the active region B_m and the PhC layer C_m are shown in Fig. 7.5 at peak wavelength. As we deal with a very shallow etched PhC the overlap C_m is a very reasonable measure for the coupling integral. From the overlap product an optimum main reciprocal lattice vector length of $G_0=1.5k_0$ would be most preferable. However, if the absorption of the guided modes is additionally taken into account, see Fig. 7.6, a $G_0=k_0$ should be chosen in order to extract the most absorbed guided modes first. The remaining modes are extracted anyway by high-order processes that also offer in-plane omni-directionality as their aborption coefficient is at least almost two orders of magnitude smaller. The TM-polarized guided mode at $\beta_m=1.68k_0$ which does not have appreciable overlap neither with the active layer nor with the PhC but has high absorption is a surface plasmon mode guided at the SiO_2-Ag interface. The vertical layer stack was primarily designed in regards of the radiative modes. In order to obtain only one dominating resonance of the radiative modes within the extraction disk a thickness in the micro cavity regime is chosen, i.e. the cavity formed by the mirror and the semiconductor-to-air interface is $\sim 4\lambda_{peak}$ thick. The position of the active region ensures high extraction of light within a limited acceptance angle of 30°. Calculations with the transfer matrix algorithm of section 4.1 including a Gaussian wavelength average reveal roughly 51% of directionality within 30°. Hence, the directly emitted light forms a very directional background. The overlap of radiative modes with $\beta_m<0.5k_0$ with the PhC layer results in preferred diffraction into the targeted acceptance angle of 30°. The fairly shallow etched PhC with a filling fraction of F=0.5 ensures on the one hand to stay within the weakly coupled regime. On the other hand, it is still thick enough to cover the largest attenuation length of ~96nm within the PhC for the TM-polarized guided mode with $\beta_m=2.03k_0$.

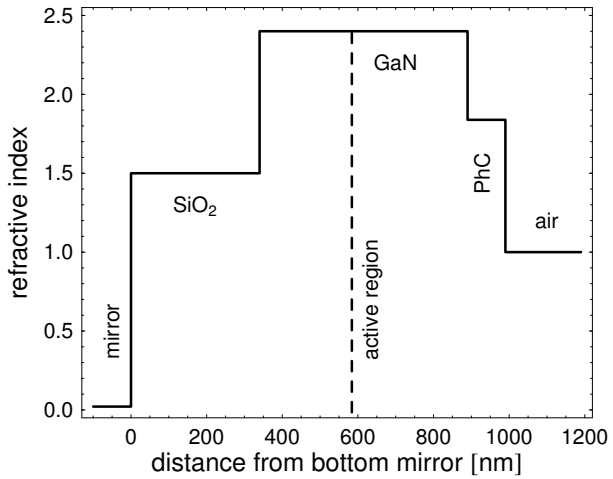

Fig. 7.4: Refractive index profile of the optimised PhC LED.

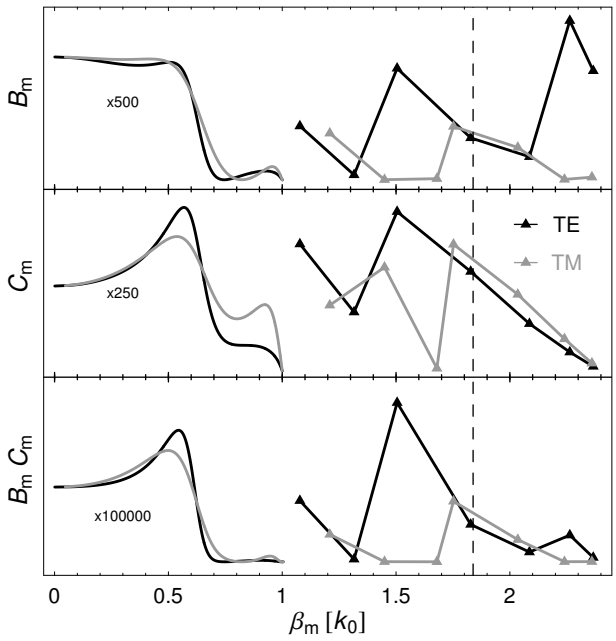

Fig. 7.5: Mode distribution of the optimised PhC LED. Overlap with the active region B_m, with the PhC layer C_m and the corresponding product $B_m C_m$ at peak wavelength $\lambda_{peak}=520nm$ for TE-polarized guided (black triangles), TE-polarized radiative (black lines), TM-polarized guided (grey triangles), and TM-polarized radiative (grey lines) modes. The vertical dashed line indicates the average refractive index of the PhC layer.

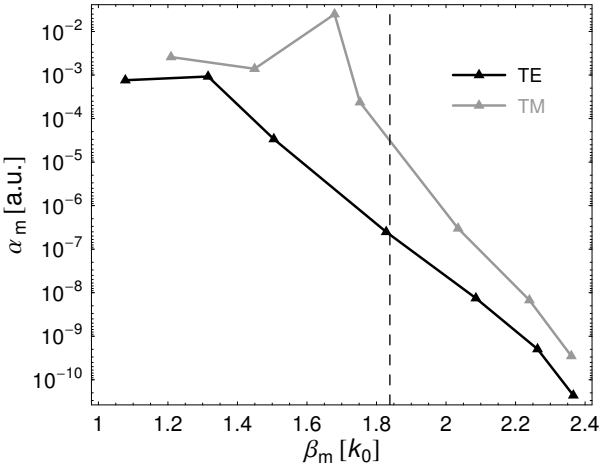

Fig. 7.6: Absorption coefficient for the guided modes of the optimised PhC LED. The vertical dashed line indicates the average refractive index of the PhC layer. Even though the overlap product as shown in Fig. 7.5 favours a main reciprocal lattice vector length of $G_0=1.5k_0$, the absorption calls for a reduced G_0.

The FDTD simulations in Fig. 7.7 reveal an improvement in extraction efficiency compared to the thick PhC LED (the roughened LED) of the previous chapter of 53% (16%) for the PhC with $G_0=k_0$. In contrast, the PhC with $G_0=1.6k_0$ has less overall extraction efficiency, even though it extracts the guided mode with very large overlap product very efficiently. The latter causes the higher extraction efficiency of this lattice for small integration radii. The extraction efficiency of the PhC with $G_0=2.3k_0$ can be well explained by the lack of omni-directionality.

Of course, a roughened LED also benefits from a reduced absorption of the guided modes due to the mirror combination SiO_2+Ag. Therefore, we replaced the Ag-based mirror in the roughened LED by this combined mirror but left the overall thickness of 3µm and the maximum etch depth of 1µm. As can be seen in Fig. 7.7 the reduced absorption losses of the

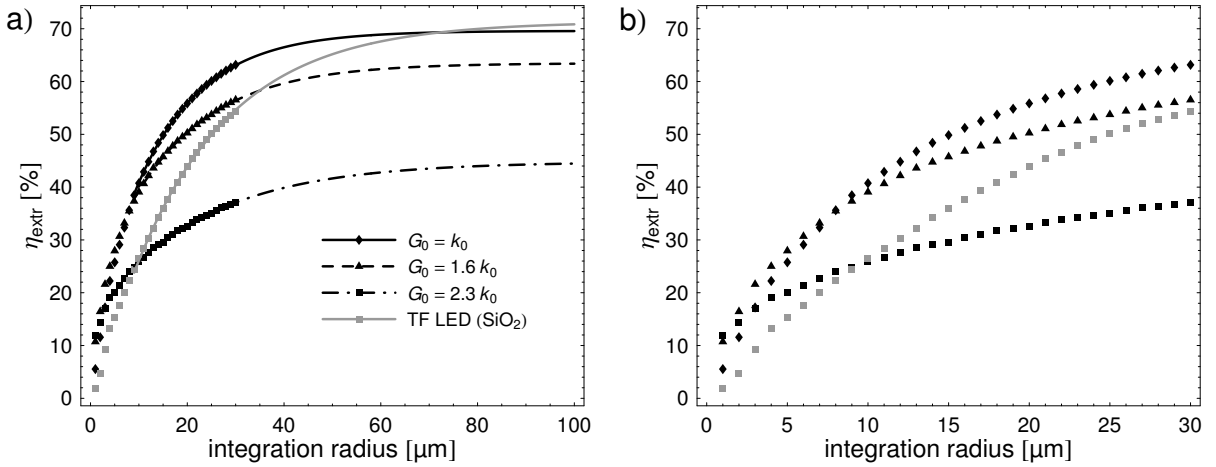

Fig. 7.7: Extraction efficiency from FDTD simulations of the optimum PhC LED from Fig. 7.4 with $G_0 = k_0$ (solid black line, black diamonds), $G_0 = 1.6\,k_0$ (dashed black line, black triangles), and $G_0 = 2.3\,k_0$ (dash-dotted black line, black boxes). The solid grey line (grey boxes) depicts the results from a roughened LED with a combined SiO_2-Ag mirror but 3µm overall thickness.

guided modes enhance the extraction efficiency and the roughened LED with SiO_2 catches up to the best PhC LED. Due to the lower interaction of the modes with the surface structuring – remember its thickness – and the spread Fourier spectrum the rough surface accomplishes its extraction efficiency after larger propagation distances.

7.2 Étendue Limited Applications

In this section, we focus on the implementation of PhC LEDs in an étendue limited application in comparison to a standard thin-film LED. For these systems the directionality in addition to the overall extraction efficiency is decisive for their performance as derived in section 2.4.

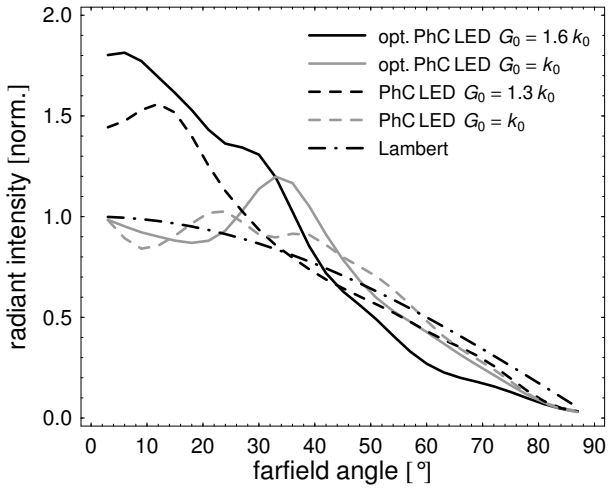

Fig. 7.8: Radiant intensities from FDTD simulations of the opt. PhC LED with $G_0 = k_0$ (grey solid line), $G_0 = 1.6\,k_0$ (black solid line), the thick PhC LED with $G_0 = k_0$ (grey dashed line), $G_0 = 1.3\,k_0$ (black dashed line), and a Lambertian emission profile (black dash-dotted line) representing the roughened LEDs. The emission patterns are normalized to 1W radiant flux.

LED	η_{extr} [%]	D(30°) [%]	D(60°) [%]	Efficacy (lm/W)
Opt. PhC LED $G_0=k_0$	70	25	83	119
Opt. PhC LED $G_0=1.6k_0$	63	40	88	107
PhC LED $G_0=k_0$	46	26	81	78
PhC LED $G_0=1.3k_0$	42	34	81	71
Rough TF LED	59	25	75	100
Rough TF LED, SiO_2	71	25	75	120

Table 7.1: Summary of properties of the LEDs discussed in this chapter. The extraction efficiencies are obtained from extrapolated FDTD results. These FDTD simulations also yield the emission pattern and thus the directionality for the PhC LEDs. The emission profile of the rough LEDs is assumed Lambertian. The efficacy of the rough thin-film (TF) LED with standard mirror is set to 100lm/W. The efficacies of the other LEDs are calculated according to their extraction efficiencies.

In Fig. 7.8 the far fields of the investigated LEDs are summarized and the relevant properties in Table 7.1. The optimised PhC LED with the highest extraction efficiency exhibits a rather flat emission pattern owing to high order diffraction. By adjusting the main reciprocal lattice vector to $G_0=1.6k_0$ the guided mode with highest overlap product is diffracted very efficiently towards the surface normal. Hence, a highly directional emission is gained at the expense of a small drop in efficiency. However, due to the diffraction along the guided modes' circles the directionality of the initially emitted light is decreased from 51% down to 40% within 30°. The analogous optimisation of the main reciprocal lattice vector from $G_0=k_0$ to $G_0=1.3k_0$ for the thick PhC LED also reveals a stronger forward emission. For the roughened thin-film LEDs a Lambertian emission pattern is used according to the uniform Fourier spectrum and [59].

In order to compare these LEDs with respect to an étendue limited application we assume the following. The rough thin-film LED with standard mirror serves as the reference and its radiant flux is set to 100lm at 1W of electrical input power. We further neglect the potential impact of an altered vertical layer stack, as in the case of the optimised PhC LED, on the internal quantum efficiency or the electrical efficiency. Therefore, the difference between the different samples in terms of wall-plug efficiency or efficacy stems from the extraction efficiency alone. The values for the efficacy used throughout this chapter are given in Table 7.1. The resulting emitted radiant flux within some limited acceptance θ_L is calculated according to the directionality within that angle multiplied with the overall emitted flux and is shown in Fig. 7.9. Despite its lower overall efficacy the optimised PhC LED with $G_0=1.6k_0$ outperforms every competitor within an acceptance angle $\theta_L<54°$ due to its high directionality.

For the performance analysis of an étendue limited application we utilize the DMD based projection system already introduced in 2.4. If the whole emission of the LEDs can be collected the largest feasible source area is $4\,mm^2$ corresponding to the étendue of the imager of $E_{sys}=12.7\,mm^2 sr$. If we assume a chip size of $1\,mm^2$ of each LED with efficacies as summarized in Table 7.1, the roughened standard LED yields 400lm at the imager. Owing to the constant radiance of its Lambertian emission characteristics this amount of luminous flux stays constant for decreased acceptance angles if the source area A_L is adjusted to match the étendue of the imager. Consequently, more chips have to be incorporated. According to the higher efficacy the system with the roughened LED with SiO_2 projects constantly 480lm onto the DMD. In contrast, by incorporating PhC LEDs with high directionality and comparable efficacy up to 800lm can be generated on the imager by increasing the source area. However, this results in system efficacies of as low as $800lm/128W \approx 6lm/W$. In general, the efficacy gets lower the smaller the acceptance angle becomes, since the light outside this angle is wasted regardless of the emission pattern of the LED. But even with moderate source areas of

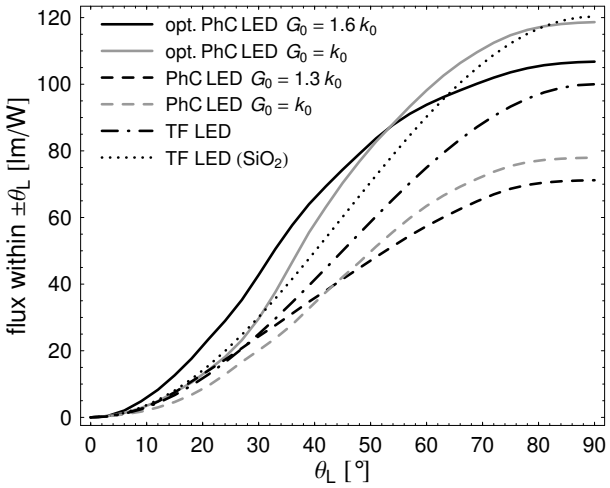

Fig. 7.9: Radiant flux as a function of the acceptance angle θ_L for the opt. PhC LED with $G_0 = k_0$ (grey solid line), $G_0 = 1.6k_0$ (black solid line), the thick PhC LED with $G_0 = k_0$ (grey dashed line), $G_0 = 1.3k_0$ (black dashed line), the roughened LED (black dash-dotted line), and the roughened LED with SiO_2 (black dotted line).

approximately 10mm^2 (θ_L=40°) the thin directional PhC LED reveals 1.3 times more flux on the DMD compared to the system with the most efficient rough LED at the same electrical input power. This enhancement does not rely on the actual source area as only the total flux onto the imager does. Therefore, any system with a limited acceptance angle of θ_L<65° benefits from the incorporation of this thin PhC LED. Only for acceptance angles of 54°<θ_L<80° the PhC LED with highest overall efficacy is applicable. In contrast, the standard PhC LED hardly achieves any reasonable enhancement compared to the standard thin-film LED due to its lower overall efficacy and a moderate forward emission.

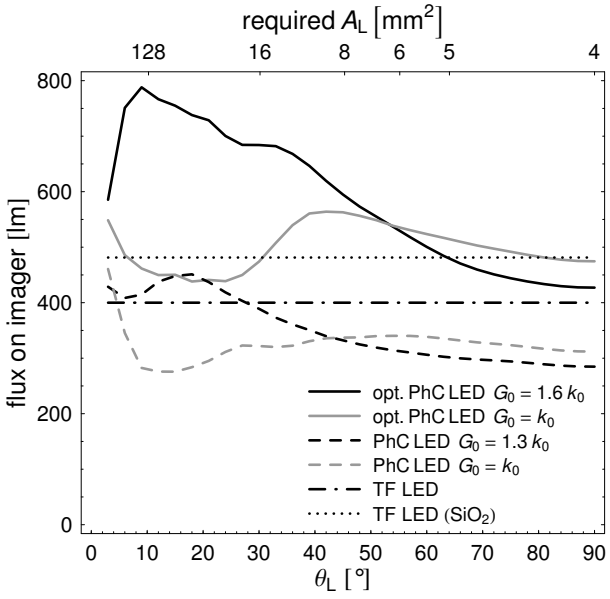

Fig. 7.10: Flux onto a DMD with $E_{sys} = 12.7mm^2sr$ as a function of the acceptance angle θ_L for the opt. PhC LED with $G_0 = k_0$ (grey solid line), $G_0 = 1.6k_0$ (black solid line), the thick PhC LED with $G_0 = k_0$ (grey dashed line), $G_0 = 1.3k_0$ (black dashed line), the roughened LED (black dash-dotted line), and the roughened LED with SiO_2 (black dotted line). The upper x-axis shows the required source area A_L in order to match the étendue of the imager and to generate the flux on the imager as given on the left y-axis.

8 Conclusions

The goal of this work was to clarify the benefit of nano-structuring for light-emitting diodes, namely photonic crystals for light extraction and surface plasmon polaritons for internal light generation. Even though considerable work already showed that the efficiency of as-grown LEDs can be enhanced by these mechanisms, the benchmark for the applicability are nowadays commercially available thin-film devices with surface roughening. These devices achieve extraction efficiencies as high as 85% with encapsulation and hence, there is only little room for improvement. However, certain applications or the internal quantum efficiency could profit from PhCs or SPPs. PhC LEDs in particular could improve the performance of étendue limited systems like projectors or automotive headlamps owing to their beam shaping properties.

It turned out that the application of SPP LEDs is only attractive for LEDs with poor internal quantum efficiency. In this case, the enhanced Purcell factor due to coupling of the active region with the SP suppresses non-radiative recombination. However, the higher the internal quantum efficiency of an emitter gets, the lower is the impact of an increased spontaneous emission rate. On the other hand, the extraction of light from the SP is the main bottleneck for a significant enhancement because the competing process, i.e. absorption inside the metal, is strong. If the extraction of light from the semiconductor to air is additionally taken into account, the necessary structuring of the mirror results in a reduced reflectivity and consequently a decreased extraction efficiency to air owing to a mutual coupling of guided modes with the SP. Usually, the mirror reflectivity is less important in both limits, high absorption rates within or high extraction rates from the LED structure. In general, the absorption of the SP has to be reduced in order to extract the light from the SP and afterwards from the LED more efficiently. Nevertheless, a high level of the Purcell factor is still necessary. A further improvement of the Purcell factor as in the case of localized particle plasmons [106] hardly overcomes the penalty of metal absorption [107].

The major part of the work is dedicated to PhC LEDs. With respect to the overall efficiency of the LED shallow etched PhCs are preferable as they imply less penalties on the functionality of the perforated layers. In this regime, the dispersion relation of guided modes is almost not affected by the PhC as the difference in the average refractive index seen by two modes at the degeneracy points can be neglected. Therefore, the PhC acts as a diffraction grating and the dispersion is given by Bragg's law of diffraction. Under these assumptions the PhC can be treated as a perturbation of the vertical layer stack that enables the coupling of guided modes with radiative modes above the light line. A model based upon coupled mode theory is proposed that allows to identify the important quantities on the way to high efficiency PhC LEDs. A scan over a wide variety of parameters can be carried out since the demand on computational resources for this diffraction model is low. Furthermore, a physically correct scheme within the FDTD method is established for the calculation of the absolute extraction efficiency and the far field radiation pattern of surface structured LEDs. Hence, it has been possible to verify the diffraction model. But even more striking, this enables a quantitative comparison between PhC LEDs and standard thin-film LEDs with surface roughening in terms of overall efficiency and with respect to applications that account for the radiation pattern.

Based upon these modelling tools the impact of the different parameters on the diffraction process and the extraction efficiency has been investigated. Apart from the PhC parameters, like pitch, filling fraction, or lattice type, also the vertical layer stack plays an important role for the optimisation of PhC LEDs. The LED should support guided modes that couple strongly to radiative modes and gather a large fraction of the spontaneous emission. For a given vertical layer stack the pitch of the PhC should be chosen in order to extract these guided modes into air by first order diffraction. It has been shown, however, that replacing the random surface structure of commercial devices by a PhC does not result in more efficient LEDs. Owing to its discrete diffraction behaviour and the large number of guided modes the PhC is inferior to the rough surface in the case of modest bulk absorption. Only if the structure contains no absorbing layers both surface structures should perform equally as both redistribute guided light. Increasing the omni-directionality of the lattice, i.e. "approximating" the rough surface, improves the extraction efficiency but limits the impact of the PhC on the far field. Therefore, the route for high efficiency PhC LEDs is to reduce both the number of guided modes and the absorption within the structure. Of course, the latter is also beneficial for common LEDs. Furthermore, the diffraction rate of the guided modes should be improved. In general, weakly guided modes interact sufficiently with the PhC as they are confined by the semiconductor-to-air interface and the mirror. In order to extract the strongly guided modes that are evanescent within the PhC the corresponding confining core should be as thin as technologically feasible. However, the absorption within the structure has to be taken into account and might even out the benefit from a decreased core thickness. A structure optimised in this respect showed an extraction efficiency competing well with that of commercial LEDs. The potential implications of an altered layer stack on the internal, injection and electrical efficiency have to be addressed separately.

The performance of étendue limited applications can indeed be enhanced by the incorporation of PhC LEDs as a light source owing to their collimated emission pattern. This advantage only has any effect if a fraction of the LED's total emission cannot be coupled into the optical system and this fraction is reduced by the beam steering properties of the PhC. However, a diffracting PhC cannot achieve complete collimation of the far field within a desired solid angle as diffraction outside simultaneously takes place. Hence, the efficiency of PhC LEDs has to be comparable to rough thin-film LEDs in order to obtain an absolute enhancement within the limited extraction cone. With the help of an optimised PhC LED it was possible to almost double the flux on the imager for narrow acceptance angles. Of course, in terms of system efficiency it is not advantageous to waste any light owing to a limited acceptance angle but to collect every quantum of light [35].

In conclusion, the extraction efficiency of a LED boils down to the two numbers: extraction and absorption coefficient. The lower the latter, the more efficient is the LED. Hence, progress in chip technology in terms of absorption reduction does not only increase the extraction efficiency of common LEDs. Additionally, PhCs along with their ability to control the light emission become more and more applicable. However, complete control of the light emission can only be achieved in the case of strongly coupled PhC where advantage of band-bending can be taken [52]. Here, achievements in material science, like core-shell growth of nano-rods, could overcome the main drawback of a reduced active area.

9 Appendix

Fig. 9.1 shows a schematic sketch of a thin-film LED with its rough surface and bottom mirror. For the derivation of (2.9) in section 2.3.2 light propagation is assumed completely incoherent. Hence, only the intensities are taken into account and bounce between the surface and the mirror.

For an isotropic source distribution $I_s(\theta)=1$ the amount of light I_1 incident on the surface for the first time reads

$$I_1 = \frac{A_{iso}}{2} + \frac{A_{iso}}{2} R_M \tag{9.1}$$

with R_M the reflectivity of the mirror and A_{iso} the amount of light not absorbed after propagation through the semiconductor with absorption coefficient α and thickness t

$$A_{iso} = \int_0^{90°} I_s(\theta) \exp\left(-\alpha \frac{t}{\cos\theta}\right) \sin\theta \, d\theta \,. \tag{9.2}$$

The surface is assumed to scatter the light perfect Lambertian and thus, the amount of light transmitted into the ambient medium is given by

$$T_1 = \frac{A_{iso}}{2}(1 + R_M) T_{Lam} \tag{9.3}$$

with

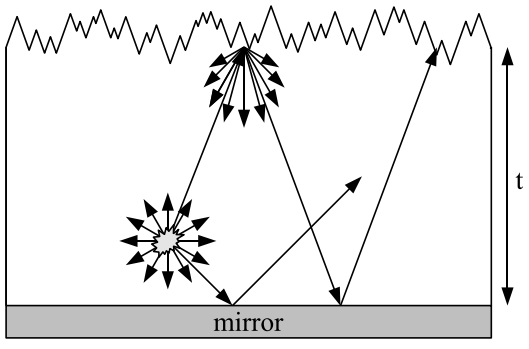

Fig. 9.1: Isotropic light generation and Lambertian redistribution at the rough surface within a thin-film LED. The distance between the surface and the mirror is t.

$$T_{\mathrm{Lam}} = 2\int_0^{\theta_c} \cos\theta \sin\theta \, d\theta \, . \tag{9.4}$$

Hence, the intensity $R_{\mathrm{Lam}}=1-T_{\mathrm{Lam}}$ is reflected back into the LED chip. After propagation through the chip, reflectance at mirror and again propagation, this light gives rise to the second transmission

$$T_2 = \frac{A_{\mathrm{iso}}}{2}(1+R_{\mathrm{M}})R_{\mathrm{Lam}}A_{\mathrm{Lam}}R_{\mathrm{M}}A_{\mathrm{Lam}}T_{\mathrm{Lam}} \, . \tag{9.5}$$

Thus the extraction efficiency after N incidences on the surface is determined by

$$\eta_{\mathrm{extr}}(N) = \frac{A_{\mathrm{iso}}}{2}(1+R_{\mathrm{M}})T_{\mathrm{Lam}}\sum_{n=0}^{N}\frac{1}{1-A_{\mathrm{Lam}}^{2\mathrm{n}}R_{\mathrm{M}}^{\mathrm{n}}R_{\mathrm{Lam}}^{\mathrm{n}}} \tag{9.6}$$

and the overall extraction efficiency for $N\rightarrow\infty$

$$\eta_{\mathrm{extr}} = \frac{A_{\mathrm{iso}}}{2}(1+R_{\mathrm{M}})\frac{T_{\mathrm{Lam}}}{1-A_{\mathrm{Lam}}^{2}R_{\mathrm{M}}R_{\mathrm{Lam}}} \, . \tag{9.7}$$

10 Bibliography

[1] H. J. Round, Electrical World 49, 309 (1907).

[2] N. Zheludev, *The life and times of the LED – a 100-year history*, Nature Photonics 1, 189 (2007).

[3] N. Holonyak, Jr. and S. F. Bevacqua, *Coherent (visible) light emission from $Ga(As_{1-x}P_x)$ junctions*, Appl. Phys. Lett. 1, 82 (1962).

[4] McKinsey & Company, *Pathways to a Low-Carbon Economy – Version 2 of the Global Greenhouse Gas Abatement Cost Curve*, (2009).

[5] S. Nakamura, S. Pearton, and G. Fasol, *The blue laser diode: the complete story*, Springer, Berlin (2000).

[6] J. M. Phillips, M. E. Coltring, M. H. Crawford, A. J. Fischer, M. R. Krames, R. Mueller-Mach, G. O. Mueller, Y. Ohno, L. E. S. Rohwer, J. A. Simmons, and J.Y. Tsao, *Research challenges to ultra-efficient inorganic solid-state lighting*, Laser Photonics Rev. 1, 307 (2007).

[7] http://www.osram-os.com/osram_os/EN/Products/Light_Emitting_Diodes_(LED)/index.html

[8] W. N. Carr and G. E. Pittman, *One-watt GaAs p-n junction infrared source*, Appl. Phys. Lett. 3, 173 (1963).

[9] W. N. Carr, *Photometric figures of merit for semiconductor luminescent sources operating in spontaneous mode*, Infrared Phys. 6, 19 (1966). (Reprinted in: Semiconductor Devices Pioneering Papers, edited by S. M. Sze, World Scientific, Singapore (1991), pp. 919–937).

[10] M. R. Krames, M. Ochiai-Holcomb, G. E. Höfler, C. Carter-Coman, E. I. Chen, I.-H. Tan, P. Grillot, N. F. Gardner, H. C. Chui, J.-W. Huang, S. A. Stockman, F. A. Kish, M. G. Craford, T. S. Tan, C. P. Kocot, M. Hueschen, J. Posselt, B. Loh, G. Sasser, and D. Collins, *High-power truncated-inverted-pyramid $(Al_xGa_{1-x})_{0.5}In_{0.5}P/GaP$ light-emitting diode exhibiting >50% external quantum efficiency*, Appl. Phys. Lett. 75, 2365 (1999).

[11] I. Schnitzer, E. Yablonovitch, C. Caneau, T. J. Gmitter, and A. Scherer, *30% external quantum efficiency from surface textured, thin-film light-emitting diodes*, Appl. Phys. Lett. 63, 2174 (1993).

[12] S. Fan, P. R. Villeneuve, J. D. Joannopoulos, and E. F. Schubert, *High extraction efficiency of spontaneous emission from slabs of photonic crystals*, Phys. Rev. Lett. 78, 3294 (1997).

[13] R. K. Lee, Y. Xu, and A. Yariv, *Modified spontaneous emission from a two-dimensional photonic bandgap crystal slab*, J. Opt. Soc. Am. B 17, 1438 (2000).

[14] M. Fujita, S. Takahashi, Y. Tanaka, T. Asano, and S. Noda, *Simultaneous inhibition and redistribution of spontaneous light emission in photonic crystals*, Science 308, 1296 (2005).

[15] K. Bergenek, Ch.Wiesmann, H. Zull, R.Wirth, P. Sundgren, N. Linder, K. Streubel, and T. F. Krauss, *Directional light extraction from thin-film resonant cavity light-emitting diodes with a photonic crystal*, Appl. Phys. Lett. 93, 231109 (2008).

[16] J. Shakya, K. H. Kim, J. Y. Lin, and H. X. Jiang, *Enhanced light extraction in III-nitride ultraviolet photonic crystal light-emitting diodes*, Appl. Phys. Lett. 85, 142 (2004).

[17] J. J. Wierer, M. R. Krames, J. E. Epler, N. F. Gardner, M. G. Craford, J. R. Wendt, J. A. Simmons, and M. M. Sigalas, *InGaN/GaN quantum-well heterostructure light-emitting diodes employing photonic crystal structures*, Appl. Phys. Lett. 84, 3885 (2004).

[18] K. McGroddy, A. David, E. Matioli, M. Iza, S. Nakamura, S. DenBaars, J. S. Speck, C. Weisbuch, and E. L. Hu, *Directional emission control and increased light extraction in GaN photonic crystal light-emitting diodes*, Appl. Phys. Lett. 93, 103502 (2008).

[19] D. Delbeke, P. Bienstmann, R. Bockstaele, and R. Baets, *Rigorous electromagnetic analysis of dipole emission in periodically corrugated layers: the grating-assisted resonant-cavity light-emitting diode*, J. Opt. Soc. Am. A 5, 871 (2002).

[20] M. Rattier, H. Benisty, E. Schwoob, C. Weisbuch, T. F. Krauss, C. J. M. Smith, R. Houdré, and U. Oesterle, *Omnidirectional and compact guided light extraction from Archimedean photonic lattices*, Appl. Phys. Lett. 83, 1283 (2003).

[21] A. David, C. Meier, R. Sharma, F. S. Diana, S. P. DenBaars, E. Hu, S. Nakamura, C. Weisbuch, and H. Benisty, *Photonic bands in two-dimensionally patterned multimode GaN waveguides for light extraction*, Appl. Phys. Lett. 87, 101107 (2005).

[22] A. David, T. Fujii, R. Sharma, K. McGroddy, S. Nakamura, S. P. DenBaars, E. L. Hu, C. Weisbuch, and H. Benisty, *Photonic-crystal GaN light-emitting diodes with tailored guided modes distribution*, Appl. Phys. Lett. 88, 061124 (2006).

[23] A. David, T. Fujii, E. Matioli, R. Sharma, S. Nakamura, S. P. DenBaars, and C. Weisbuch, *GaN light-emitting diodes with Archimedean lattice photonic crystals*, Appl. Phys. Lett. 88, 073510 (2006).

[24] A. David, *High-efficiency GaN-based light-emitting diodes: Light extraction by photonic crystals and microcavities*, PhD thesis (2006), appendix B.

[25] A. David, H. Benisty, and C. Weisbuch, *Optimization of lightdiffracting photonic-crystals for high extraction efficiency LEDs*, J. Display Technol. 3, 133, (2007).

[26] A. David, B. Moran, K. McGroddy, E. Matioli, E. L. Hu, S. P. DenBaars, S. Nakamura, and C. Weisbuch, *GaN/InGaN light-emitting diodes with embedded photonic crystal obtained by lateral epitaxial overgrowth*, Appl. Phys. Lett. 92, 113514 (2008).

[27] M.-K. Kwon, J.-Y. Kim, I.-K. Park, K. S. Kim, G.-Y. Jang, S.-J. Park, J.W. Kim, and Y. C. Kim, *Enhanced emission efficiency of GaN/InGaN multiple quantum well*

light-emitting diodes with an embedded photonic crystal, Appl. Phys. Lett. 92, 251110 (2008).

[28] Ch. Wiesmann, K. Bergenek, N. Linder, and U. T. Schwarz, *Analysis of the emission characteristics of photonic crystal LEDs*, Proc. SPIE 6989, Light Emission I, 69890L (2008).

[29] H. Benisty, J. Danglot, A. Talneau, S. Enoch, J. M. Pottage, and A. David, *Investigation of extracting photonic crystal lattices for guided modes of GaAs-based heterostructures*, IEEE J. Quantum Electron. 44, 777 (2008).

[30] C.-F. Lai, J.-Y. Chi, H.-H. Yen, H. C. Kuo, C.-H. Chao, H.-T. Hsueh, and J.-F. Trevor, Wang, C.-Y. Huang, and W.-Y. Yeh, *Polarized light emission from photonic crystal light-emitting diodes*, Appl. Phys. Lett. 92, 243118 (2008).

[31] K. Bergenek, Ch. Wiesmann, R. Wirth, L. O'Faolain, N. Linder, K. Streubel, and T. F. Krauss, *Enhanced light extraction efficiency from AlGaInP thin-film light-emitting diodes with photonic crystals*, Appl. Phys. Lett. 93, 041105 (2008).

[32] K. Bergenek, Ch. Wiesmann, H. Zull, C. Rumbolz, R. Wirth, N. Linder, K. Streubel, T. F. Krauss, *Beam-shaping properties of InGaN thin-film micro-cavity light-emitting diodes with photonic crystals*, to be published in Proc. SPIE 7231, LED Desing and Fabrication I, 7231-11.

[33] K. Bergenek, Ch. Wiesmann, H. Zull, R. Wirth, C. Rumbolz, N. Linder, K. Streubel, and T. F. Krauss, to be published.

[34] G. Harbers, S. J. Bierhuizen, and M. R. Krames, *Performance of high power light-emitting diodes in display illumination applications*, J. Display Technol. 3, 98 (2008).

[35] A. Wilm, *Requirements on LEDs in étendue limited light engines*, Laser and LED Projection, Proc. SPIE 7001, 70010F (2008).

[36] I. Gontijo, M. Boroditsky, E. Yablonovitch, S. Keller, U. K. Mishra, and S. P. DenBaars, *Coupling of InGaN quantum-well photoluminescence to silver surface plasmons*, Phys. Rev. B 60, 11564 (1999).

[37] K. Okamoto, I. Niki, A. Shvartser, Y. Narukawa, T. Mukai, and A. Scherer, *Surface-plasmon-enhanced light emitters based on InGaN quantum wells*, Nature Mater. 3, 601 (2004).

[38] http://www.osram-os.com/osram_os/EN/Press/Press_Releases/Light_Emitting_Diodes/LED-chip-record.jsp

[39] J. A. E. Wasey and W. L. Barnes, *Efficiency of spontaneous emission from planar microcavities*, J. Mod. Opt. 47, 725 (2000).

[40] H. Benisty, R. Stanley, and M. Mayer, *Method of source terms for dipole emission modification in modes of arbitrary planar structures*, J. Opt. Soc. Am. A 15, 1192 (1998).

[41] A. Taflove and S. C. Hagness, *Computational electrodynamics: the finite-difference time-domain method*, Artech House, Norwood (2005).

[42] G. Sun, J. B. Khurgin, and R. A. Soref, *Practicable enhancement of spontaneous emission using surface plasmons*, Appl. Phys. Lett. 90, 111107 (2007).

[43] J. Xu, M. F. Schubert, A. N. Noemaun, D. Zhu, J. K. Kim, E. F. Schubert, M. H. Kim, H. J. Chung, S. Yoon, C. Sone and Y. Park, *Reduction in efficiency droop, forward*

voltage, ideality factor, and wavelength shift in polarization-matched GaInN/GaInN multi-quantum-well light-emitting diodes, Appl. Phys. Lett. 94, 011113 (2009).

[44] R. N. Hall, *Electron-hole recombination in Germanium*, Phys. Rev. 87, 387 (1952).

[45] W. Shockley andW. T. Read, *Statistics of the recombination of holes and electrons*, Phys. Rev. 87, 835 (1952).

[46] A. R. Beatti and P. T. Landsberg, *Auger effect in semiconductors*, Proc. Roy. Soc. London 249, 16 (1959).

[47] Y. C. Shen, G. O. Mueller, S. Watanabe, N. F. Gardner, A. Munkholm, and M. R. Krames, *Auger recombination in InGaN measured by photoluminescence*, Appl. Phys. Lett. 91, 141101 (2007).

[48] M. Sabathil et al. to be published in IWN08 Proceedings.

[49] M. F. Schubert, J. Xu, Q. Dai, F. W. Mont J. K. Kim, and E. F. Schubert, *On resonant optical excitation and carrier escape in GaInN/GaN quantum wells*, Appl. Phys. Lett. 94, 081114 (2009).

[50] E. M. Purcell, *Spontaneous emission probabilities at radio frequencies*, Phys. Rev. 69, 681 (1946).

[51] M. Boroditsky, R. Vrijen, T. F. Krauss, R. Coccioli, R. Bhat, and E. Yablonovitch, *Spontaneous emission extraction and Purcell enhancement from thin-film 2-D photonic crystals*, J. Lightwave Technol. 17, 2096 (1999).

[52] A.-L. Fehrembach, S. Enoch, and A. Sentenac, *Highly directive light sources using two-dimensional photonic crystal slabs*, Appl. Phys. Lett. 79, 4280 (2001).

[53] U. Zehnder, A.Weimar, U. Strauss, M. Fehrer, B. Hahn, H.-J. Lugauer, and V. Härle, *Industrial production of GaN and InGaN-light-emitting diodes on SiC-substrates*, J. Cryst. Growth 230, 497 (2001).

[54] R.Windisch, C. Rooman, S. Meinschmidt, P. Kiesel, D. Zipperer, G. H. Dohler, B. Dutta, M. Kuijk, T. Borghs, and P. Heremans, *Impact of texture-enhanced transmission on high-efficiency surface-textured light-emitting diodes*, Appl. Phys. Lett. 79, 2315 (2001).

[55] M. K. Kelly, O. Ambacher, R. Dimitrov, R. Handschuh, and M. Stutzmann, *Optical process for liftoff of group III-nitride films*, phys. stat. sol. (A) 159, R3 (1997).

[56] W. S. Wong, T. Sands, and N.W. Cheung, *Damage-free separation of GaN thin-films from sapphire substrates*, Appl. Phys. Lett. 72, 599 (1998).

[57] E. Yablonovitch, T. Gmitter, J. P. Harbison, and R. Bhat, *Extreme selectivity in the lift-off of epitaxial GaAs films*, Appl. Phys. Lett. 51, 2222 (1987).

[58] M. R. Krames, O. B. Shchekin, R. Mueller-Mach, G. O. Mueller, L. Zhou, G. Harbers, and M. G. Craford, *Status and future of high-power light-emitting diodes for solid-state lighting*, J. Display Technol. 3, 160 (2007).

[59] V. Haerle, B. Hahn, S. Kaiser, A.Weimar, S. Bader, F. Eberhard, A. Plössl, and D. Eisert, *High brightness LEDs for general lighting applications using the new ThinGaN^{TM}-technology*, phys. stat. sol. (A) 201, 2736 (2004).

[60] R. Windisch, R. Butendeich, S. Illek, S. Kugler, R. Wirth, H. Zull, and K. Streubel, *100-lm/W InGaAlP thin-film light-emitting diodes with buried microreflectors*, IEEE Photon. Technol. Lett. 19, 774 (2007).

[61] S. Illek, I. Pietzonka, A. Ploessl, P. Stauss, W. Wegleiter, R. Windisch, R. Wirth, H. Zull, and K. Streubel, *Scalability of buried micro-reflector light-emitting diodes for high-current applications*, LEDs: Research, Manufacturing and Applications VII Proc. SPIE 4996, 18–25 (2003).

[62] T. Fujii, Y. Gao, R. Sharma, E. L. Hu, S. P. DenBaars, and S. Nakamura, *Increase in the extraction efficiency of GaN-based light-emitting diodes via surface roughening*, Appl. Phys. Lett. 84, 855 (2004).

[63] K. Tadatomo, H. Okagawa, Y. Ohuchi, T. Tsunekawa, Y. Imada, M. Kato, and T. Taguchi, *High output power InGaN ultraviolet light-emitting diodes fabricated on patterned substrates using metalorganic vapor phase epitaxy*, Jpn. J. Appl. Phys. 40, L583 (2001).

[64] E. F. Schubert, N. E. J. Hunt, M. Micovic, R. J. Malik, D. L. Sivco, A.Y. Cho, and G. D. Zydzik, *Highly efficient light-emitting diodes with microcavities*, Science 265, 943 (1994).

[65] H. Benisty, H. De Neve, and C. Weisbuch, *Impact of planar microcavity effects on light extraction – Part I: Basic concepts and analytical trends*, IEEE J. Quantum Electron. 34, 1612 (1998).

[66] H. Benisty, H. De Neve, and C. Weisbuch, *Impact of planar microcavity effects on light extraction – Part II: Selected exact simulations and role of photon recycling*, IEEE J. Quantum Electron. 34, 1632 (1998).

[67] R. Sharma, Y.-S. Choi, C.-F. Wang, A. David, C. Weisbuch, S. Nakamura, and E. L. Hu, *Gallium-nitride-based micro-cavity light-emitting diodes with air-gap distributed Bragg reflectors*, Appl. Phys. Lett. 91, 211108 (2007).

[68] R. Joray, M. Ilegems, R. P. Stanley, W. Schmid, R. Butendeich, R. Wirth, A. Jaeger, and K. Streubel, *Far-field radiation pattern of red emitting thin-film resonant cavity LEDs*, IEEE Photon. Technol. Lett. 18, 1052 (2006).

[69] C. Weisbuch, A. David, T. Fujii, C. Schwach, S. P. Denbaars, S. Nakamura, M. Rattier, H. Benisty, R. Houdré, R. Stanley, J. F. Carlin, T. F. Krauss, and C. J. M. Smith, *Recent results and latest views on microcavity LEDs*, Proc. SPIE 5366, 1–19 (2004).

[70] Y. C. Shen, J. J. Wierer, M. R. Krames, M. J. Ludowise, M. S. Misra, F. Ahmed, A.Y. Kim, G. O.Mueller, J. C. Bhat, S. A. Stockman, and P. S. Martin, *Optical cavity effects in InGAN/GaN quantum-well-heterostructures flip-chip light-emitting diodes*, Appl. Phys. Lett. 82, 2221 (2003).

[71] E. F. Schubert, N. E. J. Hunt, R. J. Malik, M. Micovic, and D. L. Miller, *Temperature and modulation characteristics of resonant-cavity light-emitting diodes*, J. Lightwave Technol. 14, 1721 (1996).

[72] http://www.dlp.com/

[73] J. Muschaweck, Private correspondence, Nov. 2008.

[74] A. Laubsch, M. Sabathil, G. Bruederl, J. Wagner, M. Strassburg, E. Baur, H. Braun, U. T. Schwarz, A. Lell, S. Lutgen, N. Linder, R. Oberschmid, and B. Hahn, *Measurement of the internal quantum efficiency of InGaN quantum wells*, Proc. SPIE, Vol. 6486, 64860J (2007).

[75] M. Sabathil, A. Laubsch, and N. Linder, *Self-consistent modeling of resonant PL in InGaN SQW LED-structure*, Proc. SPIE, Vol. 6486, 64860V (2007)

[76] J. D. Joannopoulos, S. G. Johnson, J. N. Winn, and R. D. Meade, *Photonic crystals – Molding the flow of light*, Princeton University Press, Princeton (2008), pp. 9-17.

[77] M. J. Bergmann and H. C. Casey, *Optical-field calculations for lossy multiple-layer $Al_xGa_{1-x}N/In_xGa_{1-x}N$ laser diodes*, J. Appl. Phys. 84, 1196 (1998).

[78] K. Sakoda, *Optical properties of photonic crystals*, Springer Series in Optical Sciences, Vol. 80, Springer, Berlin (2005), pp. 175–179.

[79] J. D. Joannopoulos, S. G. Johnson, J. N. Winn, and R. D. Meade, *Photonic crystals – Molding the flow of light*, Princeton University Press, Princeton (2008), pp. 127-130.

[80] J. D. Joannopoulos, S. G. Johnson, J. N. Winn, and R. D. Meade, *Photonic crystals – Molding the flow of light*, Princeton University Press, Princeton (2008), p. 18.

[81] M. C. Netti, A. Harris, J. J. Baumberg, D. M. Whittaker, M. B. D. Charlton, M. E. Zoorob, and G. J. Parker, *Optical Trirefringence in Photonic Crystal Waveguides*, Phys. Rev. Lett. 86, 1526 (2001).

[82] D. M. Whittaker and I. S. Culshaw, *Scattering-matrix treatment of patterned multiplayer structures*, Phys. Rev. B 60, 2610 (1999).

[83] S. G. Tikhodeev and A. L. Yablonskii, *Quasiguided modes and optical properties of photonic crystal slabs*, Phys. Rev. B 66, 045102 (2002).

[84] D. Y. K Ko and J. C. Inkson, *Matrix method for tunnelling in heterostructures: Resonant tunnelling in multilayer systems*, Phys. Rev. B 38, 9945 (1988).

[85] D. Marcuse, *Theory of dielectric optical waveguides*, Academic Press, Boston (1991), p. 410.

[86] D. Marcuse, *Theory of dielectric optical waveguides*, Academic Press, Boston (1991), p. 425.

[87] T. Butz, Fouriertransformation für Fußgänger, Wiesbaden, Teubner (2005).

[88] K. Yee, *Numerical solutions of initial boundary value problems involving Maxwell's equations in isotropic media*, IEEE Trans. Antennas and Propag. 14, 302 (1966).

[89] http://www.lumerical.com/fdtd.php

[90] Y. Xu, J. S. Vučković, R. K. Lee, O. J. Painter, A. Scherer, and A. Yariv, *Finite-difference time-domain calculation of spontaneous emission lifetime in a microcavity*, J. Opt. Soc. Am. B 16, 465 (1999).

[91] P. B. Johnson and R.W. Christy, *Optical constants of the noble metals*, Phys. Rev. B 6, 4371 (1972).

[92] http://www.lumerical.com/fdtd_online_help/ref_fdtd_matdb_models.php

[93] D. Delbeke, R. Bockstaele, P. Bienstmann, R. Baets, and H. Benisty, *High-efficiency semiconductor resonant-cavity light-emitting diodes: A review*, J. Selec. Top. Quantum Electron. 8, 189 (2002).

[94] S. Keller, C. Schaake, N. A. Fichtenbaum, C. J. Neufeld, Y. Wu, K. McGroddy, A. David, S. P. DenBaars, C. Weisbuch, J. S. Speck, and U. K. Mishra, *Optical and structural properties of GaN nanopillar and nanostripe arrays with embedded InGaN/GaN multi-quantum wells*, J. Appl. Phys. 100, 054314 (2006).

[95] H. Kitagawa, T. Suto, M. Fujita, Y. Tanaka, T. Asano, and S. Noda, *Green Photoluminescence from GaInN Photonic Crystals*, Appl. Phys. Express 1, 032004 (2008).

[96] W. Streifer, D. Scifres, and R. Burnham, *Analysis of grating-coupled radiation in GaAs:GaAlAs lasers and waveguides*, IEEE J. Quantum. Electron. 12, 422 (1976).

[97] M. B. Stern, H. G. Craighead, P. F. Liao, and P. M. Mankiewich, *Fabrication of 20-nm structures in GaAs*, Appl. Phys. Lett. 45, 410 (1984).

[98] S.Y. Chon, P. R. Krauss, and P. J. Renstrom, *Imprint lithography with 25-nanometer resolution*, Science 272, 85 (1996).

[99] Y. Xia and G. M. Whitesides, *Soft lithography*, Annu. Rev. Mater. Sci. 28 153 (1998).

[100] S. Brueck, *Optical and interferometric lithography – Nanotechnology enablers*, Proc. IEEE 93, 1704 (2005).

[101] H.W. Deckmann and J. H. Dunsmuir, *Natural lithography*, Appl. Phys. Lett. 41, 377 (1982).

[102] W. Han, S. Fan, Q. Li, and Y. Hu, *Synthesis of gallium nitride nanorods through a carbon nanotube-confined Reaction*, Science 277, 1287 (1997).

[103] S. D. Hersee, X. Sun, and X. Wang, *The controlled growth of GaN nanowires*, Nano Lett. 6, 1808 (2006).

[104] F. Qian, S. Gradečak, Y. Li, C.-Y. Wen, and C. M. Lieber, *Core/multishell nanowire heterostructures as multicolor, high-efficiency light-emitting diodes*, Nano Lett. 5, 2287 (2005).

[105] Y. Gao, T. Fujii, R. Sharma, K. Fujito, S. P. Denbaars, S. Nakamura and E. L. Hu, *Roughening hexagonal surface morphology on laser lift-off (LLO) n-face GaN with simple photo-enhanced chemical wet etching*, Jpn. J. Appl. Phys. 43, L 637 (2004).

[106] S. Kühn, U. Håkanson, L. Rogobete, and V. Sandoghdar, *Enhancement of single-molecule fluorescence using a gold nanoparticle as an optical nanoantenna*, Phys. Rev. Lett. 97, 017402 (2006).

[107] J. B. Khurgin, G. Sun, and R. A. Soref, *Electroluminescence efficiency enhancement using metal nanoparticles*, Appl. Phys. Lett. 93, 021120 (2008).

Danksagung

An dieser Stelle möchte ich mich bei allen Personen bedanken, die zum Gelingen dieser Arbeit beigetragen haben. Mein Dank geht an:

- die Firma Osram Opto Semiconductors GmbH für die Möglichkeit, diese Promotion in der Industrie durchführen zu können.
- PD Dr. Ulrich T. Schwarz für die unkomplizierte Betreuung und große Unterstützung dieser Industriepromotion, sowie die vielen Stunden Arbeit, die in das Review-Paper flossen.
- Dr. Norbert Linder für die Anregungen, Hilfen und Antworten auf unzählige Fragen und dafür, dass er trotz vollem Terminkalender immer die Zeit dafür fand.
- Krister Bergenek als photonischen-Kristall-Mitstreiter für die fachlichen wie auch sonstigen Diskussionen, die zum einen neue Wege eröffneten und zum anderen halfen, auf andere Gedanken zu kommen.
- Dr. Ross P. Stanley and Dr. Romuald Houdré for their introduction to photonic crystal LEDs and fruitful discussions, that led to the diffraction model and improved very much the related paper.
- Prof. Dr. Bernd Witzigmann für die Möglichkeit, einige FDTD-Rechnungen auf seinen Servern laufen zu lassen.
- Allen Kolleginnen und Kollegen aus den Abteilungen, denen ich im Laufe der Zeit angehört habe, für die lockere Atmosphäre und Hilfsbereitschaft.
- Herrmann-Josef Robin, der weder Tod noch Teufel fürchtet und deshalb diese Arbeit ohne Vorwissen Korrektur las.
- Nadja Wurm und nochmals Norbert Linder für die wirklich gelungene Abschiedsfeier, die ich eindeutig nicht erwartet hatte, wie man mit Sicherheit sehen konnte...
- Meinen Eltern für ihre Unterstützung und dafür, dass sie unumstößlich hinter mir stehen und an mich glauben.
- Susan Irrgang dafür, dass sie an meiner Seite ist.